Electronic Thermal Conductance of Graphene via Electrical Noise

A dissertation presented
by
Jesse Dylan Crossno
to
The School of Engineering and Applied Sciences

in partial fulfillment of the requirements
for the degree of
Doctor of Philosophy
in the subject of
Applied Physics

Harvard University
Cambridge, Massachusetts
May 2017

Dissertation Advisor: Professor Philip Kim Jesse Dylan Crossno

Electronic Thermal Conductance of Graphene via Electrical Noise

Abstract

This dissertation presents the methods and experimental results of studies on electronic thermal transport in mesoscopic conductors by means of radio frequency Johnson noise thermometry. In particular, we present the application of these methods to study the electronic thermal conductivity of monolayer graphene over a wide range of temperatures, charge densities, and magnetic fields.

A comprehensive theory of thermal noise in conductors is formulated in a language convenient for high frequency measurements of mesoscopic samples. Auto- and cross-correlated Johnson noise thermometry is demonstrated over the temperature range of $3 - 300\ K$ and in magnetic fields up to $13\ T$, achieving a sensitivity of $5.5\ mK$ $(110\ ppm)$ in $1\ s$ of integration time. Techniques for overcoming the challenges of measuring devices with resistances that dynamically vary over multiple orders of magnitude are presented. Impedance matching circuits, capable of withstanding the harsh measurement environments of condensed matter experiments while remaining stable across the extreme changes in temperature and magnetic field, are described. A systematic and robust calibration procedure for converting noise power to electronic temperature is outlined which allows for the inevitable drift of device resistance that often plagues mesoscopic experiments. With the ability to measure electronic temperature, the thermal conductance between the electronic system and a

thermal bath can be measured.

We quantitatively discuss the various cooling mechanisms of the quasi-relativistic electrons in graphene and how they combine to create a complicated thermal network. Moreover, we present experimental techniques to disentangle these mechanisms allowing the study of each cooling pathway independently. Using these methods, the electron-phonon coupling of clean graphene is quantitatively compared to theoretical estimates and found to be an order of magnitude larger than that predicted for graphene intrinsic acoustic-phonons and the disorder-assisted supercollision mechanism. We find that at low temperature and high carrier density, the thermal conductivity of diffusive monolayer graphene closely obeys the Wiedemann-Franz law.

Near the charge neutrality point, we present evidence that the electronic system in monolayer graphene forms an electron-hole plasma with collective behavior described by hydrodynamics. This charge-neutral plasma of quasi-relativistic fermions, known as a Dirac fluid, exhibits a substantial enhancement of the thermal conductivity, due to decoupling of charge and heat currents. We report an order of magnitude increase in the thermal conductivity and the breakdown of the Wiedemann-Franz law in the thermally populated charge-neutral plasma in graphene. A novel hydrodynamic framework in the presence of charge disorder — in the form of a spatially varying chemical potential — is presented and compared quantitatively to our experimental results.

Lastly, measurements for the low temperature thermal conduction of graphene under a magnetic field are presented. We report data spanning from zero field, through the quantum oscillation regime, and into the quantum Hall regime.

Contents

Dedicated to Samantha Lucia Cardillo

Acknowledgments

The past six years at Harvard have been some of the best in my life. The people I've met have become some of my best friends. The colleagues I've worked with, both inside and outside of the lab, have pushed me to grow and continue to inspire me to think bigger than I do. This dissertation has been influenced by so many people that sitting down to write this acknowledgement seems more overwhelming than the dissertation itself. Perhaps I should start with the single most influential person in my life, the person to whom this text is dedicated. Samantha Cardillo has both supported and encouraged me throughout my time at Harvard and before. We were traveling together when we first found out that I was accepted to grad school and she celebrated, even knowing it meant 6+ years of stress, long hours, and late nights apart. We moved from sunny California to Boston together where she helped me through the hardest times. Above all others, this thesis would not have been possible without her.

While my path to graduation was certainly a windy one, I could not have asked for a better advisor and mentor than Philip Kim. Philip has an unbelievable ability to provide support and understanding while still applying enough guidance and direction to keep me moving. I don't think I've ever met someone who cared more deeply for the well-being of their students than Philip. Plus, probably the best meal I've had in years was at one of his now famous BBQs and how many other

people get to say they beat their advisor at candle pin bowling.

It would be an understatement to say that this dissertation would not have happened without the help of KC Fong. KC has affected, in some way, nearly every experiment in this thesis. He helped design, guide, and interpret the Johnson noise thermometry experiments which realized the observation of the Dirac fluid and it is safe to say he has taught me everything I know about microwave experiments. More than this though, I consider KC to be one of my closest friends.

I want to thank all the members of the Kim lab for helping me along the way. Jonah, Ke, Gil-Ho, Xiaomeng, Jing, and Frank, these experiments only worked thanks to you sacrificing your time scratching, transferring, fabricating, and brainstorming. Artem, Kemen and Hugo, the effort you guys spent on building and optimizing the RF circuits and cyrostats was invaluable. Austin and Andy, I likely would have gone crazy over the years without you guys there to distract me. I hope you all take it as a compliment that one major reason I had to write this thesis from home was because, "I have WAY too many friends in lab to write productively"

Over the years, I was lucky enough to collaborate with some amazing people. In particular, I'd like to thank Andy Lucas and Subir Sachdev for taking the time to really explain hydrodynamics in terms that an experimentalist could understand. Thank you to all the folks at the Raytheon BBN, especially Tom, Blake, Colm, and Graham, for going out of their way to patiently teach me how an experiment should be run and Marcus, Mohammed, and Zach for all the great discussions over the years. Thank you to the Yacoby and Capasso labs who were always there to lend tools, cryogenics, and, most importantly, their expertise. And of course, Hannah Belcher, Carolyn Moore, and Bill Walker for doing more than any person should to help me navigate the Harvard bureaucracy.

I can not overstate the great undergraduate education I received from the University of California at Santa Barbara and the Santa Barbara City College. In particular, I owe my deepest gratitude to Mike Young and Jim Allen for showing me what physics was and convincing me to give my education a second chance and to Deborah Fygenson all her guidance over the years. Everyone knows an undergraduate researcher is only as good as their graduate mentor and I was lucky enough to have two great ones. Greg Dyer and Kim Weirich are two of the most patient and helpful people I've known and I'm happy to now call them both friends. As any physics student who has gone through Santa Barbara City College can tell you, at the heart of that program is Don Ion who seemed to teach more with a question than any book could with a paragraph.

I want to thank the amazing friends I've made over the past years who have made my time in Boston great. Bryan Kaye and Daniel Wintz have become two of my best friends and there isn't a doubt in my mind I would not have made it through without them. It's hard to imagine a better group of people than Zach Gault, Will Fitzhugh, Bryan Hassell, Pete Greskoff, and Michael Brady. Evan Walsh, Tony Zhou, Danny Kim, Tommi Hakala, Rui Zhang, and Xi Wang were always there for me. And even though they were mostly on the other side of the country, I want to thank Steve Crawford, Brian Hoffman, Lucy Rangel, Will Snyders, Tommy Foley, Amber Mccreary, Kyle Lutz, Norah Olley, Kevin Dober, Stephanie Hall, Greg Tavangar, Daniel Murawka, and Alex Woolf for reminding me to keep my eye on graduation.

Finally, I cannot say enough about the love and support of family. Without the continual efforts of my parents, Mark and Sally Crossno, and brother, Jordan Crossno, none of this would have been possible.

Previous publications

The experiments on thermal conduction in high density graphene and some of the experimental details for measuring Johnson noise presented in Chapters 2–5 were published in

> "Development of high frequency and wide bandwidth Johnson noise thermometry" J. Crossno, X.Liu, T. Ohki, P. Kim, and K.C. Fong. Applied Physics Letters, 106(2), p.023121 (2015).

The Dirac fluid experimental results shown in chapter 6 were published in

> "Observation of the Dirac fluid and the breakdown of the Wiedemann-Franz law in graphene". J. Crossno, J.K. Shi, K. Wang, X. Liu, A. Harzheim, A. Lucas, S. Sachdev, P. Kim, T. Taniguchi, K. Watanabe, T.A. Ohki, and K.C. Fong. Science, 351(6277), pp.1058-1061 (2016).

The hydrodynamic theory of the Dirac fluid discussed in chapter 7 was published in

> "Transport in inhomogeneous quantum critical fluids and in the Dirac fluid in graphene". A. Lucas, J. Crossno, K.C. Fong, P. Kim, and S. Sachdev. Physical Review B, 93(7), p.075426 (2016).

Sometimes science is a lot more art than science. A lot of people don't get that.

1

Overview

This dissertation describes measurements of thermal transport in two-dimensional systems. While it focuses primarily on extracting the electronic thermal conductivity of graphene, the techniques described here are quite general. Probing the thermal characteristics in these materials requires a new thermometry technique capable of dealing with the challenges unique to

low-dimensional systems. Van der Waals heterostructures, for example, often contain several thin electrical layers separated by atomic distances; precise knowledge of their individual temperatures is critical in characterizing these structures. A good thermometer should have fast measurement times, high accuracy, no magnetic field dependence, and a wide operating temperature range. Nanoscale thermometry imposes additional challenges: the measurement process should be non-perturbative to avoid thermal agitation of minute heat capacities, it should measure electron temperature directly as weak electron-phonon coupling can result in different steady state electronic and lattice temperatures, it should be local and selective to distinguish temperatures of densely packed elements or layers, and it should not require additional complicated processing of the device.

While the above requirements rule out many commonly used thermometry techniques, Johnson noise thermometry (JNT) stands out as a natural solution. Fundamentally based upon the Fluctuation-Dissipation theorem, JNT is a primary thermometry having a straight forward interpretation, independent of the material details. Analogous to radiation thermometry, JNT measures temperature by passively monitoring fluctuations of the conducting components within the device without the need for current excitations.

Chapter 2 outlines the fundamentals of Johnson noise thermometry and with a focus on measurements of noise in mesoscopic systems at high frequency. A general framework for quantifying the noise emitted by a device with a nonuniform spatial temperature profile is developed. We demonstrate techniques for impedance matching devices with resistances which vary dynamically over multiple orders of magnitude. Experiments quantifying the performance of auto- and cross- correlated JNT of a macroscopic resistor are presented.

Chapter 3 describes the various cooling mechanisms of hot electrons in low-dimensional systems. The theoretical treatment of diffusive cooling of electrons in metals, known as the Wiedemann-Franz Law, is presented as well as its limits in the high and low heating regimes. We then quantitatively discuss the coupling of hot electrons to phonons with an emphasis on graphene electron-phonon coupling.

Chapter 4 uses the foundations developed in the previous chapter to outline a technique to extract the electronic thermal conductivity using JNT paired with Joule heating. The intimate connection between dissipation (Joule heating) and fluctuations (Johnson noise) results in a measurement which is insensitive to the device geometry or the form of the conductivity tensor.

Chapter 5 presents data on the thermal conductivity of monolayer graphene doped away from the charge neutrality point. As expected for a degenerate Fermi liquid with a well defined Fermi surface, we find good agreement to the Wiedemann-Franz law at low temperature. At high temperatures we find electronic cooling to be dominated by coupling to phonons and we extract the amplitude and thermal exponent characterizing the power transfer.

Chapter 6 details our experimental findings for graphene in the non-degenerate regime. Similar to the data in chapter 5, at low temperatures we find that graphene obeys the Wiedemann-Franz law while at sufficiently high temperatures electron-phonon coupling dominates. However at intermediate temperatures, we find that inter-particle scattering results in a decoupling of charge and heat currents at the neutrality point and the Wiedemann-Franz law is violated. We compare this strongly-interacting electron-hole plasma of quasi-relativistic fermions (known as a Dirac fluid) to hydrodynamic theories with weak disorder.

Chapter 7 presents a hydrodynamic description of the Dirac fluid with disorder treated as a spatially varying chemical potential. Based on relativistic conservation laws, the hydrodynamic equations are presented for two-dimensional systems to first order. The Dirac fluid in graphene is briefly reviewed and placed in the context of these equations. The experimental data of chapter 6 is then compared to numerical results of this hydrodynamic model.

Chapter 8 contains our most recent results on extending our thermal conduction measurements of graphene into high magnetic fields. The generalized transport coefficients in two-dimensions are defined in tensorial form and a description is given for their classical behavior in the presence of a magnetic field. Thermal conductance of low temperature graphene is measured via Joule heating and Johnson noise from zero field to 13 T. We find quantum oscillations in the thermal signal which diverge as the system enters quantum Hall.

Appendix A contains technical information about the measurement apparatus and Appendix B contains details of the hydrodynamic calculations from chapter 7

In theory, theory and practice are the same thing, but in practice...

Adam Savage

2

Johnson noise thermometry

Given any process in which an applied force generates heat, the reverse process must also exist and, therefore, thermal fluctuations must cause fluctuations in that force. The idea that the same physics governing the dissipation of an object moving through some environment is responsible for the apparent random motion of that object was originally described by Einstein in

the context of pollen grains [1]. The generalized fluctuation-dissipation theorem [2] quantifies this statement for linear systems[†] by relating the power spectral density $S_P(\omega)$ to the real part of the generalized impedance $Z(\omega)$ [3].

$$S_P(\omega) \propto k_B T \, \Re[Z(\omega)] \tag{2.1}$$

Nearly a quarter of a century later, Nyquist [4] related Einstein's description of Brownian motion to the electrical noise measured by Johnson [5, 6]. Although all the key components were in place, it would take until 1946 for the first noise thermometer to be built [7]. The general idea is to measure the noise spectrum emitted by a device and thus determine its electronic temperature. Johnson noise thermometry (JNT) is analogous to radiation thermometry where the blackbody spectrum of an object is used to determine its temperature — in fact, both rely upon modified versions of eq 2.1

2.1 Thermal noise in resistors

Johnson noise, often referred to as Johnson-Nyquist noise, was first measured in 1927 [5]. Johnson found the fluctuations in the squared voltage across a resistor were linearly proportional to both the resistance and the temperature and independent of the conductor being measured. The following year, Nyquist derived the form of the noise spectral density through a simple

[†]Here a linear system is one where the force acting on a particle is proportional to its velocity — i.e. F/v is constant

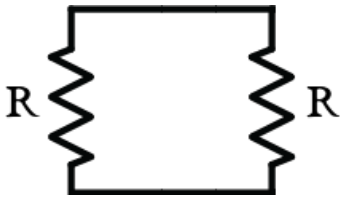

Figure 2.1: Schematic of Nyquist's famous thought experiment. Two resistors in thermal equilibrium are connected end to end and allowed to transfer energy between them via thermal current fluctuations.

thermodynamic argument. Consider two identical resistors in thermal equilibrium at a temperature T connected such that any noise emitted by one is absorbed by the other, as shown in Fig. 2.1. As the resistors are in thermal equilibrium, we know the power being absorbed by a given resistor per unit frequency must be equal to the thermal energy being emitted, $k_B T$. If we represent the Johnson noise of the first resistor as a series voltage source with squared fluctuations, V_{JN}^2, the power dissipated in the second resistor per unit frequency is given by $I^2 R = \left(\frac{V_{JN}}{2R}\right)^2 R$ as the total resistance of the circuit is $2R$. Setting this equal to $k_B T/\Delta f$ leads us to Nyquist's famous result.

$$S_V(\omega) = 4Rk_B T \tag{2.2}$$

This derivation holds regardless of the conductor, be it an electrolytic solution or graphene in a quantum Hall state. However, there is a glaring problem with extending this formula to high frequency; similar to the UV-catastrophe in black-body radiation, Nyquist's formula extends to infinite energies as it lacks a high frequency cutoff. This is fixed by quantum mechanics resulting in a rolloff

of the noise spectrum centered at $\hbar\omega = k_B T$.

$$S_V(\omega) = 4\hbar\omega\, \Re(Z) \left[\frac{1}{2} + \frac{1}{exp(\hbar\omega/k_B T) - 1}\right] \tag{2.3}$$

This high frequency cutoff was seen experimentally by Schoelkopf, et al. [8] and is only of practical import at high frequencies ($> 1\ GHz$) and low temperatures ($< 1\ K$).

2.2 Resistor networks: The Johnson noise temperature

As noise is a random process, finding the spectral density of multiple resistors connected together into a network is not a simple matter of adding the voltages and/or currents via Kirchoff's laws, but instead the mean squared voltages $\langle V^2 \rangle$ and/or mean squared current $\langle I^2 \rangle$ must be combined. This is a property of Gaussian distributed noise: adding together two Gaussian distributions, each with mean 0 and variance σ, with result in another Gaussian distribution with mean 0 and variance 2σ[†].

To find the noise emitted by two resistors in series with resistance R_1 and R_2 and temperature T_1 and T_2, we add their mean squared voltages.

$$\langle V^2 \rangle = 4k_B(R_1 T_1 + R_2 T_2)\Delta f \tag{2.4}$$

[†]This is why mean squared error is often a useful metric. If errors are unbiased and Gaussian distributed then summing their variance is appropriate.

While in the case of the same two resistors in parallel we must add their mean squared currents.

$$\langle I^2 \rangle = 4k_B \left(\frac{T_1}{R_1} + \frac{T_2}{R_2} \right) \Delta f \tag{2.5}$$

This process can be extended to any network of discrete, two-terminal resistors in analogy to Kirchoff's laws.

An effective "Johnson noise temperature" for a given resistor network can be defined as the temperature, T_{JN}, such that the total noise emitted between two given terminals of the network is:

$$\langle V^2 \rangle = 4k_B R \Delta f \times T_{JN} \tag{2.6}$$

where R is the total two-terminal resistance. For an arbitrary network with many terminals, T_{JN} will differ depending upon which two-terminals the noise is measured between. For resistors in series we can see from Eqn. 2.4

$$\langle V^2 \rangle = 4k_B R \left(\frac{R_1}{R} T_1 + \frac{R_2}{R} T_2 \right) \Delta f \tag{2.7}$$

and thus we can define the Johnson noise temperature for this network as:

$$T_{JN}^{series} = \sum_i \frac{R_i}{R} T_i \tag{2.8}$$

Similarly from Eqn.2.5 we see that for resistors in parallel

$$\langle V^2 \rangle = \langle I^2 \rangle \times R^2 = 4k_B R \Delta f (\frac{R}{R_1} T_1 + \frac{R}{R_2} T_2) \tag{2.9}$$

$$T_{JN}^{parallel} = \sum_i \frac{R}{R_i} T_i \tag{2.10}$$

These equations are unified by considering the relationship between the power dissipated in a particular resistor P_i from a voltage across the two terminals of the network (or equally a current across the network) compared to the total power dissipated over the entire network P_0. For the resistors in series $P_i/P_0 = R_i/R$ and for resistors in parallel $P_i/P_0 = R/R_i$. Thus in both cases:

$$T_{JN} = \sum_i \frac{P_i}{P_0} T_i \tag{2.11}$$

In fact, this is quite general and holds for any combination of resistive elements. It stems from the fluctuation dissipation theorem and can be summarized by the statement: The voltage fluctuations created between two terminals of a resistor network due to the thermal fluctuations of a given element in that network are exactly given by the normalized power dissipated in that element due to an external voltage placed on those terminals.

In the continuous limit, Eqn. 2.11 can be used to find the noise emitted by a device with a spatially non-uniform temperature profile $T(\vec{r})$ by solving for the spatial power dissipation profile $\mathcal{P}(\vec{r})$.

$$T_{JN} = \frac{\int \mathcal{P}(\vec{r}) * T(\vec{r}) d\vec{r}}{\int \mathcal{P}(\vec{r}) d\vec{r}} \tag{2.12}$$

where $\vec{r}$ is over the spatial dimensions of the device. Eqn. 2.12 is the main result of this section.

2.3 Johnson noise in RF circuits

When measuring Johnson noise at high frequency, it can be useful to reformulate the problem into the language of microwave circuits. The Nyquist theorem, Eqn. 2.2, can be rewritten to describe the average power, $\langle \mathrm{P} \rangle$, absorbed by an amplifier coupled to a device with reflection coefficient Γ^2:

$$\langle \mathrm{P} \rangle = k_B T \Delta f \ (1 - \Gamma^2) \tag{2.13}$$

and

$$\Gamma = \frac{Z - Z_0}{Z + Z_0} \tag{2.14}$$

where Z is the complex impedance of the device and Z_0 is the characteristic impedance of the measurement circuit — typically 50 Ω. In this form is it quite easy to see the thermodynamic origins of the Nyquist equation. A device at temperature T radiates a power of $k_B T$ per unit frequency; some of that power is absorbed by the measurement circuit, and some is reflected back to the sample. All the resistance dependence of the noise power is captured by Γ[†]. With this new formulation, the importance of minimizing Γ becomes apparent. For high frequency Johnson noise thermometry to be

[†]this is also a nice proof for why Γ in any non absorptive 2 port device must be symmetric, $\Gamma_{12} = \Gamma_{21}$. If this was not true, we could place the device between two resistors in thermal equilibrium and one would heat the other. Two-port devices which report asymmetric coefficients often include internally terminated third ports.

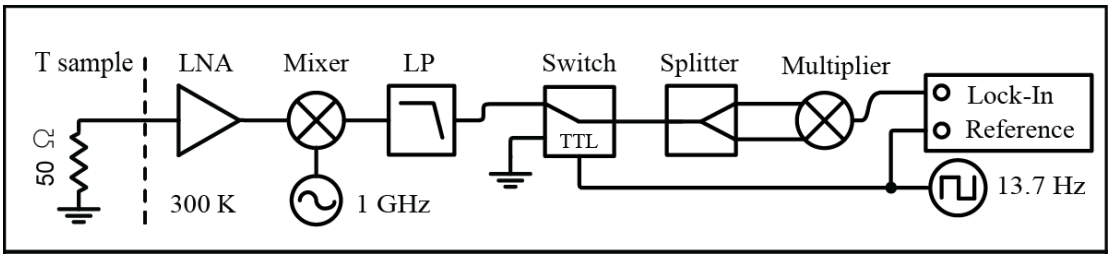

Figure 2.2: High level schematic of a typical Johnson noise thermometry measurement circuit. Noise from an impedance matched sample is amplified and a measurement bandwidth is selected using a homodyne mixer and low-pass filter. The noise power is then measured with a power diode or linear multiplier. A microwave switch acts as a chopper and the signal is measured using a lock-in amplifier.

effective, we must match the impedance of the device to the measurement circuit. For devices with two-terminal resistances far from 50 Ω, it is beneficial to add impedance matching circuits to transform the device to match Z_0 — a good rule of thumb is that resistances less than $\sim$10 Ω or greater than $\sim$250 Ω tend to benefit from matching circuits. As can be seen from Eqn. 2.13, the larger the measurement bandwidth Δf the larger noise signal. In practice, measurement bandwidths are often limited by either the impedance matching circuitry or the amplifier bandwidth; operating at higher frequencies typically increases both these limiting bandwidths.

2.4 An autocorrelation RF noise thermometer

Fig. 2.2 shows an example of a typical, Dicke style [7], radiometer used to measure the temperature of a 50 Ω sample. Radiation from the resistor is coupled into a transmission line terminated with a low noise amplifier (LNA). A typical noise spectrum, collected directly from the output of the LNA, is shown in Fig. 2.3. The signal-to-noise ratio of a noise measurement is mostly

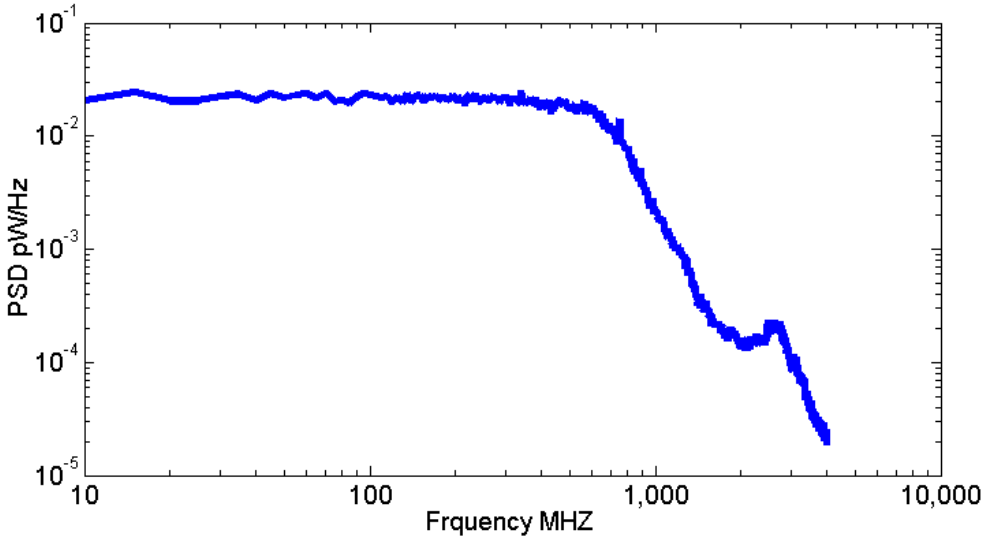

Figure 2.3: A typical spectrum collected directly from the output of a low noise amplifier (Miteq AU-1291, $\sim 65\,dB$ gain, $\sim 100\,K$ noise temperature) with the input terminated with a $50\,\Omega$ resistor. The spectrum is flat until the amplifier gain begins to roll off above $500\,MHz$. The amplitude of the "white" spectrum is proportional to the resistor temperature added to the amplifier noise temperature.

determined by the front-end LNA [9] so care should be taken in selecting the right amplifier. The SiGe LNA (Caltech CITLF3) used throughout the majority of this thesis has a room temperature noise figure, in the frequency range of 0.01 to $2\,GHz$, of about $0.64\,dB$, corresponding to an intrinsic noise temperature of $46\,K$.

Even though Johnson noise has a flat "white" spectrum, it is important to filter out unwanted $1/f$ low frequency fluctuations ($\lesssim 100\,kHz$) as well as high frequency noise produced where the amplifier gain begins to roll off. This can be done using high- and low- pass filters (producing a spectrum similar to that shown in Fig. 2.4, or with a homodyne mixer and low-pass filter combo, as shown in Fig. 2.2.

Once amplified and cleaned, the total noise power can be measured in a few ways: a spectrum

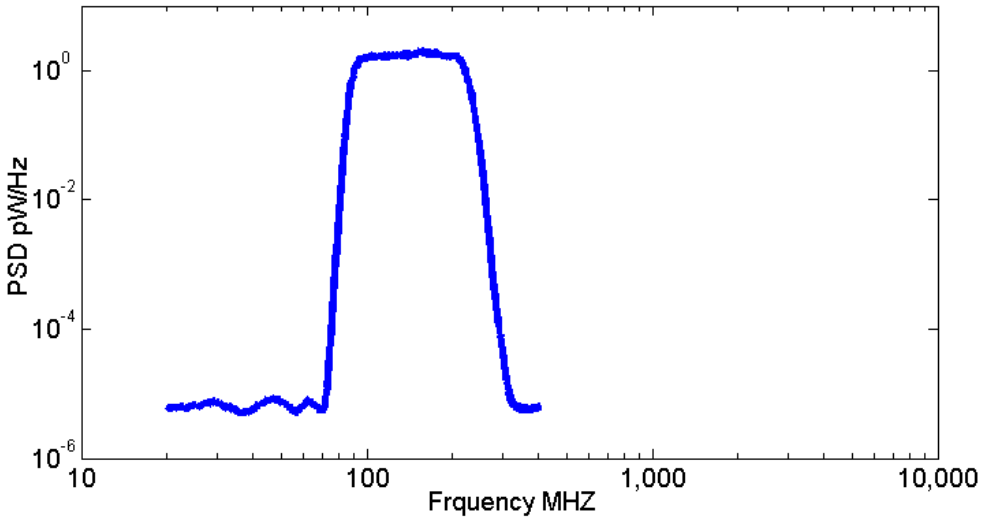

Figure 2.4: A typical Johnson noise spectrum after amplification and filtering using SMA high- and low-pass filters (mini-circuits SLP and SHP series). This square band can then be integrated to find the total noise power and thus the temperature of the resistor.

analyzer or digital Fourier transform can read the spectrum directly, a linear multiplier can square the signal and the mean voltage can be measured, or a high frequency power diode and low pass filter combo can convert the power to a proportional DC voltage. Each technique has its own advantages/disadvantages and in a typical experiment multiple techniques are used.

When presented with a new device or noise setup, a spectrum analyzer is often the first measurement to be done; it provides the most in-depth look into the noise of the system and readily shows problem areas such as narrowband noise, parasitic resonances, and/or amplifier performance. After initial setup, however, spectral detail becomes less important and measurements speeds can be significantly enhanced by moving to an all analog setup.

A linear multiplier (as shown in the schematic Fig. 2.2) can be combined with an RF power split-

ter and a DC voltmeter to directly measure $\langle V^2 \rangle$. Operating from DC to 2 GHz, the multiplier[†] serves as a square law detector with 30 dB dynamic range. A JNT using a multiplier is fast and has the added capability of measuring the autocorrelation function, $\langle V(t)V(t-\tau) \rangle$, by simply adding a delay, τ, to one arm of the splitter. While more complicated to set up, once operational a multiplier is a good combination of speed and versatility.

The simplest of the three power detectors discussed here is an RF power diode/low-pass filter combo (e.g. Pasternach PE8000-50). These detectors input an RF signal and output a DC voltage as shown in Fig. 2.5. The output capacitance of these detectors can be quite large so, if a thermal modulation faster than a few 100 Hz is required, care must be taken in choosing an appropriate model. Nevertheless, this is the detector used most commonly in the experiments detailed in chapters 6 and 8 due to its wide dynamic range (30 dB), small sample package, and ease of use.

Once the noise power is converted to a DC voltage it can be read by a common voltmeter. To increase the sensitivity it is useful to modulate the noise power. When measuring mesoscopic samples this can be done by modulating the electron temperature via Joule heating. However, in the case of a macroscopic resistor, a microwave switch can be placed after amplification to act as a chopper. The resulting signal can then be integrated using a lock-in amplifier.

We can test the noise circuit shown in Fig. 2.2 by attaching a resistor to a coldfinger and varying the temperature from 3 K to 300 K. The results are shown in Fig. 2.6. As the sample temperature is lowered, the noise reduces linearly as expected from Eqn. 2.13. However, if we extrapolate the data to zero temperature, we see residual noise; this offset is due to all the other (temperature indepen-

[†]Analog Devices $ADL5931$

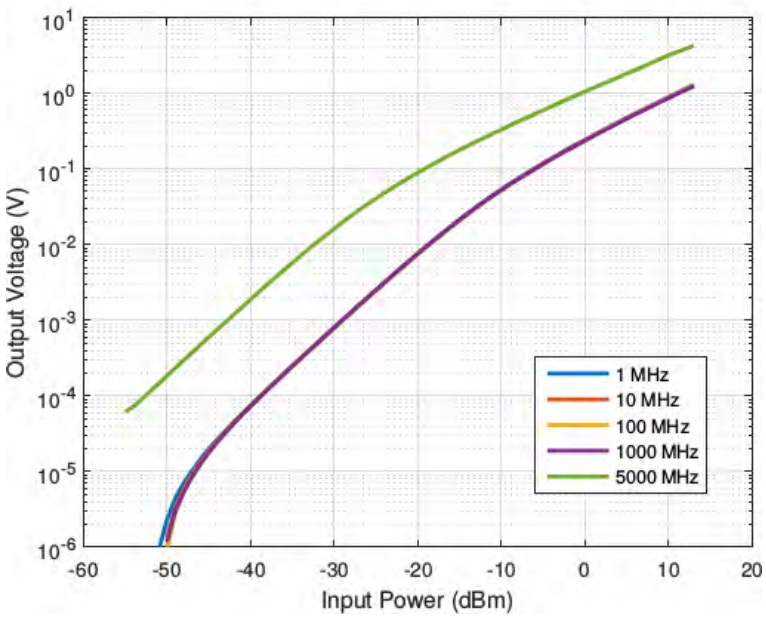

Figure 2.5: Calibration curves for the Pasternach PE8000-50 power detector. A monochromatic signal of known power is supplied using a microwave source (Stanford Research Systems) and the output is measured using a voltmeter (Keithley 2400). The detector has a flat frequency response up to 1 GHz and shows linear behavior from -45 dBm to -15 dBm (30 dB dynamic range)

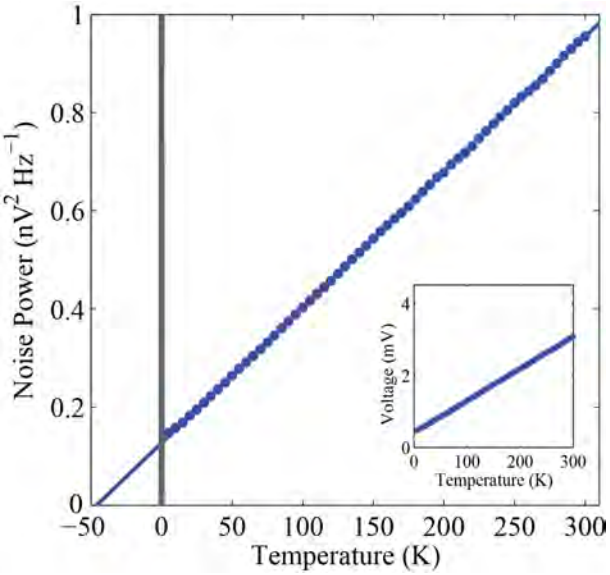

Figure 2.6: Johnson noise of a 50 Ω resistor measured by the circuit shown in Fig. 2.2. Inset show the lock-in amplifier output. The signal is converted to noise power by the Nyquist equation. The solid line is a linear fit with an offset of 68 K due to amplifier noise

dent) noise sources in the system — primarily the front-end amplifier. It is useful to quantify this offset in units of Kelvin and is often called the "system noise temperature". Here we find a system noise temperature of 68 K using a room temperature amplifier. More details on this circuit can be found in Ref. [10]

2.5 Uncertainty in noise measurements

Even noise has noise. There are 2 main areas of uncertainty in a noise measurement. The first comes from the fact that noise is stochastic and deals with how well you know the variance of a Gaussian after measuring some amount of time. If the measurements you take are discrete and

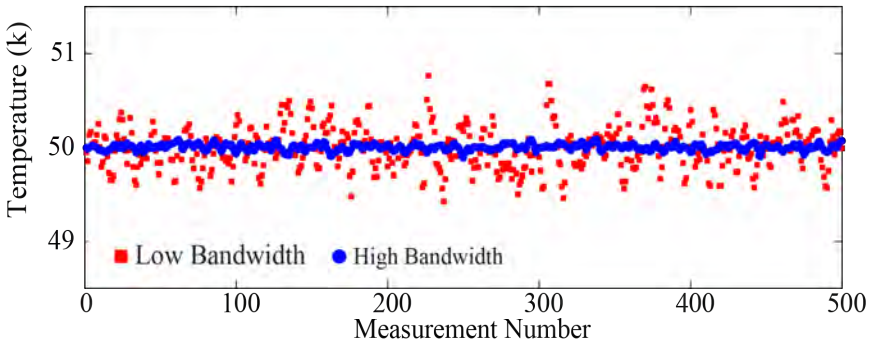

Figure 2.7: 500 repeated Johnson noise measurements of a $50\ \Omega$ resistor at $50\ K$ using two different measurement bandwidths. The high bandwidth data has smaller statistical fluctuations than the low bandwidth data.

uncorrelated then we get the usual $1/\sqrt{n}$ dependence, but what do we do if we are measuring a continuous signal? It turns out that this is an old problem which stems back to the 1940's and measurements of noise on telephone lines [11]. In 1944 Rice showed the effective number of uncorrelated measurements is related to the number of unique zero crossings of the signal and is given by the product of the measurement time τ and the effective noise bandwidth[†] Δf. The surprising fact that the wider the measurement bandwidth the lower the uncertainty, is counter to many experiments where high Q filters are desired to lower the background noise; nevertheless, it can be seen experimentally, as shown in Fig. 2.7

The second source of uncertainty comes from external noise sources, such as amplifiers, and boils down to the question: of the noise you measure, what amount comes from the sample? Quantitatively, this can be thought of as a constant offset to the sample temperature and is called the system noise temperature T_n[‡]. In an autocorrelated noise measurement, T_n can be estimated as the offset of

[†]The effective noise bandwidth is defined as the width of a perfect square band that passes the same noise power as the true filter function.

[‡]It should be noted that the system noise temperature can be quite different from an amplifiers intrinsic

a linear fit to the noise power vs sample temperature, as shown in Fig. 2.6. This offset is highly sensitive to the noise in the front-end amplifier, the sample impedance matching, and the bandwidth being measured, as discussed in section 2.7.

Combining these two sources of error we arrive at the famous Dicke radiometer formula [7]:

$$\delta T = \frac{T + T_n}{\sqrt{\tau \ \Delta f}} \tag{2.15}$$

where δT is the uncertainty in the measured temperature.

We can directly compare Eqn. 2.15 to experiments by repeating a measurement many times and studying how it fluctuates about the mean. Fig. 2.8 compares two histograms, both containing $20,000$ autocorrelation measurements at $50\ K$ with $50\ ms$ integration time but using two different bandwidths: 28 and 328 MHz. A sensitivity of $5.5\ mK\ (110 ppm)$ in 1 second of integration time was achieved using 328 MHz bandwidth on a $50\ K$ signal.

2.6 Impedance matching

Life does not always give you $50\ \Omega$ samples. Eqn. 2.13 illustrates the importance of minimizing the impedance mismatch between the sample and the measurement circuitry – typically $50\ \Omega$. The central principle is to use non-dissipative components to transform the total impedance

noise temperature which often assumes a perfectly matched input impedance. See the section 2.7 for more details

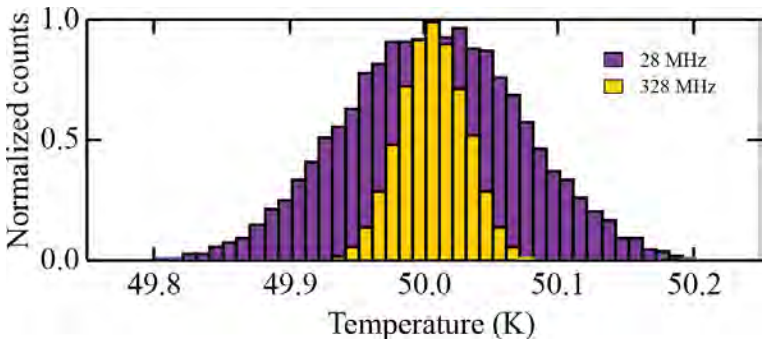

Figure 2.8: Histograms of 20,000 auto-correlation temperature measurements for 28 and $328\ MHz$ bandwidth using $50\ ms$ integration time. Histogram peaks are normalized to 1 for clarity. All data is taken on a $50\ K$ resistive load.

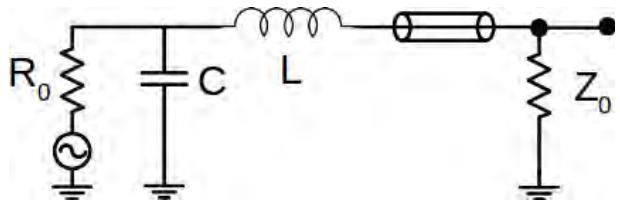

Figure 2.9: Schematic of an LC tank circuit setup in a low-pass configuration used to transform a sample resistance R_0 to match the characteristic impedance of a measurement circuit Z_0.

to $Z(\omega_0) = 50 + 0i\ \Omega$ at some frequency ω_0. Impedance matching mesoscopic devices has a unique set of challenges: electrostatic gates and high magnetic fields can cause device impedances to change by multiple orders of magnitude, cryogenic temperatures require the use of only thermally stable components, and large magnetic fields restrict the use of ferrite inductors.

2.6.1 LC tank circuits

A common way to achieve matching is to use an LC circuit. These transformation circuits, known as a tank circuits, can be arranged in several ways but the configuration most useful to these

experiments is that of a low-pass filter — i.e a shunt capacitor followed by a series inductor as shown in Fig. 2.9. The impedance of such a circuit is given by:

$$Z(\omega) = \left(R_0^{-1} + i\omega C\right)^{-1} + i\omega L \tag{2.16}$$

where L and C are the series inductance and shunt capacitance values, respectively. Proper matching requires solving Eqn. 2.16 under the condition:

$$Z(\omega_0) = 50 + 0i\ \Omega \tag{2.17}$$

where ω_0 is the center of the measurement band. Fig. 2.10 shows a plot of the real and imaginary components of Eqn. 2.16 with $R_0 = 1\ k\Omega$. For the right choice of C and L, the imaginary part of the complex impedance crosses zero when the real part is $50\ \Omega$. Combining Eqn. 2.16 and Eqn. 2.17 for a given R_0, ω_0 and Z_0 gives us the needed inductance and capacitance values.

$$L = \sqrt{\frac{R_0 Z_0}{\omega_0^2}} \qquad C = \frac{1}{\sqrt{R_0 Z_0 \omega_0^2}} \tag{2.18}$$

While in theory adding a precise inductance and capacitance to a device is straight forward, in practice real devices can have a not insignificant amount of stray capacitance[†]. To account for this we can use a variable capacitor and tune the matching circuit to each device. One simple, temperature

[†]stray inductance is also possible (particularly if long wire bonds are necessary) but is usually negligible for the resistance and frequency ranges in this thesis

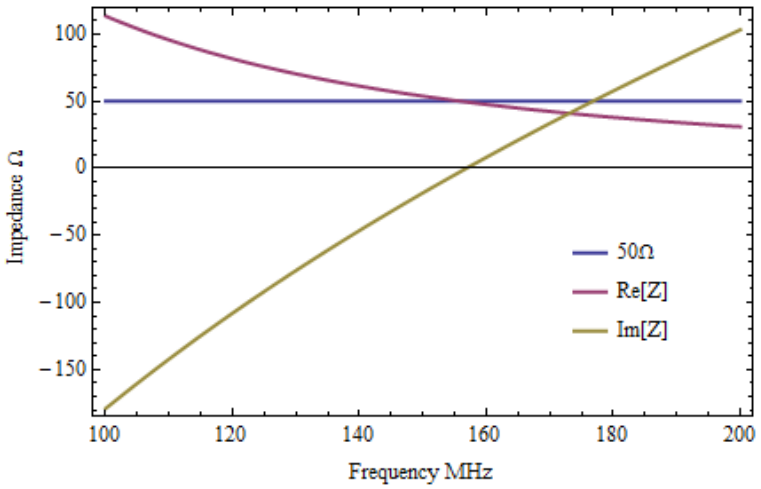

Figure 2.10: The real and imaginary impedance of an LC tank circuit (Eqn. 2.16) with $R_0 = 1\,k\Omega, C = 4.5\,pF$, and $L = 220\,nH$. The imaginary component cross zero as the real component is 50 Ω.

independent, magnetic field compatible capacitor that can be easily tuned is a set of twisted pair wires. Fig. 2.11 shows an example of a matching circuit using a twisted pair capacitor before and after tuning.

A vector network analyzer (VNA) is used to measure the sample reflectance $\Gamma^2 = S_{11}^2$ to ensure the sample is properly matched. Fig. 2.12 shows how the reflectance changes for a 1 $k\Omega$ sample resistance and 220 nH series inductance as the capacitance is tuned. When properly tuned we measure a large dip in S_{11}^2 signifying the sample is well coupled to the 50 Ω transmission line.

After matching, the noise spectral density emitted into the measurement circuitry is no longer flat but instead shaped by Γ in accordance to Eqn. 2.13. This point becomes clear when looking at the noise spectra emitted by an impedance matched sample at various temperatures — as shown in Fig. 2.13. Two features of these spectra stand out prominently: first, the background noise is no longer flat but has structure and, second, the increase in noise as the sample temperature is raised

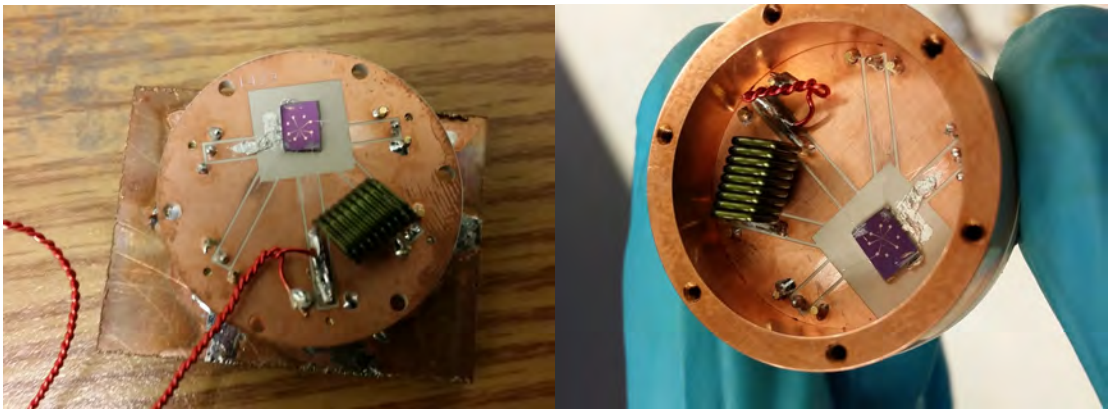

Figure 2.11: Images of an impedance matching circuit before (**left**) and after (**right**) capacitance tuning. A long piece of twisted pair wire shunts the sample and an inductor (Coilcraft RF Air Core) is placed in series. To tune the capacitance, the twisted pair wire is cut shorter and shorter while the reflectance is monitored.

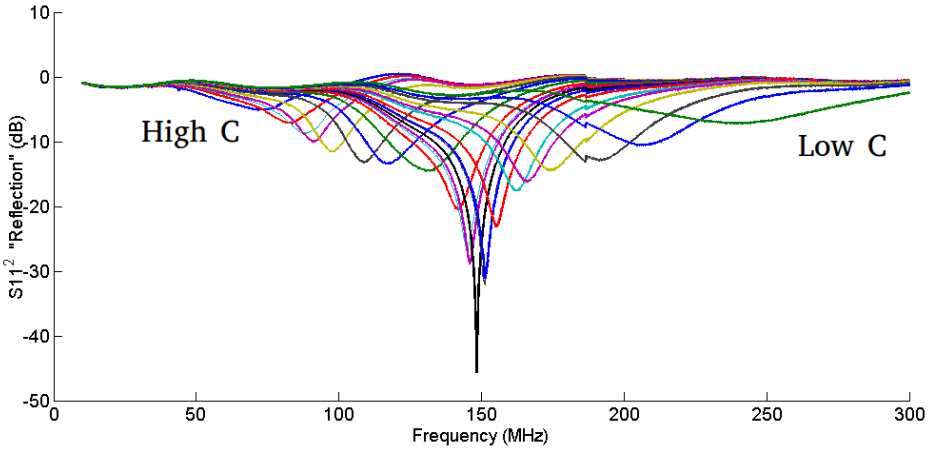

Figure 2.12: Reflectance curves while tuning a matching circuit for $R_0 = 1\,k\Omega$ and $L = 200\,nH$. The rightmost curve (green) corresponds to the lowest capacitance and the leftmost curve (blue) corresponds to the highest. Each curve is the result of cutting off a section of twisted pair wire as shown in Fig. 2.11.

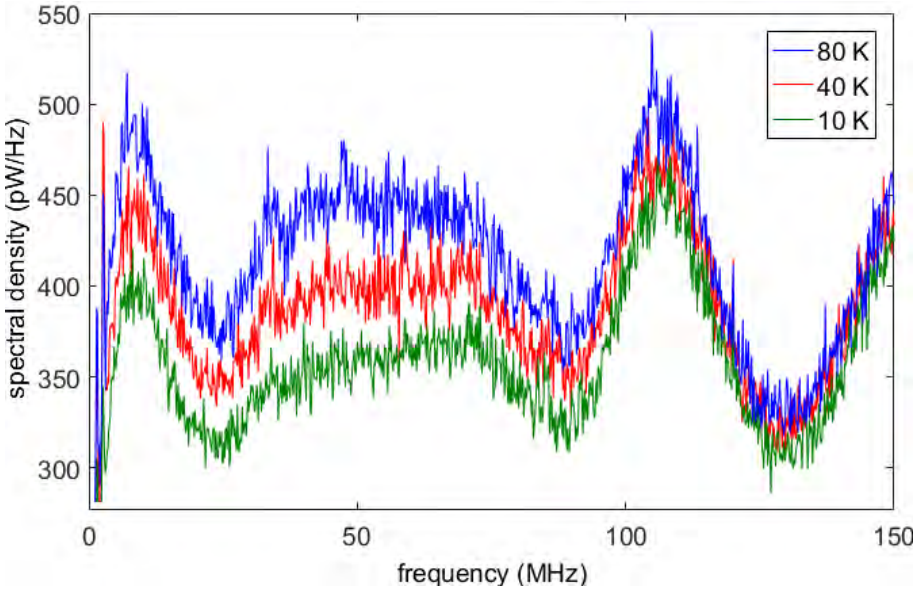

Figure 2.13: Amplified noise spectrum from a device, impedance matched using an LC tank circuit, at various temperatures. The background noise is no longer flat as the amplifier is not properly terminated at all frequencies. As the device temperature is raised, the spectral density increases non-uniformly as different frequencies couple differently to the circuitry as determined by Eqn. 2.13

is not the same at all frequencies. The result is that we are no longer free to select just any measurement bandwidth but must carefully choose filters suited to the reflection profile.

In most mesoscopic measurements, the resistance of the device under test varies throughout the experiment; whether electrostatic gates modulate the carrier density, strong magnetic fields drive the system into quantum hall, or cryogenic temperatures modify the conductivity, matching networks should operate over a wide dynamic range of input impedances. The response of a single stage LC matching network coupled to a variable resistance device[†] is shown in Fig. 2.14. The device is optimally matched around $450\ \Omega$ but maintains more than $10\ dB$ coupling between $200\ \Omega$ and $1\ k\Omega$. As the resistance drops, we see the appearance of the trivial solution to Eqn. 2.16 of $R_0 = 50\ \Omega$ and

[†]in this case a graphene device modulated via an electrostatic gate

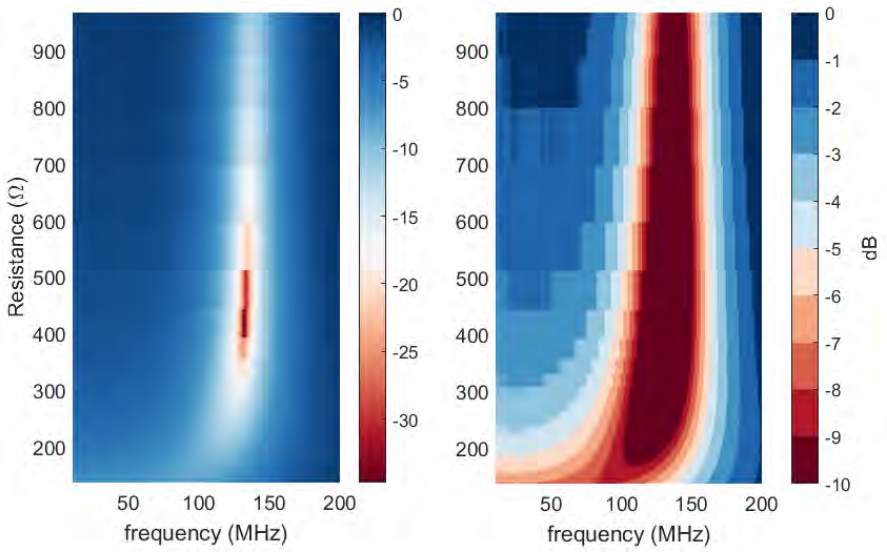

Figure 2.14: Reflection coefficient $|S_{11}|^2$ for a single stage LC matching network as a function of device resistance. The left plot shows the full data set with a maximum coupling efficiency of more than $30\,dB$. The right plot shows the same data with the color scale adjusted to highlight $1\,dB$ changes up to a maximum of $10\,dB$ (corresponding to 90% coupling efficiency). All data taken from a graphene device at low temperature using an electrostatic gate.

$\omega = 0\,Hz$.

2.6.2 Multi-stage matching

Magneto-thermal transport studies discussed in chapter 8, require devices to vary in resistance over multiple ordered of magnitude. Single stage LC networks are insufficient to cover this wide range. Fig. 2.15 shows the loss of coupling in a single stage LC tank circuit at high device resistances. In this situation, multiple LC stages can be used to increase the dynamic range.

Multi-stage LC networks allow you to match a wider area of the resistance-frequency space[†] by

[†]This is a well known solution to a similar problem in audio recording. Multi-stage impedance transformers are used to capture the full audio range [12].

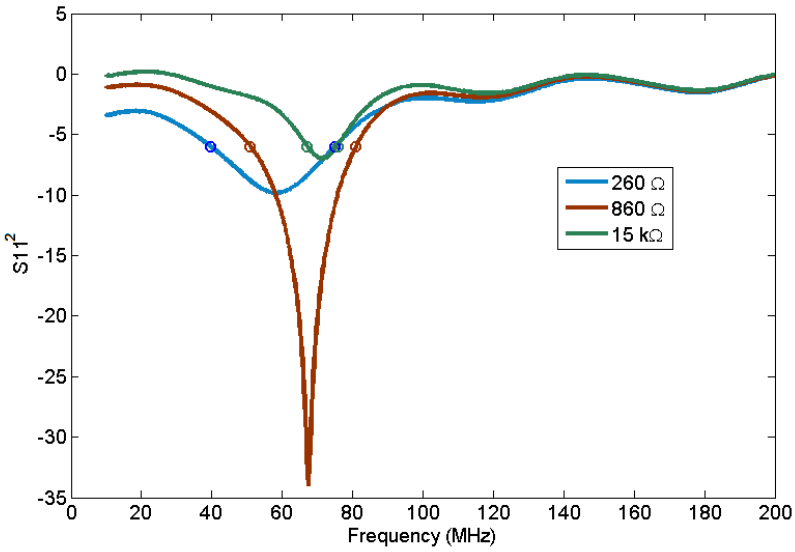

Figure 2.15: Reflection measurements of a single stage LC tank circuit coupled to a graphene device at different resistances. At high resistance the coupling drops off and reflection is high.

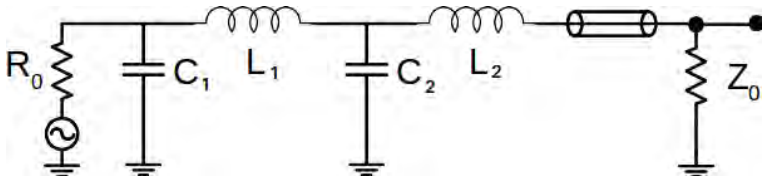

Figure 2.16: Schematic of a double-stage LC matching network. The device resistance R_0 is transformed to match the characteristic impedance of the measurement circuit Z_0 using two LC tank circuits. This results in a wider matching bandwidth and/or larger dynamic range depending on the values of the reactive elements.

giving you multiple solutions to the equation $Z(\omega) = Z_0$. An example schematic of a two-stage LC tank circuit is shown in Fig. 2.16. The resulting impedance takes the form:

$$Z(\omega) = \left\{ \left[\left(R_0^{-1} + i\omega C_1 \right)^{-1} + i\omega L_1 \right]^{-1} + i\omega C_2 \right\}^{-1} + i\omega L_2 \tag{2.19}$$

Eqn. 2.19, under the constraint defined by Eqn. 2.17, can have multiple solutions for the same set

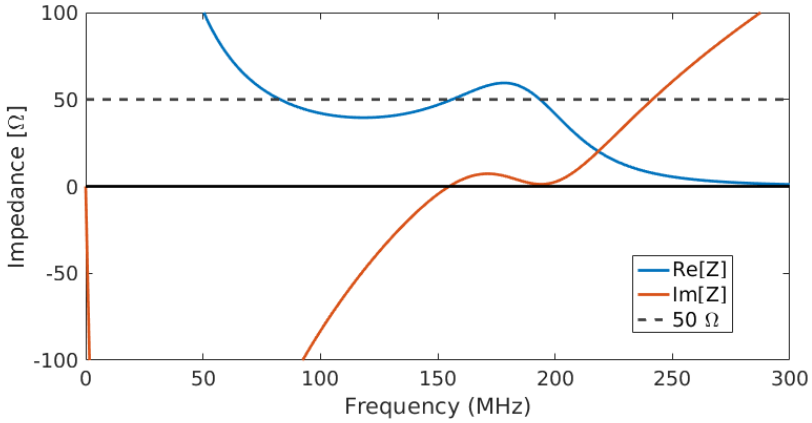

Figure 2.17: Real and imaginary components of Eqn. 2.19 for $R = 1\,k\Omega, C_1 = 1.9\,pF, L_1 = 430\,nH, C_2 = 8.6\,pF$, and $L_2 = 96\,nH$. The impedance goes to $50 + 0i\ \Omega$ at two nearby frequencies.

of inputs. This makes it possible to increase the matching bandwidth for the same dynamic range. Fig. 2.17 plots the real and imaginary components of Eqn. 2.19 for a specific choice of inductances and capacitances designed to cross $50+0i\ \Omega$ at two nearby frequencies for the same device resistance. It can be shown for a fixed resistance that the maximum bandwidth occurs when the impedance is dropped by geometric factor [9] — i.e each stage transforms the impedance by the same multiplicative factor. For an N stage network of the form shown in Fig. 2.16, the ith inductance and capacitance are given by a generalized form of Eqn. 2.18.

$$L_i = \frac{\left(R_0^{2N-2i+1}\, Z_0^{2i-1}\right)^{1/2N}}{\omega_0} \qquad C_i = \frac{\left(R_0^{2N-2i+1}\, Z_0^{2i-1}\right)^{-1/2N}}{\omega_0} \tag{2.20}$$

Applying Eqn. 2.20 to a two-stage LC network with a graphene device we can increase the matched bandwidth to $\sim 150\ MHz$, as shown in Fig. 2.18.

However, if instead we want to match to larger range of resistances, we can move one of the so-

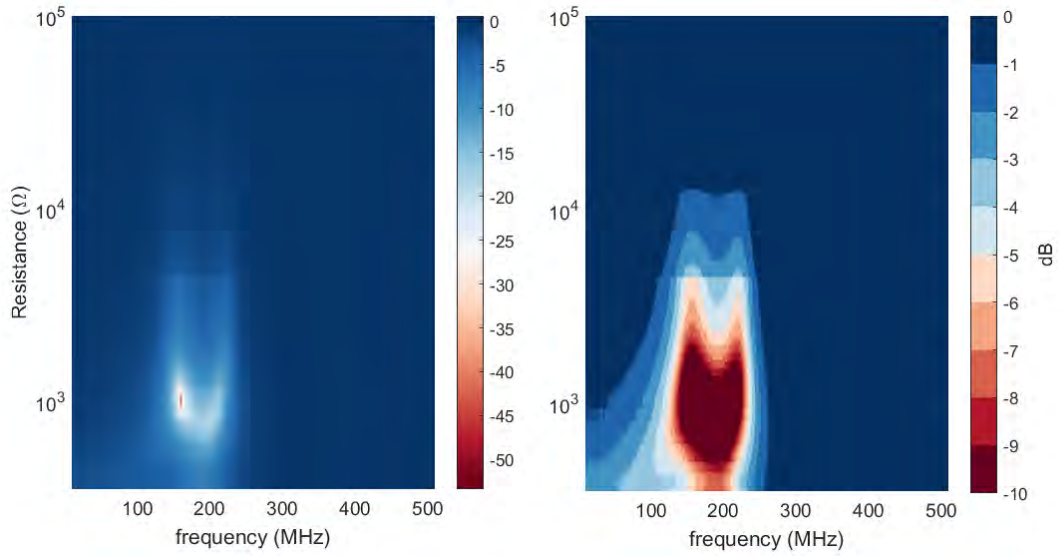

Figure 2.18: Measured reflection coefficient $|S11|^2$ for a double stage LC matching network as a function of device resistance for reactive components following Eqn. 2.20. The left plot shows the full data. The right plot shows the same data with the color scale adjusted to highlight 1 dB changes up to a maximum of 10 dB. The attached graphene device is optimally coupled at $\sim 1\ k\Omega$ and has an effective noise bandwidth of $\sim 150\ MHz$.

lutions to Eqn. 2.19 to a higher resistance. This increases the dynamic range of the matching circuit at the expense of bandwidth. For example, by lowering the first capacitance of the network shown in Fig. 2.18, we move the high frequency solution from $\sim 1\ k\Omega$ to $\sim 4\ k\Omega$, increasing the dynamic range to include quantum hall resistances, as shown in Fig. 2.19.

The more stages added the wider the matched area in resistance-frequency space but also the more sensitive to stray capacitance the circuit becomes. In practice, devices with a 300 nm SiO_2 back-gate dielectric often have $3 - 6\ pF$ stray capacitance; this can be reduced to less than $1\ pf$ with the use of insulating substrates and local top-gates, or by increasing the back-gate dielectric to $1\ \mu m$. Reducing the stray reactance also addressed the another challenge that comes with multiple match-

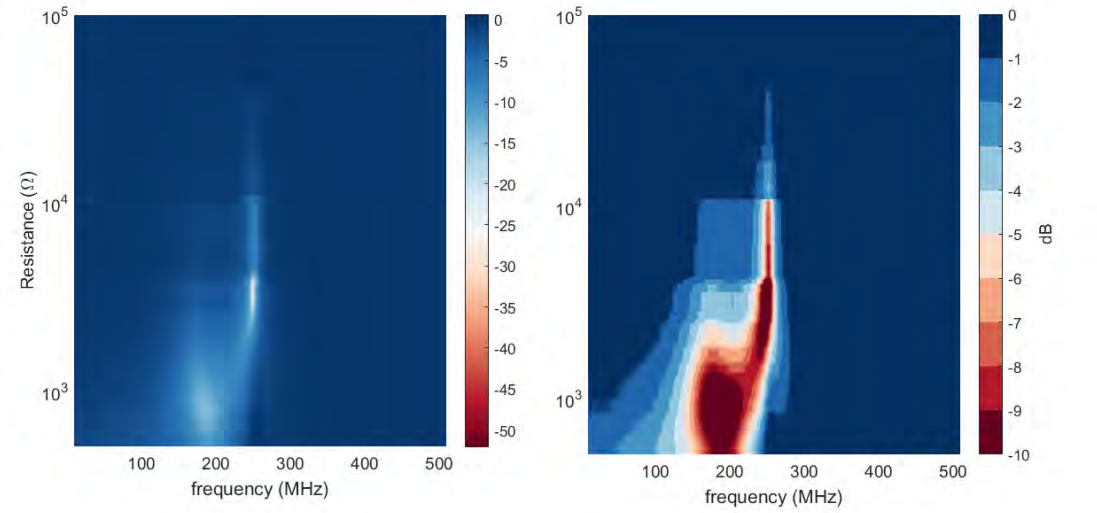

Figure 2.19: Measured reflection coefficient $|S11|^2$ for the same double stage LC matching network shown in Fig. 2.18 as a function of device resistance with the first stage capacitance lowered. This moves the high frequency solution to a higher resistance; effectively increasing the dynamic range at the cost of bandwidth. This technique enables the continuous measurement of graphene devices from zero field into the quantum Hall regime

ing stages — it is no longer trivial to tune the circuit using a gimmick[†]. For these more complicated networks, surface mount ceramic capacitors can be soldered directly to the sample package, as shown in Fig. 2.20, and adjustments can be made by careful removal and replacement[‡].

2.7 System noise temperature

A factor of two in signal to noise can be the difference between graduating in two years and eight. From the Dicke radiometer formula, Eqn. 2.15, the measurement time scales as the system noise temperature squared. Each component of the measurement circuit should be chosen with this

[†]twisted pair wire is one form of a gimmick used to fine tune the circuit capacitance
[‡]making sure to only apply heat the capacitor locally to avoid damaging the sample.

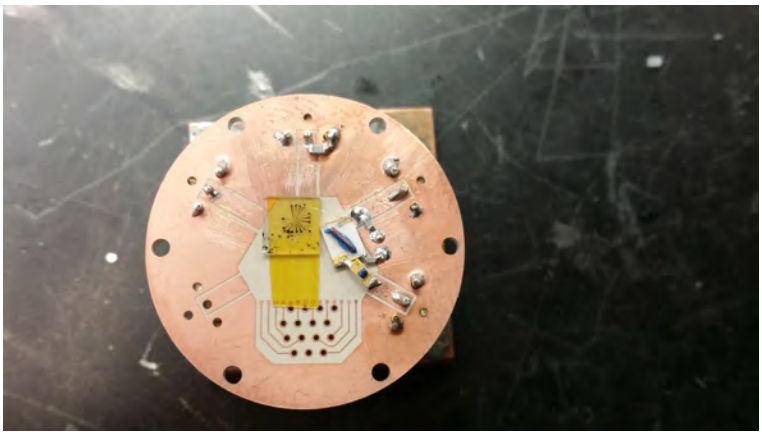

Figure 2.20: Image of a two-stage LC matching network soldered directly to a custom cryogenic sample package and wire-bonded to a graphene device. Inductive elements have gold leads allowing direct wire-bonding. The sample is placed on an insulating sapphire substrate with a local top-gate to reduce the stray capacitance.

in mind and, as such, it is important to understand how each element affects the system as a whole.

The system noise temperature, T_n, is the temperature at which your sample emits the same noise power as the sum of all the "unwanted" noise in your system — i.e. your signal to noise ratio is given by T/T_n, where T is the sample temperature. Quantifying noise in this way lets us write the output voltage of our circuit, V_{out}, (which is proportional to the integrated noise power) as:

$$V_{out} = \mathcal{G}(\Gamma)(T + T_n(\Gamma)) \tag{2.21}$$

where Γ^2 is reflection coefficient between the sample and the amplifier and $\mathcal{G}$ is a generalized gain factor set by the LNA amplification together with the insertion loss of the microwave components integrated over the bandwidth defined by the external filters. In general, both $\mathcal{G}$ and T_n are functions of Γ. All defining characteristics of a given measurement circuit can be swept into T_n and $\mathcal{G}$. In principle these factors must be measured but reasonable estimates can aid in the circuit design.

It is useful to distinguish the difference between the intrinsic noise temperature T_0^n and the system noise temperature T_n. T_0^n corresponds to the noise emitted by the circuit relative to the Johnson noise of a perfectly matched resistor, while T_n is relative to the sample being measured — i.e. T_0^n can be reported on a device's specification sheet while T_n is a function of the sample under test and can therefore change with experimental parameters such as electrostatic gate voltage and external magnetic field. In general T_n is always equal to or greater than T_0^n.

While T_0^n is primary determined by the front-end amplifier, every component, i, with a finite intrinsic noise T_i^n contributes an amount inversely proportional to the gain before that component, G_i. For example, if a circuit has three amplification stages with gains G_1, G_2, and G_3 with intrinsic noise temperatures T_1^n, T_2^n, and T_3^n, respectively, the total system intrinsic noise value is given by:

$$T_0^n = T_1^n + \frac{T_2^n}{G_1} + \frac{T_3^n}{G_1 G_2} \tag{2.22}$$

or in general

$$T_0^n = \sum_i \frac{T_i^n}{\prod_{j<i} G_j} \tag{2.23}$$

Hence, if the front-end amplifier has a gain or 30 dB, the noise from second amplifier is effectively reduced by a factor of $1,000$.

Estimating T_n from T_0^n requires knowing the matching function characterized by Γ. If Γ is frequency independent then $T_n \approx T_0^n/(1-\Gamma^2)$. For arbitrary $\Gamma(\omega)$ you can integrate over the

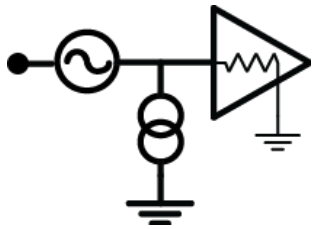

Figure 2.21: Schematic of a common noise model for active elements. A random voltage source is added in series with the signal and a random current source is added in parallel.

bandwidth defined by external filters Δf[†].

$$T_n \approx \frac{1}{\Delta f} \int_{\Delta f} \frac{T_n^0}{1 - \Gamma^2(\omega)} d\omega \tag{2.24}$$

The above formulation is approximate as it assumes the system's intrinsic noise can be described entirely by a single parameter T_0^n — a good assumption if the sample is properly matched. However, in general active components require two parameters to fully capture the noise behavior. A common technique is to model the circuit with an effective series voltage noise and parallel current noise, as shown in Fig. 2.21. However, an equivalent description, which is often more useful in microwave experiments, is that of a forward traveling noise power, T_{for}^n, a reverse traveling noise power T_{rev}^n, and some correlation between them. In the case of perfect matching, $\Gamma \rightarrow 0$, T_{rev}^n is completely absorbed. However for finite Γ we can write the amplified noise as:

$$\langle P \rangle = G \left[T(1 - \Gamma^2) + T_{rev}^n \Gamma^2 + T_{for}^n \right] \tag{2.25}$$

[†]Eqn. 2.24 approximates the external filter function as a perfect square filter of bandwidth Δf. For the full calculation you must include the full filter function.

Rewriting this in the form of Eqn. 2.21 and solving for T_n and $\mathcal{G}$ yields.

$$T_n(\Gamma) = \frac{\Gamma^2}{1-\Gamma^2} T_{rev}^n + \frac{1}{1-\Gamma^2} T_{for}^n \tag{2.26}$$

and

$$\mathcal{G}(\Gamma) = G(1-\Gamma^2) \tag{2.27}$$

Eqn. 2.26 is what determines the measurement uncertainty and therefore the speed of the measurement. An interesting consequence of Eqn. 2.25 is that when the sample temperature is equal to T_{rev}^n, the total output noise has no dependence on Γ; no matter what resistance is being measured, the output noise power is the same! Fig. 2.22 shows the total noise power, Eqn. 2.25, as a function of sample resistance at several temperatures. The sample is optimally matche at $\sim 10^3\ \Omega$. In accordance with Eqn. 2.25, at low sample temperature the noise decreases as Γ decreases while at high temperature the noise increases as the sample approaches optimal matching. The spacing between curves is proportional to the generalized gain, $\mathcal{G}(\Gamma)$, which is maximized when Γ is minimized.

2.8 Calibration

Circuit losses and couplings are difficult to calculate a priori, and while T_n can be modulated away in a differential measurement, the generalize gain $\mathcal{G}(\Gamma)$ must be calibrated. If the

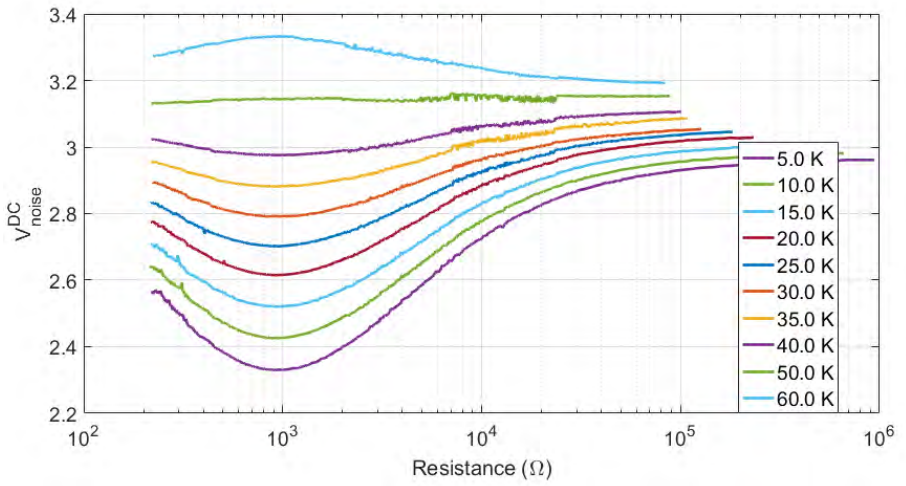

Figure 2.22: Voltage proportional to the total integrated noise power as a function of input sample resistance for different sample temperatures. The matching circuit is optimally matched (Γ is minimized) at $\sim 10^3\ \Omega$. At low temperature, the total noise decreases as Γ decreases, while at high temperature, the opposite is true. At $T \approx 50\ K$ the noise power is constant regardless of the input impedance in accordance with Eqn. 2.25 and $T^n_{rev} \approx 50\ K$.

output voltage is written in the form of Eqn. 2.21 then $\mathcal{G}$ is given by:

$$\mathcal{G}(\Gamma) = \left.\frac{dV_{out}}{dT}\right|_{\Gamma} \tag{2.28}$$

The challenge here is fixing Γ. If the device under test has a fixed resistance then calibration can be done by recording V_{out} for a few select bath temperatures. $\mathcal{G}$ is then given by the slope of a linear fit to $V_{out}(T)$. The inset of Fig. 2.6 shows $V_{out}(T)$ which was used to calibrate $\mathcal{G}$ yielding the main panel. However, most mesoscopic devices do not have a temperature independent resistance and thus more care must be taken in calibrating $\mathcal{G}(\Gamma)$.

The exact method of calibration will depend on the device characteristics and the size of the parameter space being measured. If the impedance of the device is sensitive to external parameters but

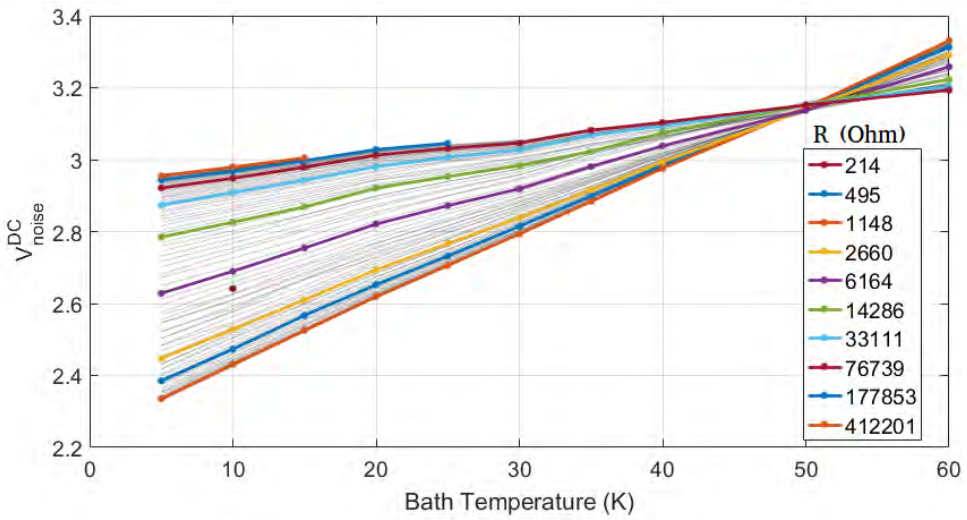

Figure 2.23: Output voltage proportional to the integrated noise given by Eqn. 2.21 as a function of device temperature with fixed resistance. The slope of each line gives the generalized gain $\mathcal{G}(R)$ while the extrapolated offset (divided by $\mathcal{G}$) is $T_n(R)$. The external parameters (e.g. gate voltage, magnetic field, etc.) that result in a given resistance are generally different for different bath temperatures.

only has a weak dependence on temperature — i.e. $|\mathrm{d}\Gamma/\mathrm{d}T|$ is small and $V_{out}(T)$ is locally linear on a reasonable experimental scale — then calibration can be done by taking local derivatives of $V_{out}(T)$ everywhere in the parameter space. While this method is straight forward to implement, it has several glaring drawbacks. Firstly, the time required to find local derivatives for the entire parameter space scales exponentially in the number of parameters. Secondly, it requires knowing the exact parameters that will be measured ahead of time; if during the course of an experiment the parameter space must be expanded or higher resolution is required, calibration must be done again.

A more robust method is to simultaneously measure both V_{out} and Γ and then numerically solve for $\mathrm{d}V_{out}/\mathrm{d}T$ for fixed Γ. Whats more, if the right reactive elements are used for impedance matching, Γ becomes a function of only the sample resistance and fixing Γ is equivalent to fixing

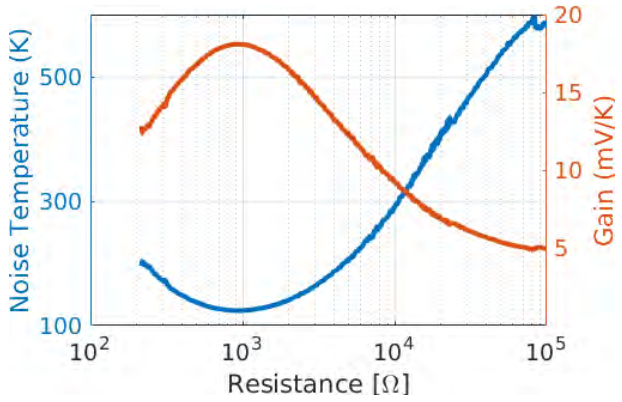

Figure 2.24: Generalize gain and effective noise temperature exracted from data shown in Fig. 2.23. The circuit is designed to optimally match an input resistance of $\sim 1 k\Omega$. As expected from Eqn. 2.26 and 2.27, the gain is maximized and the noise temperature is minimized when the device is effectively coupled — i.e. Γ is minimized. This two-stage LC tank circuit shows effective coupling over 3 orders of magnitude of input resistance.

R. Fig. 2.22 shows V_{out} as a function of device resistance for various temperatures. It is important to note that each temperature curve is a collection of many different parameter sweeps that all collapse onto one smooth curve — i.e. it does not matter if the sample is $13\ k\Omega$ due to electrostatic gating at zero magnetic field, or due to the quantum Hall effect, the emitted noise is the same. If we attempt to fix external parameters and raise the temperature the output voltage is nonlinear, but if instead we fix the two-terminal resistance we arrive at Fig. 2.23. Linear fits to each line then give $\mathcal{G}$ as the slope and T_n as the offset[†]. For the data shown in Fig. 2.23, the gain and noise temperature are shown in Fig. 2.24; as expected the gain in maximized and the noise temperature is minimized at $R \sim 1\ k\Omega$ where the sample is optimally matched. This particular data was taken from a two-stage matching network coupled to a graphene device and shows a dynamic range of ~ 3 orders of magnitude in device resistance.

[†]negative T_n is where the linear fit intercepts the horizontal axis; also given by the offset divided by the slope

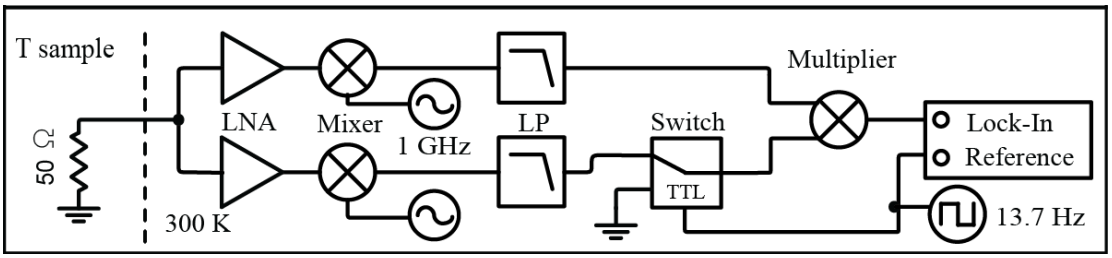

Figure 2.25: High level schematic of a typical Johnson noise thermometry cross-correlation measurement circuit. Noise from an impedance matched sample is sent into two independent measurement lines. Each line is then amplified, a measurement bandwidth is selected, and the signals are combined using a linear multiplier. A microwave switch acts as a chopper and the signal is integrated using a lock-in amplifier.

2.9 Cross-correlated noise thermometry

A challenge in noise measurements is isolating the noise you want to measure from the noise you don't. Dissipation between the resistive load and the LNA, such as coaxial attenuation and contact resistance, can contaminate thermal transport measurements [13, 14]. Johnson noise from the sample is added to the unwanted Johnson noise from these lossy components. Cross-correlation techniques can mitigate this problem by amplifying the Johnson noise signal of interest independently via two separate measurement lines [14, 15, 16, 17, 18] and discarding uncorrelated noise between the two channels. The output voltage of such a scheme can be written as:

$$V_{out} \propto \langle (V_{JN} + V_{n1}) \times (V_{JN} + V_{n2}) \rangle \tag{2.29}$$

$$V_{out} \propto \langle V_{JN}^2 \rangle + \langle V_{JN} V_{n1} \rangle + \langle V_{JN} V_{n2} \rangle + \langle V_{n1} V_{n2} \rangle \tag{2.30}$$

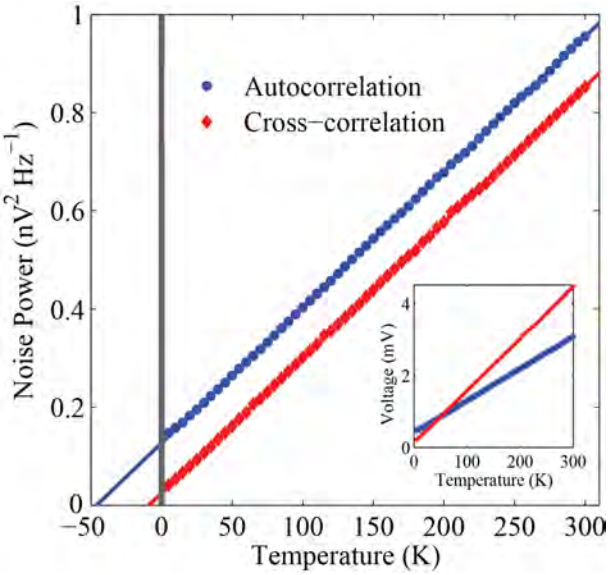

Figure 2.26: Auto- and cross-correlation Johnson noise measurements of a $50\ \Omega$ resistor measured by the circuit shown in Figs. 2.2 and 2.25, respectively. Inset shows the raw output voltage. The signal is converted to noise power by the Nyquist equation. The solid lines are linear fits, where the auto- and cross-correlation data exhibit an offset of $68\ K$ and $2.6\ K$, respectively, due to amplifier noise

where V_{JN} is the instantaneous Johnson noise voltage and V_{n1} and V_{n2} are the instantaneous voltage noise on the two channels. If all noise sources are uncorrelated then only the first term in Eqn. 2.30 is non zero and $V_{out} \propto \langle V_{JN}^2 \rangle$.

Previously, cross-correlation measurements were limited to frequencies below a few MHz due to the practical implementation of multipliers and digital processing speeds [17, 18, 19, 15]. However, the 2 GHz analog multiplier (Analog Devices ADL5931) and LNA, combined with the lock-in amplifier modulation scheme described in Fig. 2.25, measure the correlated noise between the two channels, rejecting a large portion of the uncorrelated amplifier noise. The results are shown alongside an autocorrelation measurement (Fig. 2.2) for comparison in Fig. 2.26; the offset due to amplifier noise was reduced from $68\ K$ to $2.6\ K$.

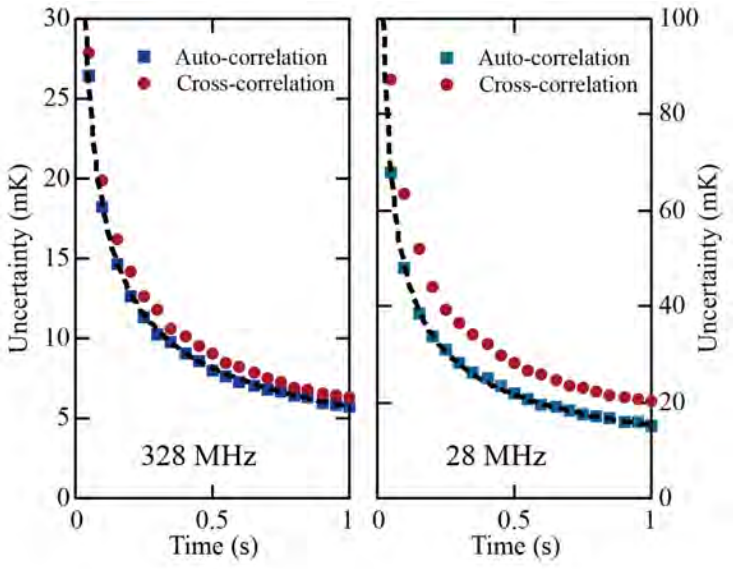

Figure 2.27: Standard deviation of 1000 auto- and cross-correlation temperature measurements as a function of integration time for $328\ MHz$ (left) and $28\ MHz$ (right). In all cases, uncertainty follows the Dicke relation, Eqn. 2.15, scaling as $\sqrt{\tau}$ and $\sqrt{\Delta f}$. Data is taken from a $50\ \Omega$ resistor

Although the offset in the data is reduced by cross-correlation, the measurement time required to achieve a given precision is not reduced[†]. The time required to effectively average out the uncorrelated noise is still proportional to the amplifiers noise temperature. To be precise, T_n is given by the geometric mean of individual amplifiers noise temperatures.

$$T_n = \sqrt{T_{n1} T_{n2}} \tag{2.31}$$

where T_{n1} and T_{n2} are the system noise temperatures of the two measurement lines. Using two LNAs with similar specifications Eqn. 2.31 reduces to the Dicke formula, Eqn. 2.15. Fig. 2.27 illustrates this point by showing the standard deviation of 1000 temperature measurements as a func-

[†]Cross-correlation can improve the accuracy of an experiment but not the precision

Figure 2.28: Cartoon of a four-terminal device. If the voltage between terminals A and C is cross-correlated to the voltage between terminals B and D, the result will be more sensitive to the temperature of the device than pairing A-B and C-D

tion of integration time. Both auto- and cross-correlation measurements follow the Dicke formula with similar magnitude and uncertainty scaling as $\sqrt{\tau}$ and $\sqrt{\Delta f}$.

2.9.1 MULTI-TERMINAL CROSS-CORRELATION

CROSS-CORRELATION CAN BE USED TO REDUCE the effects of contact and lead resistance with the use of multi-terminal devices. However, as discussed in section 2.2, the voltage fluctuations on different pairs of terminals generally measure different areas of a device. For example, the four-terminal device drawn in Fig. 2.28 will give very different results depending on which terminal are paired — cross-correlation between V_{AC} and V_{BD} will by more sensitive to the device temperature than cross-correlation of V_{AB} and V_{CD}. The exact amount of overlap between the noise on any pair of terminals can be found via the method described in section 2.2.

3

Electronic cooling mechanisms in graphene

Charge carriers in conductors exchange energy with the environment in many ways. If an electronic system is directly heated — whether it be by Joule heating, optical pumping, or any other direct energy transfer — the mechanisms with which the system cools can be quite diverse. In mesoscopic samples there are typically three cooling mechanisms one has to consider. Firstly, if the ma-

terial is electrically connected to a thermal bath, such as macroscopic electrodes, then hot electrons can diffuse out and cold electrons can diffuse in; this diffusion is often referred to as Wiedemann-Franz cooling and is the dominate thermal transport mechanism in metals at low temperatures [20]. Secondly, hot electrons can transfer energy directly to the lattice by coupling to acoustic and optical phonon modes in the graphene itself or the nearby substrate (section: 3.2). Thirdly, electrons are charged and can therefore radiatively cool; this radiation is primarily in the form of Johnson noise and, although often negligible, can be the dominate cooling mechanism in ultralow temperature systems coupled to superconducting leads [21, 22].

3.1 Wiedemann-Franz

If a material hosts mobile charge carriers at a fixed temperature, each quasiparticle can transport a quantized amount of thermal energy and a quantized charge through the system; it then stands to reason that the electronic thermal conductivity must be related to the electrical conductivity. First observed at room temperature in 1853 by Wiedemann and Franz [23], the electronic thermal conductivity (κ) of metals is directly proportional to the electrical conductivity (σ) at room temperature. Twenty years later, Lorenz expanded upon the idea [24] and showed the ratio of the thermal conductivity to the product of the electrical conductivity and temperature (T) was a constant, $\mathcal{L}$.

$$\frac{\kappa}{\sigma T} = \mathcal{L} \tag{3.1}$$

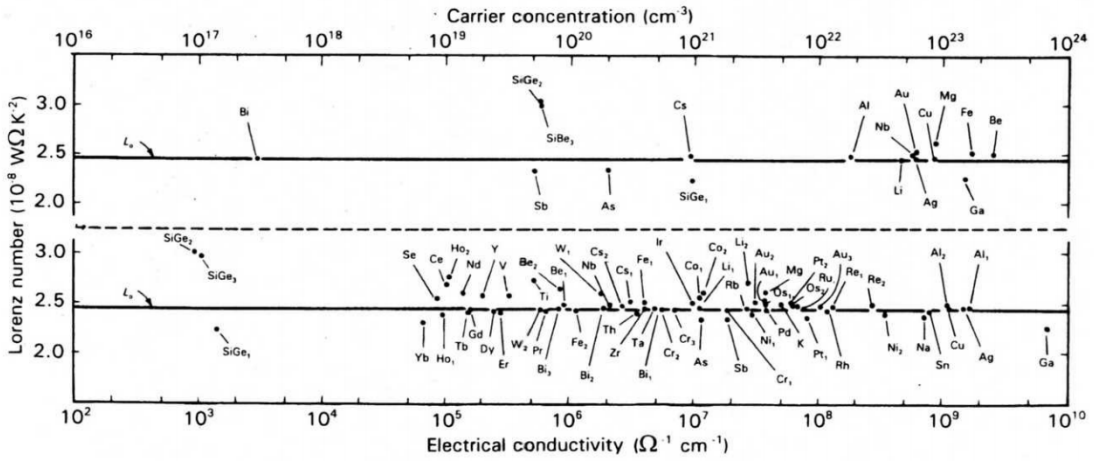

Figure 3.1: Experimental Lorenz number of elemental metals and degenerate semiconductors at low temperatures. Taken from ref [25], reprinted with permission from Springer, license number 4067330556225

Eqn. 3.1 is now known as the Wiedemann-Franz law (WFL) where $\mathcal{L}$ is the Lorenz ratio (also known as the Lorenz number). Fig. 3.1 shows experimentally measured Lorenz numbers for various metals and semiconductors as a function of conductivity and carrier concentration. The quantitative value for $\mathcal{L}$ can be approximated under the Drude model [20] but it was not until Sommerfeld in 1927 that a full derivation using Fermi-Dirac statistics was presented [26]. Under the assumptions of a degenerate Fermi gas and only elastic collisions, the theoretical value of the Lorenz number was shown to be:

$$\mathcal{L}_0 \equiv \frac{\pi^2}{3}\frac{k_B^2}{e^2} \approx 2.44 \times 10^{-8}\,\mathrm{W}\Omega/K^2 \tag{3.2}$$

The requirement that quasiparticles only scatter elastically leads the value of $\mathcal{L}$ to deviate from $\mathcal{L}_0$ in the presence of strong electron-electron scattering and inelastic electron-phonon scattering.

3.1.1 Linearization

To understand the behavior of devices under low energy excitations, it is useful to linearize the WFL. In the linear response regime the temperature variations across a device are small compared to the absolute temperature scale of the problem, T_b. For a uniform two-dimensional device connecting two thermal baths with temperatures $T_b \pm \Delta T/2$, the steady state thermal power transported via the WFL is given by:

$$\dot{Q}_{WF} = \left(\frac{W\sigma}{L}\right) \mathcal{L} T_b \, \Delta T = \frac{\mathcal{L} T_b}{R} \Delta T \tag{3.3}$$

where W and L are the sample width and length, respectively, and R is the two-terminal electrical resistance

3.1.2 Hot-electron shot noise

A common way to develop a temperature gradient is via Joule heating, where the electron temperature is raised with reference to the cold electrodes held at T_b. In the case of only WF conduction — i.e. no alternative cooling pathways such as phonons — the temperature rise in the high bias regime scales linear with the applied current, producing noise very similar to the shot noise seen in vacuum tubes. This well known effect is termed "hot-electron shot noise" [27, 28, 29] and can be

seen as the limit of the WFL with $T_e >> T_\mathrm{b}$.

$$\dot{\mathrm{Q}} \approx \frac{\beta \mathcal{L}}{R} T_e^2 \tag{3.4}$$

where β is a constant related to the temperature profile in the device. If we set the power dissipated to be proportional to the current squared, such that $\dot{\mathrm{Q}} = I^2 R$, we find:

$$\langle T_e \rangle \approx \frac{R}{\sqrt{\beta \mathcal{L}}} I \tag{3.5}$$

Solving for the temperature profile and the noise produced, eqn. 3.5 reduces to [27]:

$$S_I = \frac{\sqrt{3}}{4} 2e\, I \tag{3.6}$$

Eqn.3.6 has the same form as shot noise with Fano factor of $\sqrt{3}/4$.

3.2 Electron-Phonon coupling

At higher temperatures, the cooling of hot electrons is dominated by coupling to acoustic and optical phonons in the hexagonal lattice as well as the nearby substrate [30, 31]. In many experiments involving optical heating or Joule heating, a quasi-equilibrium can be formed where the electron temperature and the lattice temperature can be different. In the particular case of monolayer

graphene this is especially true as the high phonon conductivity and relatively weak electron-phonon coupling can result in a lattice temperature that is well thermalized to the thermal bath (T_b), but an electron temperature (T_e) which is not. The interaction between these fermionic and bosonic systems in graphene is quite rich with even the power law for the temperature dependence varying depending on the Fermi level, device disorder, and bias voltage. A general form for the heat transfer between the two systems can written as:

$$\dot{Q}_{e-ph} = \mathrm{A}\,\Sigma_{e-ph}\left(T_e^{\,\delta} - T_\mathrm{b}^{\,\delta}\right) \tag{3.7}$$

where A is the area of the device, Σ_{e-ph} is a coupling constant, and δ is the is the power law exponent. Depending on the mechanism δ can vary between 3 [32, 33] in disordered samples, or $4-5$ in clean devices [30, 31]. These relatively high power laws result in phonons dominating at high temperature but becoming negligible when cold.

3.2.1 Linearization

To find the linear response behavior ($\Delta T \ll T_\mathrm{b}$) we can Taylor expand to first order for $T_e \approx T_\mathrm{b}$ to find:

$$\dot{Q}_{e-ph} \approx \mathrm{A}\,\delta\,\Sigma_{e-ph} T_\mathrm{b}^{\,\delta-1}\,\Delta T \tag{3.8}$$

Eqn. 3.8 can be compared directly to eqn. 3.3. First we see that while both cooling mechanisms scale as the device width, they have inverse dependences on the device length and, therefore, the bath

temperature at which one mechanism will dominate over the other is geometry dependent.

The literature on electron-phonon coupling in graphene is vast [34, 35, 30, 31, 36]. Here I present a condensed review of the main mechanisms relevant to the experiments presented in this dissertation.

3.2.2 Bloch-Grüneisen temperature

In most three-dimensional metals, where the Fermi surface is large, the characteristic temperature scale for phonon dynamics is given by the Debye temperature. However, in semiconductors and semimetals the Fermi surface can be substantially smaller than the Brillouin zone leading to a second temperature scale which governs the scattering of electrons and phonons. The Bloch-Grüneisen temperature, T_{BG}, is the temperature at which the most energetic phonons have a typical momentum equal to the Fermi momentum[37, 38].

$$T_{BG} = \frac{2\hbar v_s k_F}{k_B} \tag{3.9}$$

Above this temperature, momentum conservation dictates that only a fraction of the available phonon modes can scatter electrons. This is because the largest momentum change an electron can experience is $2k_F$ — a complete backscatter — and, as such, only phonons with momentum equal to or less than $2k_F$ can participate in scattering processes. This has been shown in GaAs based 2D electron systems [39] and in graphene [40] where T_{BG} can be controlled by tuning the Fermi level

using an electrostatic gate.

3.2.3 Acoustic phonons

In typical metals at low temperature, the dominate phonon modes in the system are acoustic [20]†. In graphene, however, energy transfer between electrons and these acoustic phonons (AP) is limited by the mismatch between the Fermi velocity (v_F) and the sound speed in the material (v_s). Energy and momentum conservation limit the energy that each phonon collision can remove from the electronic system, resulting a maximal energy transfer of $2\hbar v_s k_F$ per collision. Nevertheless, experiments have shown that the electronic cooling in many graphene devices at low temperatures is dominated by AP scattering [41, 42, 43] .

Theoretical predictions for the the power law δ and the coupling constant Σ_{e-ph} have been shown to depend upon the device temperature and the amount of disorder. In the dirty limit, the energy and momentum conservation discussed above can be circumvented by disorder-assisted collisions called "supercollisions" resulting in a power law $\delta = 3$ [32]. In the clean limit at low temperature, Kubakaddi [44] showed $\delta = 4$ with a coupling constant:

$$\Sigma_{e-ap} = \frac{\pi^2 \mathcal{D}^2 |\mu| k_B^4}{15\rho\hbar^5 v_F^3 v_s^3} \tag{3.10}$$

where $\mathcal{D}$ is the deformation potential, μ is the chemical potential, and ρ is the mass density of the

†The optical phonon branch has finite energy at $k = 0$ and thus at low enough temperatures these modes are frozen out

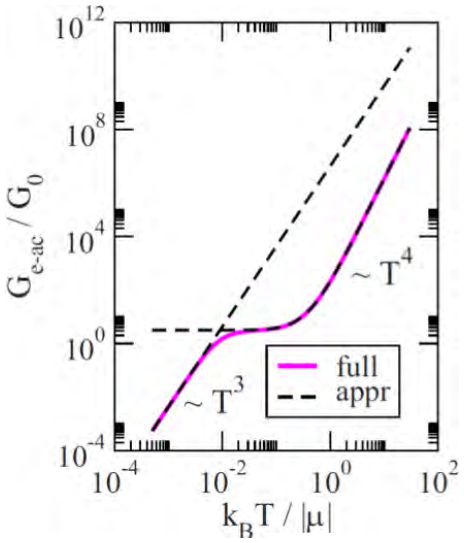

Figure 3.2: Numerical calculations of the thermal conductance between graphene electrons and acoustic phonons as a function of temperature normalized to the chemical potential (μ). the thermal conductance G scales as $T^{\delta-1}$. $G_0 \propto \mu^4$ is a temperature independent normalization constant. For temperatures below T_{BG} the electron-phonon power law δ scale as T^4 while at high temperature Viljas et al. find $\delta \sim T^5$. Reprinted with permission from Ref. [30] by the American Physical Society license number: 4077361227141.

lattice. Eqn. 3.10 was reproduced by Viljas et al. [30] and extended to high temperature where it was found that δ approaches 5. The transition from these two regimes is shown in fig. 3.2.

3.2.4 Optical phonons

Although the energies associated with optical phonons in graphene are quite large compared to the thermal energies in typical low temperature experiments, each collision can remove a significant amount of energy from the electronic system. Bistritzer et al. [31] showed that, at sufficiently high temperatures, even the $\sim$200 meV graphene intrinsic optical phonons can dominate the electronic cooling in suspended samples. For encapsulated devices, remote phonons in the

boron-nitride have been shown to have a surprisingly significant effect both theoretically [30, 31, 45] and experimentally [35]. At higher temperature ($\gtrsim 270\ K$), Sohier et al. [34] showed that despite the relatively low occupancy, graphene intrinsic optical phonons can have a more pronounced effect on the electrical resistance than acoustic phonons.

3.3 Photon cooling

For a device coupled to a microwave circuit, energy is radiated via photons over the measurement bandwidth [46, 47]. This is equivalent to 1D blackbody radiation and is the noise which is measured in Johnson noise thermometry. The power transferred is given by eqn. 2.13 and is considered to be negligible compared with the Wiedemann-Franz and phonon cooling powers for the temperatures and bandwidths covered in this dissertation. However, for devices at low temperature with superconducting leads this can become a significant source of cooling [47].

3.4 Thermal Network

When heat is injected into the electronic system of graphene, each of the mechanisms described above plays a role in thermalizing the system to an external bath. For the devices and experimental parameters used in this dissertation, a simplified thermal model can be used (illustrated in fig. 3.3). The electronic system is connected to the bath by two parallel cooling paths: a

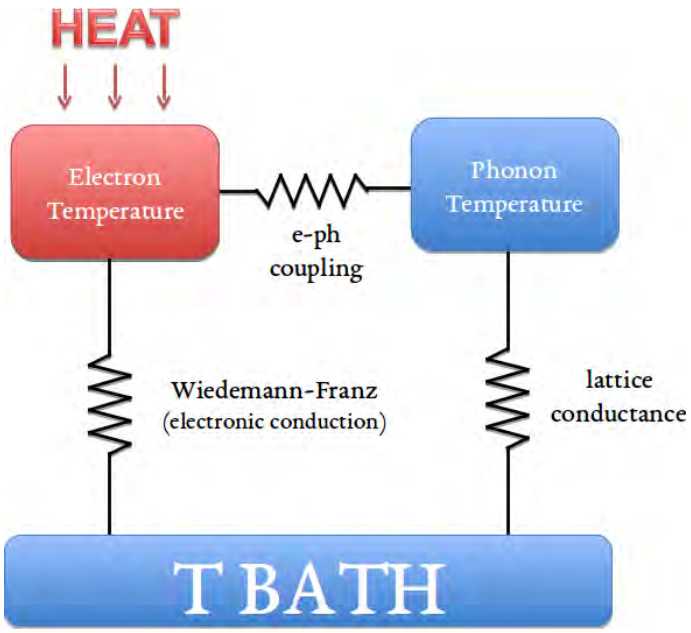

Figure 3.3: A thermal model of the electronic cooling pathways in graphene. Heat injected into the electronic system can flow directly to the bath via Wiedemann-Franz conduction, or to the lattice via electron-phonon coupling. The lattice and the bath are connected via the lattice conductivity which is large in graphene.

diffusion channel and a lattice channel. The diffusion channel is governed by the electronic thermal conductivity, while the lattice channel contains both an electron-phonon coupling term and the lattice conductivity of graphene. In practice the lattice conductance is typically many orders of magnitude larger than the electron-phonon conductance[†] resulting in the lattice being well sunk to the bath [10, 41, 48]. The temperature dependence of the two channels follow different power laws resulting in the low temperature behavior being governed by diffusive conduction while cooling at high temperatures is dominated by the lattice channel.

[†]The ratio of the lattice conductance to the electron-phonon conductance is geometry dependent. In long samples the phonon conductance may bottleneck the lattice cooling channel.

Since the dawn of time, man hath sought to make things

smaller.

4

Thermal conductance via electrical noise

A COMMON TECHNIQUE in studying the various cooling pathways in a mesoscopic sample is to inject a pulse of energy into the system and monitor the time dependent electron temperature as the system returns to equilibrium. However, these "pump-probe" experiments suffer from a few difficulties: Firstly, they yield a thermal time constant which is a convolution of the various heat capaci-

ties and thermal conductances in the problem. Secondly, the large temperature rise needed to resolve the thermal decay makes it difficult to study the linear response of low energy excitations. A steady state experiment avoids these difficulties and enables the measurement of thermal conductance in linear response at the expense of time-resolution.

In a steady state thermal experiment, a constant heating power, P_0, is injected into the electronic system and the electron temperature rise, ΔT, is measured. For the experiments in this dissertation, this is accomplished via Joule heating in a two terminal geometry while monitoring the change in Johnson noise temperature, T_{JN} — as discussed in chapter 2.2. We can define the ratio of the applied power to the change in the Johnson noise temperature as a thermal conductance:

$$G_{\text{th}} = \frac{P_0}{\Delta T_{JN}} \tag{4.1}$$

It is important to note that G_{th} is not the traditional thermal conductance which describes the total heat power flowing through a material in response to a spatial temperature gradient; it is instead a generalized thermal conductance describing the heat power transferred between the electronic system and the bath under Joule heating. To extract meaningful microscopic parameters from G_{th} it is necessary to model how the heat is entering and leaving the system as a function of these parameters. For the devices and experimental parameters presented here, the simplified thermal model shown in fig. 4.1 can be used to extract information about the electronic thermal conductivity and the electron-phonon coupling.

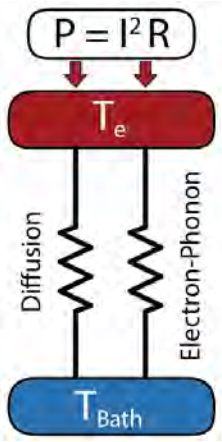

Figure 4.1: Simplified thermal diagram of the electronic cooling pathways in graphene relevant for the experimental conditions presented here. A current induces a heating power into the electronic system which conducts to the bath via two parallel pathways: diffusion and coupling to phonons.

4.1 Rectangular devices

For a two-terminal rectangular device, the temperature measured by Johnson noise — as given by Eqn. 2.12 with spatially uniform $\mathcal{P}(r)$ — is simply the spatially averaged temperature. Therefore, the total thermal power dissipated in linear response is then given by:

$$I^2R = P_0 = \dot{\mathrm{Q}} = \left(\frac{W}{L}\beta\kappa + WL\,\Sigma_{e-ph}\delta T_{\mathrm{b}}^{\delta-1}\right)\Delta T_{JN} \tag{4.2}$$

where W and L are the sample width and length, respectively, T_{b} is the bath temperature, κ is the electronic thermal conductivity, Σ_{e-ph} and δ are the electron-phonon parameters described in Ch. 3.2, and ΔT_{JN} is the Johnson noise temperature minus the bath temperature. In Eqn. 4.2 we have used the steady-state requirement that the total heating power entering the system equal the

total power transferred to the bath ($P_0 = \dot{\mathrm{Q}}$). The geometric factor β depends on the shape of the electronic temperature profile which is affected by the relative strength of the two cooling terms in Eqn. 4.2 and must be calculated.

4.1.1 Electronic conduction only

In the absence of phonons, the temperature profile, and therefore β, can be solved analytically. In a rectangular geometry, symmetry reduces the problem to one dimension (x) along the source-drain direction. For simplicity we assume that the graphene sample is homogeneous, that the approximately uniform electrical current is given by

$$\mathrm{J} = -\sigma \frac{\mathrm{d}V}{\mathrm{d}x} - \alpha \frac{\mathrm{d}T}{\mathrm{d}x} \tag{4.3}$$

and that the heat current is given by

$$\dot{q} = -\alpha T \frac{\mathrm{d}V}{\mathrm{d}x} - \bar{\kappa} \frac{\mathrm{d}T}{\mathrm{d}x} \tag{4.4}$$

where $\mathrm{d}T/\mathrm{d}x$ is the temperature gradient in the sample, $-\mathrm{d}V/\mathrm{d}x$ is the electric field in the sample, and α/σ is the Seebeck coefficient. From Eqn. 4.3 we see that the electrical conductivity, which is defined as the relation between the electric current and a potential gradient in the absence of a thermal gradient, is simply given by σ. Unfortunately, the thermal conductivity (κ) is not symmetrically de-

fined as the relation between the heat current and the thermal gradient in the absence of a potential gradient, but instead as the relation between $\dot{q}$ and $\mathrm{d}T/\mathrm{d}x$ in the absence of a charge current J. We therefore find:

$$\bar{\kappa} \equiv \kappa + \frac{T\alpha^2}{\sigma} = \kappa\,(1 + ZT). \tag{4.5}$$

In the latter equation, ZT is the thermoelectric coefficient of merit. In the limit of negligible thermo electric effects $\bar{\kappa} \approx \kappa$.

The continuity equation for the electric current yields:

$$0 = \frac{\mathrm{dJ}}{\mathrm{d}x} \tag{4.6}$$

In the linear response regime, the Joule power per unit length, $\mathcal{P}$, is given by $\mathrm{J} \cdot E$ and thus the continuity equation for the heat current with a source term becomes:

$$\mathcal{P} = \frac{\mathrm{J}^2}{\sigma} = \frac{\mathrm{d}\dot{q}}{\mathrm{d}x} \tag{4.7}$$

combining the above equations we obtain

$$\mathcal{P} = -\kappa \frac{\mathrm{d}^2 T}{\mathrm{d}x^2} \tag{4.8}$$

assuming that κ is approximately homogeneous throughout the sample.

The contacts serve as thermal baths and thus are held at the same temperature T_b. Writing

$$T(x) = T_b + \Delta T(x) \tag{4.9}$$

and solving Eqn. 4.8 using this form for the solution with the boundary conditions $\Delta T(0) = \Delta T(L) = 0$ we find a parabolic temperature profile:

$$\Delta T(x) = \frac{\mathcal{P}}{2\kappa} x(L - x) \tag{4.10}$$

The average temperature change in the sample, which is directly measured through Johnson noise thermometry, is

$$\Delta T_{JN} = \langle \Delta T \rangle = \int_0^L \frac{\mathrm{d}x}{L} \, \Delta T(x) = \frac{\mathcal{P} L^2}{12\kappa} \tag{4.11}$$

Plugging in the power per unit length $\mathcal{P}$ in terms of σ and the external voltage V_0 yields:

$$\Delta T_{JN} = \frac{V_0^2 \, \sigma}{12 \, \kappa} \tag{4.12}$$

We find ΔT_{JN} to be independent of the sample dimensions. This non-uniform temperature profile is illustrated in Fig. 4.2.

Combining Eqs. 4.2 and 4.11, we obtain the relation between the experimentally measured G_{th}

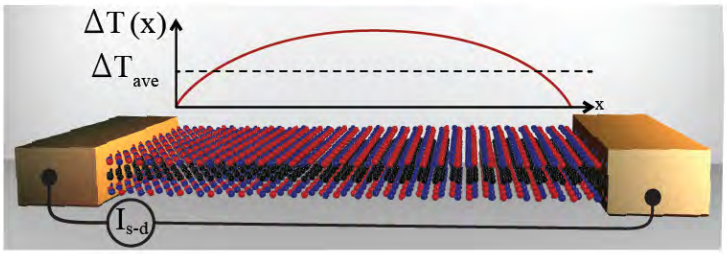

Figure 4.2: Cartoon illustrating the non-uniform temperature profile within the graphene-hBN stack during Joule heating in the diffusion-limited regime.

and the microscopic quantity of interest κ as:

$$G_{\text{th}} \equiv \frac{P_0}{\Delta T_{JN}} = \frac{12\,W}{L}\kappa \tag{4.13}$$

All the information about the heating profile is contained in the constant factor of 12. — i.e for a two-terminal rectangular geometry under Joule heating $\beta = 12$. If the electronic conductance follows the Wiedemann-Franz law, such that $\kappa = \mathcal{L}\sigma T$, then Eqn. 4.13 becomes

$$G_{\text{th}} = \frac{12W\mathcal{L}\sigma T_{\text{b}}}{L} = \frac{12\mathcal{L}T_{\text{b}}}{R} \tag{4.14}$$

where R is the directly measurable, two-terminal electrical resistance.

4.1.2 Phonon cooling only

The limit of electron-phonon dominated cooling can be modeled by phonons effectively removing an isotropic amount of heat per unit area; the balance between this and Joule heating leads

to a uniform temperature profile,

$$\Delta T(x) = T_0 = \Delta T_{JN} \tag{4.15}$$

The heat balance equation (Eqn. 4.2) then becomes

$$I^2 R = W L \, \Sigma_{e-ph} \delta T_{\mathrm{b}}^{\delta-1} \Delta T_{JN} \tag{4.16}$$

and thus the microscopic parameters governing electron-phonon coupling are related to the experimentally measured thermal conductance in the linear response regime by

$$G_{\mathrm{th}} = W L \, \Sigma_{e-ph} \delta T_{\mathrm{b}}^{\delta-1} \tag{4.17}$$

4.2 Wedge devices

Unlike in rectangular devices, where the Johnson noise temperature is simply the mean temperature, in more complicated geometries the effective temperature measured in a noise experiment must be calculated from the Joule heating temperature profile. An instructive example of a more complicated geometry which can also be solved analytically is a semicircular wedge as shown in fig. 4.3. The continuity equations for charge current in cylindrical coordinates yield

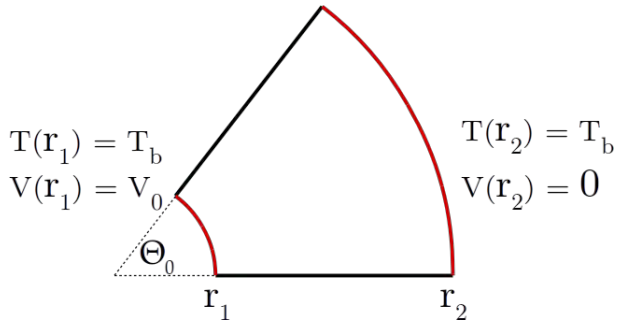

Figure 4.3: Sketch of a wedge shaped device and boundary conditions for Joule heating. Red boundaries represent contacts where temperature is fixed at T_b. A voltage V_0 is placed on the contact at $r = r_1$ while the second contact at $r = r_2$ is held at ground. Cylindrical symmetry leaves heat and charge currents independent of angle.

$$\mathrm{J}(r) = -\frac{V_0\,\sigma}{\ln(r_1/r_2)}\frac{1}{r}\hat{r} \tag{4.18}$$

and for heat current with a Joule heating source term

$$\frac{\mathrm{J}^2}{\sigma} = \nabla\cdot\dot{q} = \kappa\frac{\mathrm{d}^2T}{\mathrm{d}r^2} + \frac{\kappa}{r}\frac{\mathrm{d}T}{\mathrm{d}r} \tag{4.19}$$

Combining Eqns. 4.18 and 4.19 and solving using the thermal boundary conditions of fixed temperature at the contacts, the temperature profile is given by:

$$\Delta T(r) = \frac{V_0^2\,\sigma}{2\kappa\ln\left(r_1/r_2\right)^2}\ln\left(\frac{r}{r_1}\right)\ln\left(\frac{r}{r_2}\right) \tag{4.20}$$

The mean temperature and the Johnson noise temperature can be calculated by integrating Eqn. 4.20 yielding,

$$\begin{aligned}\langle \Delta T \rangle &= \int_{r_1}^{r_2} T(r)\, r\, \mathrm{d}r \Big/ \int_{r_1}^{r_2} r\, \mathrm{d}r \\ &= \frac{V_0^2\, \sigma}{4\, \kappa \ln(r_2/r_1)} \left[\frac{r_1^1 + r_2^2}{r_1^1 + r_2^2} - \ln(r_2/r_1) \right] \qquad (4.21) \\ \Delta T_{JN} &= \int_{r_1}^{r_2} \dot{q}(r) T(r)\, r\, \mathrm{d}r \Big/ \int_{r_1}^{r_2} \dot{q}(r)\, r\, \mathrm{d}r \\ &= \frac{V_0^2\, \sigma}{12\, \kappa} \qquad (4.22)\end{aligned}$$

The difference between the spatially averaged temperature and ΔT_{JN} illustrates the power of combining Joule heating with Johnson noise thermometry — the spatial distribution with which heat is injected into the system is the same as the spatial weighting function for Johnson noise measurements. Rewriting Eqn. 4.22 in terms of G_{th} assuming the Wiedemann-Franz law we arrive at the same form as Eqn. 4.14,

$$G_{\mathrm{th}} = \frac{12 \mathcal{L} T_{\mathrm{b}}}{R} \qquad (4.23)$$

All geometric dependence is contained in the experimentally measurable two-terminal resistance R and we find, similar to the rectangular geometry, $\beta = 12$.

4.3 Universality of β

Above we have derived two analytic examples where β was shown to be 12. In fact, it can be shown that $\beta = 12$ is universally true in the linear response regime regardless of the geometry of the device or the form of the conductivity tensors, $\hat{\sigma}$ and $\hat{\kappa}$, provided the following conditions are met:

1. The device has only two electrical terminals which serve as thermal heat sinks and sources of Joule heating current
2. Electron cool is provided only by Wiedemann-Franz diffusion
3. $\hat{\sigma}$ and $\hat{\kappa}$ are spatially uniform
4. The elastic mean free path of the charge carriers is shorter than all other relevant length scales in the system

The following derivation is adapted from a work done by Dr. Brian Skinner, MIT, altered for clarity and brevity:

Without loss of generality, we can imagine a unit voltage applied across an arbitrary two terminal device, so that the electric potential $\phi(r)$ has $\phi = 1$ at the source electrode and $\phi = 0$ at the drain. For a generic conductivity tensor $\hat{\sigma}$ (which may be affected by magnetic field) the electric current $\vec{J}(r)$ is

$$\vec{J}(r) = -\hat{\sigma}\vec{\nabla}\phi. \tag{4.24}$$

Thus, the continuity equation $\vec{\nabla} \cdot \vec{\mathrm{J}} = 0$ becomes

$$\vec{\nabla} \cdot \hat{\sigma} \vec{\nabla} \phi = 0 \tag{4.25}$$

This equation, together with the boundary conditions, defines the electric potential. The boundaries at non-contact edges are assumed to be reflecting, so that $(\vec{\nabla}\phi) \cdot \hat{n} = 0$, where $\hat{n}$ is a unit normal vector to the boundary.

The electron temperature $T(r)$, defined relative to the bath temperature T_{b}, obeys the heat diffusion equation

$$\mathcal{P}(r) = -\vec{\nabla} \cdot (\hat{\kappa} \vec{\nabla} T), \tag{4.26}$$

if there are no extraneous sources of heat dissipation, such as electron-phonon coupling, then the steady state condition will set $\mathcal{P}$ equal to the dissipated Joule heating power per unit area. The Joule power is given by $\vec{\mathrm{J}} \cdot \vec{E}$, or

$$\mathcal{P}(r) = (\hat{\sigma} \vec{\nabla} \phi) \cdot (\vec{\nabla} \phi) \tag{4.27}$$

If we assume the generalized Wiedemann-Franz relation in the linear response regime, $\hat{\kappa} = \hat{\sigma} \mathcal{L} T_{\mathrm{b}}$, we arrive at the following relation governing the temperature:

$$(\hat{\sigma} \vec{\nabla} \phi) \cdot (\vec{\nabla} \phi) = -\mathcal{L} T_{\mathrm{b}} \vec{\nabla} \cdot (\hat{\sigma} \vec{\nabla} T). \tag{4.28}$$

Together with the boundary conditions, this equation defines the temperature profile $T(r)$. We

assume that the contacts are good heat sinks, so that $T = 0$ at both contacts, and that no heat is lost at the boundary of the sample: $(\vec{\nabla}T) \cdot \hat{n} = 0$.

Eqn. 4.28 makes clear that there is a close relation between the temperature profile and the electric potential. It can be shown that Eqn. 4.28 and the boundary condictions are satisfied by the ansatz,

$$T(r) = \frac{1}{2\,\mathcal{L}\,T_\mathrm{b}}\phi(r)(1-\phi(r)). \tag{4.29}$$

From Eqn. 4.29 we can calculate the Johnson noise temperature via Eqn. 2.12:

$$\begin{aligned} \Delta T_{JN} &= \frac{\int \mathrm{d}^2 r \mathcal{P}(r)\, T(r)}{P_0} \\ &= \frac{R}{2\mathcal{L}T_\mathrm{b}} \int \mathrm{d}^2 r \phi(r)\,[1-\phi(r)] \left[\hat{\sigma}\vec{\nabla}\phi(r)\right] \cdot \left[\vec{\nabla}\phi(r)\right] \end{aligned} \tag{4.30}$$

Here we have used $P_0 = V^2/R = 1/R$ (assuming our voltage units). Combining Eqn. 4.29 and 4.30 we can write ΔT_{JN} is terms of only the temperature profile:

$$\begin{aligned} \Delta T_{JN} &= \mathcal{L}T_\mathrm{b}R \int \mathrm{d}^2 r T(r) \vec{\nabla} \cdot (\hat{\sigma}\vec{\nabla}T) \\ &= \mathcal{L}T_\mathrm{b}R \int \mathrm{d}^2 r (\vec{\nabla}T(r)) \cdot (\hat{\sigma}\vec{\nabla}T(r)). \end{aligned} \tag{4.31}$$

Eqn. 4.31 was found using integration by parts, and noting that either T or $\vec{\nabla}T$ vanishes at the boundaries of the sample.

The geometric factor β is defined by

$$\frac{1}{\beta} \equiv \frac{\Delta T_{JN}\, \mathcal{L}\, T_{\mathrm{b}}}{\dot{\mathrm{Q}}\, R}. \tag{4.32}$$

Plugging in Eqn. 4.30

$$\frac{1}{\beta} = \frac{1}{2\, P_0} \int \mathrm{d}^2 r \phi(1-\phi)(\hat{\sigma}\vec{\nabla}\phi) \cdot (\vec{\nabla}\phi). \tag{4.33}$$

On the other hand, inserting Eqn. 4.29 into eqn. 4.31 and rearranging gives

$$\begin{aligned}
\frac{1}{\beta} &= \frac{1}{4\, P_0} \int \mathrm{d}^2 r \left[\vec{\nabla}(\phi(1-\phi))\right] \cdot \left[\hat{\sigma}\vec{\nabla}(\phi(1-\phi))\right] \\
&= \frac{1}{4\, P_0} \int \mathrm{d}^2 r (1-2\phi)^2 (\vec{\nabla}\phi) \cdot (\hat{\sigma}\vec{\nabla}\phi) \\
&= \frac{1}{4\, P_0} \left[\int \mathrm{d}^2 r (\vec{\nabla}\phi) \cdot (\hat{\sigma}\vec{\nabla}\phi) - \int \mathrm{d}^2 r\, 4\phi(1-\phi)(\vec{\nabla}\phi) \cdot (\hat{\sigma}\vec{\nabla}\phi) \right].
\end{aligned} \tag{4.34}$$

The second term in Eqn. 4.34 is identical to the right hand side of Eqn. 4.33 multiplied by 2, and it is therefore equal to $2/\beta$. Thus:

$$\begin{aligned}
\frac{1}{\beta} &= \frac{1}{4\, P_0} \int \mathrm{d}^2 r (\vec{\nabla}\phi) \cdot (\hat{\sigma}\vec{\nabla}\phi) \\
&= \frac{1}{12\, P_0} \int \mathrm{d}^2 r (\vec{\nabla}\phi) \cdot (\hat{\sigma}\vec{\nabla}\phi) \\
&= \frac{1}{12\, P_0} \int \mathrm{d}^2 r\, \mathcal{P}(r)
\end{aligned} \tag{4.35}$$

The final step in Eqn. 4.35 comes from realizing the integrand is simply the Joule heating power

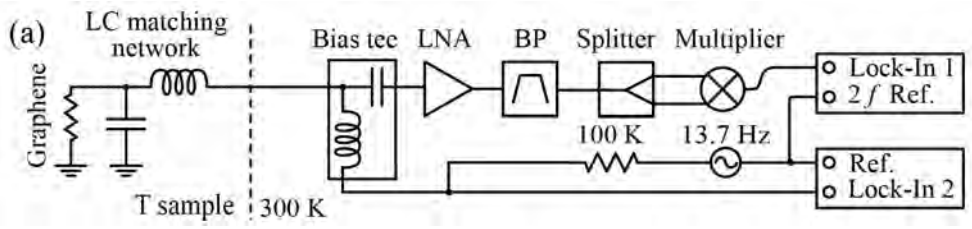

Figure 4.4: Simplified schematic of thermal conductance measurement setup. A low frequency Joule heating current is pass through the sample using a lock-in amplifier and the corresponding temperature is measured using Johnson noise thermometry. A bias tee is used to combine the DC and RF signals. The noise signal is measured as the second harmonic of the heating current as $\Delta T \sim I^2$

given in eqn. 4.27, and thus

$$\beta = 12 \tag{4.36}$$

4.4 Experimental setup

To sensitively measure ΔT_{JN}, the autocorrelation Johnson noise thermometry circuit described in chapter 2 can be modified to allow a DC current to Joule heat the sample. Fig. 4.4 shows a simplified schematic of a thermal conductance measurement setup. A low frequency ($f \sim 13\ Hz$) current is generated by a lock-in amplifier[†] at frequency $\omega = 2\pi \times f$ and passed through the sample[‡] using a bias tee. If the current is given by:

$$I(t) = I_0 \sin(\omega t) \tag{4.37}$$

[†]This lock-in is also used to measure the two-terminal resistance R

[‡]It is because of this need to pass a DC current through the matching network and into the sample that the LC tanks used are setup in a low-pass configuration

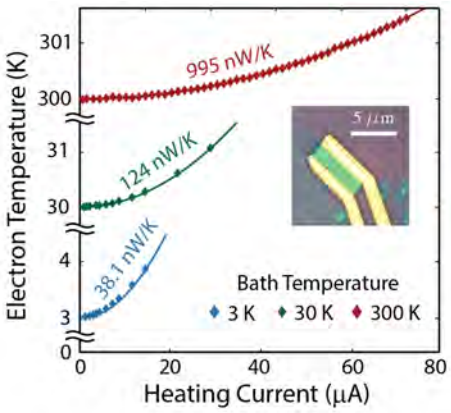

Figure 4.5: Electron temperature of a two-terminal graphene device (**inset**) as a function of a Joule heating current for three different bath temperatures. The temperatures follow an I^2 heating law with the curvature determined by the generalized thermal conductance $G_{\rm th}$ which increases with the bath temperature. Here electron temperature is defined as the Johnson noise temperature as discussed in section 4.1

the total heating power dissipated in the device is

$$P_0(t) = I_0^2 R \sin^2(\omega t) \tag{4.38}$$

and the corresponding temperature rise in Johnson noise temperature is

$$\begin{aligned} \Delta T_{JN}(t) &= \frac{I_0^2 R}{G_{\rm th}} \sin^2(\omega\, t) \\ &= \frac{I_0^2 R}{2\, G_{\rm th}} \left(1 - \cos(2\,\omega\, t)\right) \end{aligned} \tag{4.39}$$

The 2ω component of the corresponding noise signal is then measured by a second lock-in amplifier detecting the second harmonic of the Joule heating current (phase shifted by $\pi/2$) as shown in Fig. 4.4.

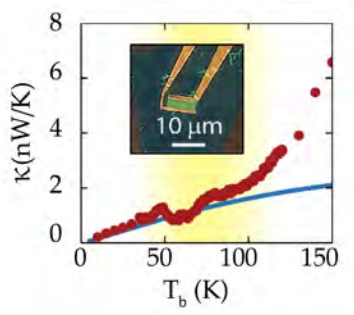

Figure 4.6: Thermal conductivity extracted from G_{th} measured using a circuit similar to that shown in Fig. 4.4 assuming $\beta = 12$. At low temperature κ can accurately be extracted from G_{th} and the measured thermal conductivity follows the Wiedemann-Franz law (solid blue line). At higher temperatures phonons spoil the assumptions needed for $\beta = 12$ and prevent the accurate measurement of κ

Fig. 4.5 shows how the electronic temperature of a mesoscopic device responds to a heating current. As expected in the linear response regime, the temperature rise follows an I^2 heating curve with curvature governed by the generalized thermal conductance. The thermal conductivity, κ, can be extracted in the low temperature regime using the factor $\beta = 12$ derived in section 4.1 — a example of which is shown in comparison to the Wiedemann-Franz law in Fig. 4.6. At low temperature the assumptions required to show $\beta = 12$ are met and the measured thermal conductivity follows the Wiedemann-Franz law. At high temperatures appreciable electron-phonon coupling creates an additional energy loss mechanism and κ can no longer be accurately extracted from G_{th}.

5

Thermal conductance in high density graphene

When the Fermi level of graphene is doped far from the Dirac point ($\mu \gg k_B T$), graphene has a well defined Fermi surface and the assumptions in Sommerfeld's derivation of the Lorenz ra-

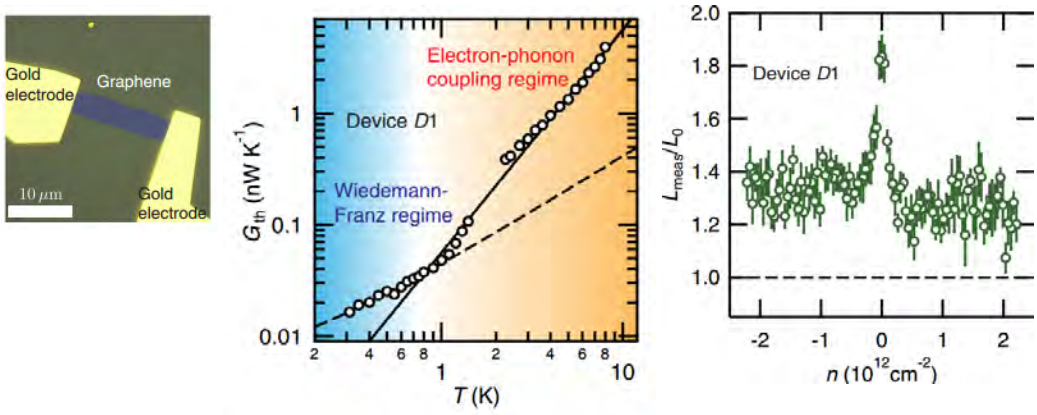

Figure 5.1: (**left**) Device image and (**center**) electronic thermal conductivity of graphene on SiO_2 measured by Fong et al. [41] using Johnson noise thermometry. Dashed line is a fit to the Wiedemann-Franz law. Below $1\ K$ the device shows WF behavior while at higher temperature the measured conduction is higher due to phonons coupling. The longer device used in this study resulted in phonons dominating conductance at a lower temperature. (**right**) The corresponding measured Lorenz ratio vs carrier density. Reprinted under the Creative Commons Attribution 3.0 License from Ref. [41].

tio hold. In 2013, Fong et al. [41] verified the Wiedemann-Franz for graphene on SiO_2 (Fig. 5.1) using Joule heating and Johnson noise thermometry. The device measured had a mobility of $\mu \gtrsim 5,000\ cm^2/Vs$ and a length which emphasized phonon scattering, resulting in the Wiedemann-Franz law (WFL) only being verifiable until $1\ K$. Nevertheless, a Lorenz ratio varying between $1 - 2\ \mathcal{L}_0$ was measured for various charge densities (Fig. 5.1) at low temperature. Above $1\ K$ the thermal conductance increased above the WFL due to electron-phonon scattering as described in section 3.2. A few months later, Yigen et al. [49] performed similar Joule heating experiments using resistive thermometry with higher quality suspended graphene ($\mu \gtrsim 35,000\ cm^2/Vs$). As shown in Fig.5.2, the shorter device geometry allowed them to measure the WFL to a much higher temperature of $\sim 150\ K$ finding experimental Lorenz ratios of about $0.5\ \mathcal{L}_0$.

In this chapter we present similar data on higher mobility samples encapsulated with hexagonal

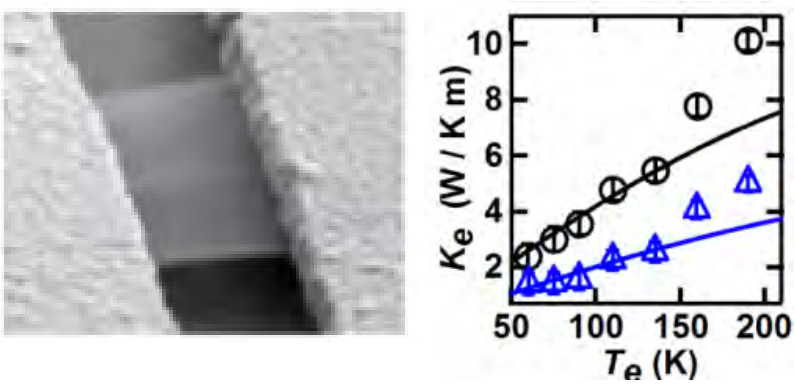

Figure 5.2: Electronic thermal conductivity of suspended graphene measured by Yigen et al. [49] using resistive thermometry. Two curves correspond to different carrier densities. Solid lines are fits to the Wiedemann-Franz law. Below $\sim 150\,K$ the device shown WF behavior while at higher temperature the measured conduction is higher due to phonons coupling. Device is $650\,nm$ long. Reprinted with permission from [49]. Copyright (2014) American Chemical Society.

boron nitride (hBN).

5.1 Device characteristics

Monolayer graphene is mechanically exfoliated, encapsulated in hexagonal boron nitride, and contacted along its 1-dimensional edge [50] to form a $(2\,\mu m \times 6\,\mu m)$ channel (Fig. 5.3). A typical two-terminal channel resistance R of this device varies between 150 and 800 Ω depending on the back gate voltage. The mobility, μ, of the device can be estimated by fitting the two-terminal resistance as a function of charge density n, as shown in Fig. 5.3, to find $\mu \approx 330,000\,cm^2/Vs$ at $3\,K$ and $\mu \approx 60,000\,cm^2/Vs$ at $300\,K$.

As maximal noise power is collected when the device is impedance matched to the measurement chain, an LC tank circuit is placed on chip to transform the graphene to 50 Ω (as disscussed in sec-

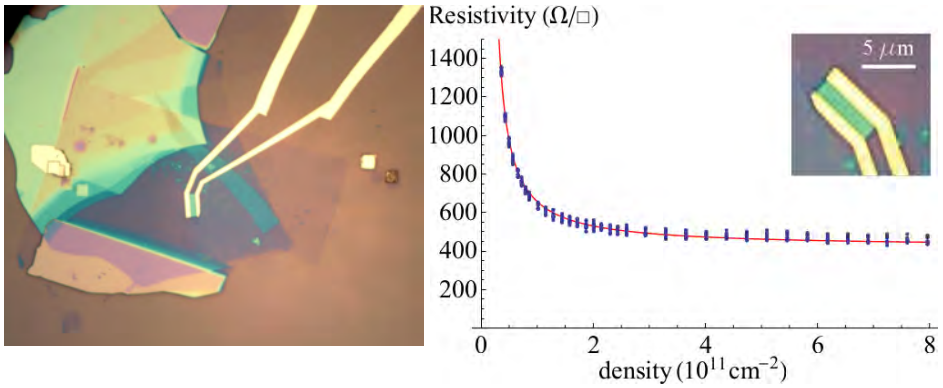

Figure 5.3: (**left**) Microscope image of the two-terminal graphene device $(2\,\mu m \times 6\,\mu m)$ used in thermal conduction studies presented in this chapter. (**right**) Estimated resistivity vs carrier density from two-terminal resistance. Solid red line is a fit used to estimate a carrier mobility of $\mu \approx 330,000\,cm^2/Vs$.

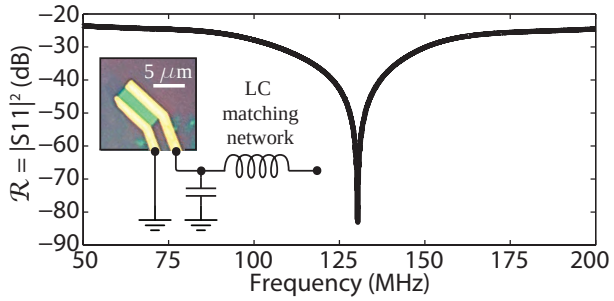

Figure 5.4: RF reflectance off the two-terminal graphene device presented in this chapter. The sample impedance is transformed using a single stage LC network (**inset**) resulting in a measurement bandwidth of $25\,MHz$ centered at $133\,MHz$. See section 2.6 for details on impedance matching.

tion 2.6 and Refs. [51] and [52]) within the measurement bandwidth. The matching network defines a bandwidth of $25\,MHz$ centered at $133\,MHz$, as shown in Fig. 5.4. The total noise power emitted into this bandwidth is amplified and measured via the circuit and procedure outlined in chapter 4 resulting in a measured output voltage (proportional to the total noise power) similar to that shown in Fig. 5.5

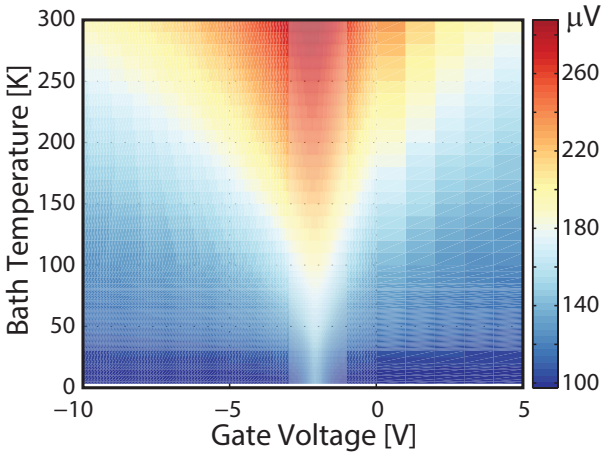

Figure 5.5: Measured DC voltage proportional to the total noise emitted from a graphene device as a function of bath temperature and back gate voltage using the circuit outline in chapter 2.

5.2 Thermal conductance

For the results shown here, the graphene device is measured away from the charge neutrality point with hole density $n \approx 5.7 \times 10^{10} cm^{-2}$, where R varies between 280 and 480 Ω from 3 to 300 K. The Johnson noise thermometer is calibrated to a given sample following the procedure outlined in chapter 2 and the thermal conductance, G_{th}, is extracted as discussed in chapter 4.

The thermal conductance of our device falls into two temperature regimes as shown in Fig. 5.6. For $T < 100\ K$, G_{th} linearly depends on temperature and is well described by the Wiedemann-Franz law. The dashed line in the left panel of Fig. 5.6 shows the theoretical Wiedemann-Franz conductance (G_{WF}) with an offset of $0.015\ \mu \mathrm{W}/K$. The fitted [41, 49] Lorenz number is $2.38 \times 10^{-8} \mathrm{W}\Omega K^{-2}$, 3% below the theoretical value. As the charge density is swept, the Lorenz ratio

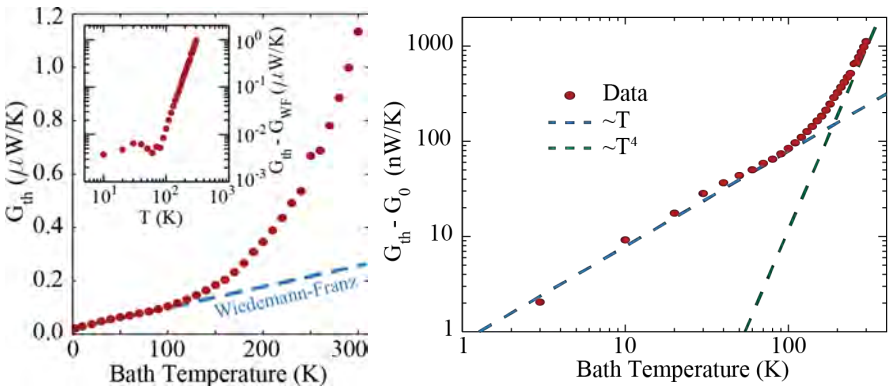

Figure 5.6: (**left**) Graphene thermal conductance from $3\ K$ to $300\ K$. Blue dashed line shows the theoretical Wiedemann-Franz conductance for our device geometry offset by a fitted constant. (**Inset**) shows the total conductance with G_{WF} subtracted. Above $T \sim 80\ K$, the conductance departs with a power law of 3.88 ± 0.02. (**right**) Same data with the fitted offset removed, shown on a log-log scale.

varies similar to that seen in ref [41], always remaining close to $\mathcal{L}_0$.

At higher temperature, the measured G_{th} is larger than Wiedemann-Franz conductance indicating a different energy transfer mechanism dominates above $100\ K$. Fig. 5.6(right) shows the same data on a log-log plot making clear the two different power laws in the different regimes. To extract the electron-phonon coupling constants, as outlined in section 3.2, the thermal conductance from electron diffusion must be accounted for. Fig. 5.6 inset plots G_{th} with G_{WF} subtracted. G_{th} departs from G_{WF} with a fitted power law of 3.88 ± 0.02 and an amplitude of $0.23 \pm 0.03\ f\mathrm{W}/K^{4.88}$. We note that the high power law $\delta \approx 4$ in our measured data is in sharp contrast to the sublinear temperature dependence of graphene's lattice conductivity for $T > 150\ K$ [48], suggesting that it is unlikely the energy transfer bottleneck and hence the lattice is well thermalized to the bath.

We compare the high temperature thermal conductance of our sample with the expected contri-

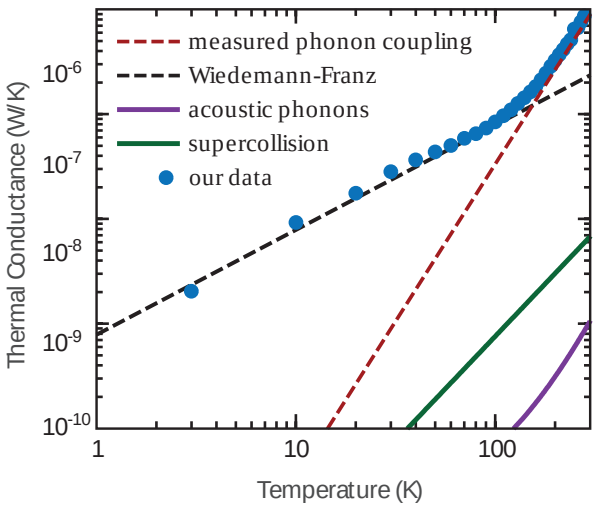

Figure 5.7: Thermal conductance of a graphene device compared to estimated contributions from acoustic phonons [31, 30] and the supercollision cooling mechanism [32, 33, 42, 43].

butions from acoustic phonons [31, 30] and the supercollision cooling mechanism [32, 33, 42, 43] given the measured mobility in Fig. 5.7; We estimate these contributions to be an order of magnitude too small to explain the observed G_{th}. From our experiment, we estimate that the thermal conductance per unit area at 300 K to be 9.5×10^4 W$/Km^2$. We find this to be comparable to theoretical calculations which suggest that optical phonons, both in the graphene lattice and the boron nitride substrate, may provide an energy relaxation channel substantially larger than acoustic phonons in this high temperature limit [34, 35, 30, 31, 36].

6

The Dirac fluid

While the term "Fermi liquid" is often used to describe the electron flow in a metal, the key feature of Fermi liquid theory is that the electron-electron interactions are renormalized away leaving something more analogous to a non-interacting gas than an ordinary fluid, like water. In strongly correlated systems, however, these interactions can dominate causing behavior ranging from Mott

insulators to high temperature superconductivity. In graphene near the charge neutrality point, a unique situation occurs where quasi-relativistic electrons are holes coexist and interact. In the limit of perfectly clean samples (and in the absence of phonon coupling), inter-particle scattering causes dissipation to electrical currents as electron and holes are driven in opposite directions by an electric field. This effect has been notoriously difficult to observe as scattering off of impurities and phonons can easily dominate inter-particle scattering in traditional graphene samples on SiO_2. Even in the case of clean samples, demonstrating that electron-electron scattering is dominate requires a measurement that can distinguish between the momentum conserving inter-particle collisions and the more traditional elastic scatting off impurities. One such measurement is to compare the response of a device under an electric field to its response under a thermal gradient; while an electric field drives electrons and holes in opposite directions, a thermal gradient drives them in the same direction, therefore inter-particle scattering causes dissipation to electric current but not to heat current (inset of Fig. 6.5c).

6.1 Temperature regimes

In general there are three primary scattering mechanism in graphene that can dominate transport: impurities, inter-particle, and phonon. At low temperature, charge impurities in graphene cause significant spatial variations in the local chemical potential resulting in what are known as electron-hole puddles. Shown in Fig. 6.1 are scanning tunneling microscope images of

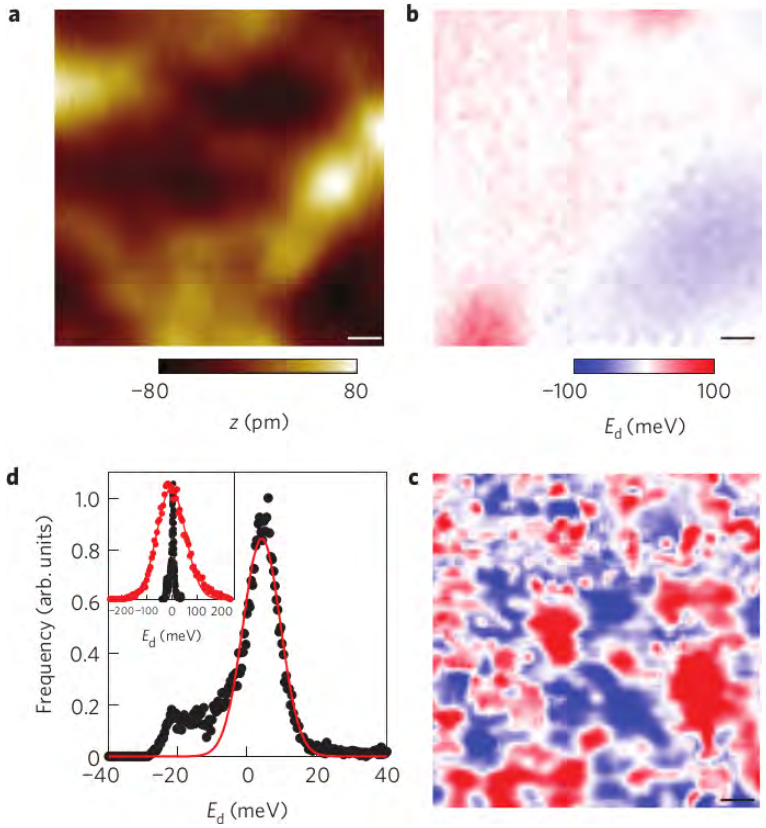

Figure 6.1: Spatial maps of the density of states of graphene on hBN and SiO_2. **a**, Topography of graphene on hBN. **b**, Tip voltage at the Dirac point as a function of position for graphene on hBN. **c**, Tip voltage at the Dirac point as a function of position for graphene on SiO_2. The color scale is the same for **b** and **c**. The scale bar in all images is 10 nm. **d** Histogram of the energies of the Dirac point from **b** as well as a Gaussian fit. The inset shows the same data but also includes the histogram for SiO_2 shown in red. Taken from ref [53], reprinted with permission from the Nature Publishing Group license number 4082110543400

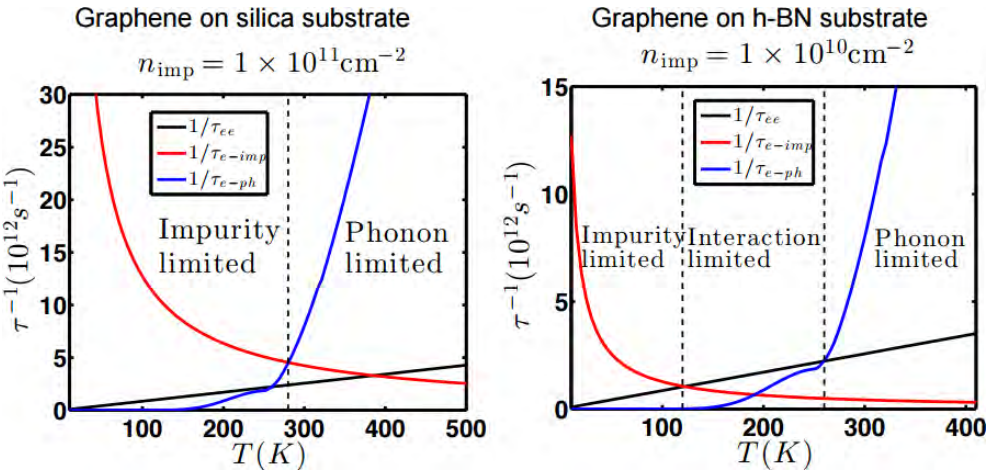

Figure 6.2: The interaction regime emerges in very clean samples. Taken from D. Y. H. Ho et al. (in preparation, 2017) with permission from S. Adam.

these puddles, taken for graphene on traditional SiO_2 substrates and on hexagonal boron nitride (hBN) [53]. On hBN these puddles can be of size $> 100\,nm$ — which is comparable to the electron-electron scattering length at moderate temperatures — and have a potential variation with standard deviation $\sim 5\,meV$. As temperature is increased, the effects of scattering off these charge impurities lessens and, at high enough temperatures, phonon scattering becomes significant, as described in section 3.2.

Whether there exists an intermediate temperature where inter-particle scattering becomes dominate depends on the disorder level. D. Ho et al. [54] quantitatively compares the scattering rates in graphene and finds that, for samples on hBN, a temperature window opens up where the electron-electron scattering time becomes the fastest in the system, Fig. 6.2.

Using clean samples on hBN and the thermal techniques presented in the previous chapters, we measured the electronic thermal conductivity of graphene at intermediate temperatures demonstrat-

ing that conduction is dominated by inter-particle scattering.

Below we present the original text of Ref. [55]. Reprinted with permission from J. Crossno, J.K. Shi, K. Wang, X. Liu, A. Harzheim, A. Lucas, S. Sachdev, P. Kim, T. Taniguchi, K. Watanabe, T.A. Ohki, and K.C. Fong. Science, 351(6277), pp.1058-1061 (2016). Copyright (2016) by AAAS.

6.2 Observation of the Dirac fluid and the breakdown of the Wiedemann-Franz law in graphene

Understanding the dynamics of many interacting particles is a formidable task in physics, complicated by many coupled degrees of freedom. For electronic transport in matter, strong interactions can lead to a breakdown of the Fermi liquid (FL) paradigm of coherent quasiparticles scattering off of impurities. In such situations, the complex microscopic dynamics can be coarse-grained to a hydrodynamic description of momentum, energy, and charge transport on long length and time scales [56]. Hydrodynamics has been successfully applied to a diverse array of interacting quantum systems, from high mobility electrons in conductors [57], to cold atoms [58] and quark-gluon plasmas [59]. As has been argued for strongly interacting massless Dirac fermions in graphene at the charge-neutrality point (CNP) [60, 61, 62, 63], hydrodynamic effects are expected to greatly modify transport coefficients as compared to their FL counterparts.

Many-body physics in graphene is interesting due to electron-hole symmetry and a linear dispersion relation at the CNP [64, 65]. In particular, the Fermi surface vanishes, leading to ineffective

screening [66] and the formation of a strongly-interacting quasi-relativistic electron-hole plasma, known as a Dirac fluid [67]. The Dirac fluid shares many features with quantum critical systems [68]: most importantly, the electron-electron scattering time is fast [69, 70, 71, 72], and well suited to a hydrodynamic description. A number of exotic properties have been predicted including nearly perfect (inviscid) flow [73] and a diverging thermal conductivity resulting in the breakdown of the Wiedemann-Franz law [74, 61].

Away from the CNP, graphene has a sharp Fermi surface and the standard Fermi liquid (FL) phenomenology holds. By tuning the chemical potential, we may measure thermal and electrical conductivity in both the Dirac fluid (DF) and the FL in the same sample. In a FL, the relaxation of heat and charge currents is closely related as they are carried by the same quasiparticles. The Wiedemann-Franz (WF) law [20] states that the electronic contribution to a metal's thermal conductivity κ_e is proportional to its electrical conductivity σ and temperature T, such that the Lorenz ratio $\mathcal{L}$ satisfies

$$\mathcal{L} \equiv \frac{\kappa_e}{\sigma T} = \frac{\pi^2}{3}\left(\frac{k_B}{e}\right)^2 \equiv \mathcal{L}_0 \tag{6.1}$$

where e is the electron charge, k_B is the Boltzmann constant, and $\mathcal{L}_0$ is the Sommerfeld value derived from FL theory. $\mathcal{L}_0$ depends only on fundamental constants, and not on specific details of the system such as carrier density or effective mass. As a robust prediction of FL theory, the WF law has been verified in numerous metals [20]. However, in recent years, an increasing number of non-trivial violations of the WF law have been reported in strongly interacting systems such as Luttinger liquids [75], metallic ferromagnets [76], heavy fermion metals [77], and underdoped cuprates [78],

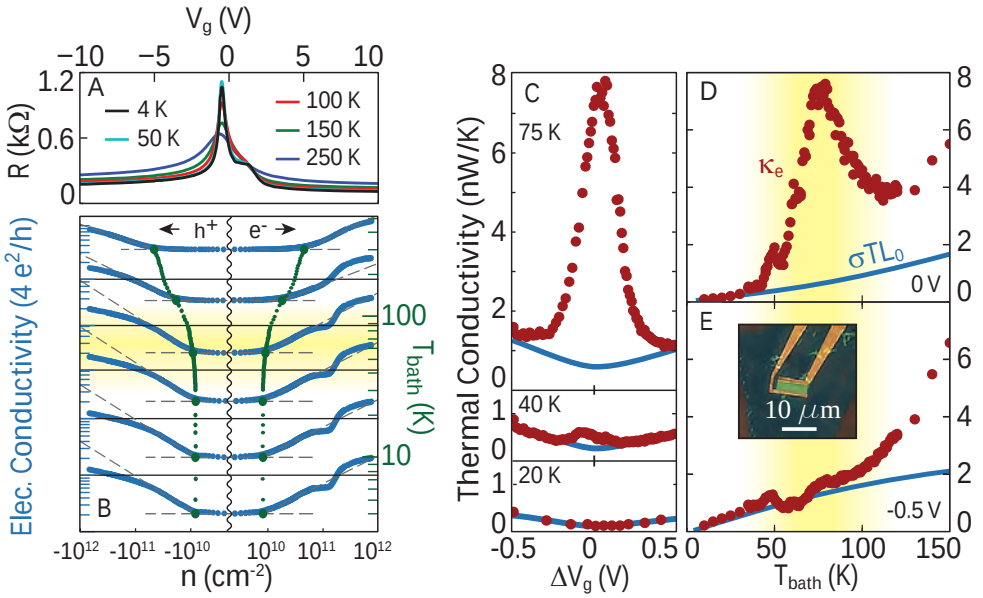

Figure 6.3: Temperature and density dependent electrical and thermal conductivity. (A) Resistance versus gate voltage at various temperatures. **(B)** Electrical conductivity (blue) as a function of the charge density set by the back gate for different bath temperatures. The residual carrier density at the neutrality point (green) is estimated by the intersection of the minimum conductivity with a linear fit to $\log(\sigma)$ away from neutrality (dashed grey lines). Curves have been offset vertically such that the minimum density (green) aligns with the temperature axis to the right. Solid black lines correspond to $4e^2/h$. At low temperature, the minimum density is limited by disorder (charge puddles). However, above $T_{\text{dis}} \sim 40$ K, a crossover marked in the half-tone background, thermal excitations begin to dominate and the sample enters the non-degenerate regime near the neutrality point. **(C-D)** Thermal conductivity (red points) as a function of (C) gate voltage and (D) bath temperature compared to the Wiedemann-Franz law, $\sigma T \mathcal{L}_0$ (blue lines). At low temperature and/or high doping ($|\mu| \gg k_{\text{B}}T$), we find the WF law to hold. This is a non-trivial check on the quality of our measurement. In the non-degenerate regime ($|\mu| < k_{\text{B}}T$) the thermal conductivity is enhanced and the WF law is violated. Above $T_{\text{el-ph}} \sim 80$ K, electron-phonon coupling becomes appreciable and begins to dominate thermal transport at all measured gate voltages. All data from this figure is taken from sample S2 (inset panel **E**).

all related to the emergence of non-Fermi liquid behavior.

The WF law is expected to be violated at the CNP in a DF due to the strong Coulomb interactions between thermally excited charge carriers. An electric field drives electrons and holes in opposite directions; collisions between them introduce a frictional dissipation, resulting in a finite conductivity even in the absence of disorder [79]. In contrast, a temperature gradient causes electrons and holes to move in the same direction inducing an energy current, which grows unimpeded by inter-particle collisions (Fig. 6.5c inset). The thermal conductivity is therefore limited only by the rate at which momentum is relaxed due to residual impurities.

Realization of the Dirac fluid in graphene requires that the thermal energy be larger than the local chemical potential $\mu(\mathrm{r})$, defined at position r: $k_{\mathrm{B}}T \gtrsim |\mu(\mathrm{r})|$. Impurities cause spatial variations in the local chemical potential, and even when the sample is globally neutral, it is locally doped to form electron-hole puddles with finite $\mu(\mathrm{r})$ [80, 81, 82, 53]. Formation of the DF is further complicated by phonon scattering at high temperature which can relax momentum by creating additional inelastic scattering channels. This high temperature limit occurs when the electron-phonon scattering rate becomes comparable to the electron-electron scattering rate. These two temperatures set the experimental window in which the DF and the breakdown of the WF law can be observed.

To minimize disorder, the monolayer graphene samples used in this report are encapsulated in hexagonal boron nitride (hBN) [83]. All devices used in this study are two-terminal to keep a well-defined temperature profile [51] with contacts fabricated using the one-dimensional edge technique [50] in order to minimize contact resistance. We employ a back gate voltage V_{g} applied to the silicon substrate to tune the charge carrier density $n = n_{\mathrm{e}} - n_{\mathrm{h}}$, where n_{e} and n_{h} are the electron and

hole density, respectively (see section 6.5). All measurements are performed in a cryostat controlling the temperature T_{bath}. Fig. 6.3a shows the resistance R versus V_g measured at various fixed temperatures for a representative device (see section 6.5). From this, we estimate the electrical conductivity σ (Fig. 6.3b) using the known sample dimensions. At the CNP, the residual charge carrier density n_{min} can be estimated by extrapolating a linear fit of $\log(\sigma)$ as a function of $\log(n)$ out to the minimum conductivity [84]. At the lowest temperatures we find n_{min} saturates to $\sim 8 \times 10^9\ cm^{-2}$. We note that the extraction of n_{min} by this method overestimates the charge puddle energy, consistent with previous reports [83]. Above the disorder energy scale $T_{\text{dis}} \sim 40\ K$, n_{min} increases as T_{bath} is raised, suggesting thermal excitations begin to dominate and the sample enters the non-degenerate regime near the CNP.

The electronic thermal conductivity is measured using high sensitivity Johnson noise thermometry (JNT) [51, 10]. We apply a small bias current through the sample that injects a joule heating power P directly into the electronic system, inducing a small temperature difference $\Delta T \equiv T_e - T_{\text{bath}}$ between the graphene electrons and the bath. The electron temperature T_e is monitored independent of the lattice temperature through the Johnson noise power emitted at $100\ MHz$ with a $20\ MHz$ bandwidth defined by an LC matching network. We designed our JNT to be operated over a wide temperature range $3 - 300\ K$ [10]. With a precision of $\sim 10\ mK$, we measure small deviations of T_e from T_{bath}, i.e. $\Delta T \ll T_{\text{bath}}$. In this limit, the temperature of the graphene lattice is well thermalized to the bath [51] and our JNT setup allows us to sensitively measure the electronic cooling pathways in graphene. At low enough temperatures, electron and lattice interactions are weak [10, 41], and most of the Joule heat generated in graphene escapes via direct diffusion to the

contacts (SM). As temperature increases, electron-phonon scattering becomes appreciable and thermal transport becomes limited by the electron-phonon coupling strength [41, 85, 22]. The onset temperature of appreciable electron-phonon scattering, $T_{\mathrm{el-ph}}$, depends on the sample disorder and device geometry: $T_{\mathrm{el-ph}} \sim 80\ K$ [41, 10, 49, 86] for our samples. Below this temperature, the electronic contribution of the thermal conductivity can be obtained from P and ΔT using the device dimensions (SM).

Fig. 6.3c plots $\kappa_e(V_g)$ alongside the simultaneously measured $\sigma(V_g)$ at various fixed bath temperatures. Here, for a direct quantitative comparison based on the WF law, we plot the scaled electrical conductivity as $\sigma T\mathcal{L}_0$ in the same units as κ_e. At low temperatures, $T < T_{\mathrm{dis}} \sim 40\ K$, where the puddle induced density fluctuations dominates, we find $\kappa_e \approx \sigma T\mathcal{L}_0$, monotonically increasing as a function of carrier density with a minimum at the neutrality point, confirming the WF law in the disordered regime. As T increases ($T > T_{\mathrm{dis}}$), however, the measured κ_e begins to deviate from the FL theory. We note that this violation of the WF law only appears close to the CNP, with the measured thermal conductivity maximized at $n = 0$ (Fig. 6.3d). The deviation is the largest at $75\ K$, where κ_e is over an order of magnitude larger than the value expected for a FL. This non-FL behavior quickly disappears as $|n|$ increases; κ_e returns to the FL value and restores the WF law. In fact, away from the CNP, the WF law holds for a wide temperature range, consistent with previous reports [10, 49, 41]. For this FL regime, we verify the WF law up to $T_{\mathrm{el-ph}} \sim 80$ K. Finally, in the high temperature regime $T > T_{\mathrm{el-ph}}$, the additional electron-phonon cooling pathway causes the measured thermal conductivity to be larger than κ_e. We find that near the CNP κ_e tends to decrease just before $T_{\mathrm{el-ph}}$, restricting the maximal observable violation of the WF law.

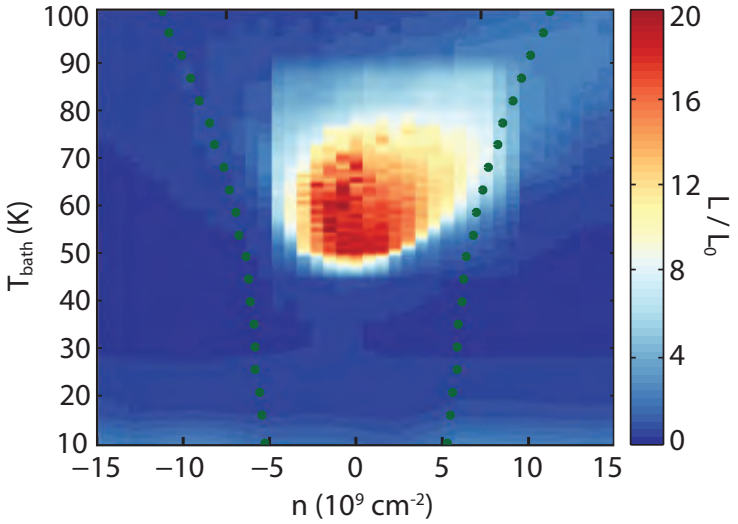

Figure 6.4: Breakdown of the Wiedemann-Franz law in the Dirac fluid regime. The Lorenz ratio is shown as a function of the charge carrier density and bath temperature. Near the CNP and for temperatures above the disorder (charge puddle) regime but below the onset of electron-phonon coupling, the Lorenz ratio is measured to be an order of magnitude greater than the Fermi liquid value of 1 (blue). The WF law is observed to hold outside of the Dirac fluid regime. All data from this figure is taken from sample S1.

Our observation of the breakdown of the WF law in graphene is consistent with the emergence of the DF. Fig. 6.4 shows the full density and temperature dependence of the experimentally measured Lorenz ratio in order to highlight the presence of the DF. The blue colored region denotes $\mathcal{L} \sim \mathcal{L}_0$, suggesting the carriers in graphene exhibit FL behavior. The WF law is violated in the DF (yellow-red) with a peak Lorenz ratio 22 times larger than $\mathcal{L}_0$. The green dotted line shows the corresponding $n_{\text{min}}(T)$ for this sample; the DF is found within this regime, indicating the coexistence of thermally populated electrons and holes. We find that disorder and phonon scattering bound the temperature range of the Dirac fluid, $T_{\text{dis}} < T < T_{\text{el-ph}}$.

We investigate the effect of impurities on hydrodynamic transport by comparing the results obtained from samples with varying disorder. Fig. 6.5a shows n_{min} as a function of temperature for three samples used in this study. $n_{\text{min}}(T = 0)$ is estimated as 5, 8, and $10 \times 10^9\ cm^{-2}$ in samples S1, S2, and S3, respectively. All devices show qualitatively similar Dirac fluid behavior; the largest value of $\mathcal{L}/\mathcal{L}_0$ measured in the Dirac fluid regime is 22, 12 and 3 in samples S1, S2, and S3, respectively (Fig. 6.5b). For a direct comparison, we show $\mathcal{L}(n)$ for all three samples at the same temperature ($60\ K$) in Fig. 6.5c. We find that cleaner samples not only have a more pronounced peak but also a narrower density dependence, as predicted [74, 61].

More quantitative analysis of $\mathcal{L}(n)$ in our experiment can be done by employing a quasi-relativistic hydrodynamic theory of the DF incorporating the effects of weak impurity scattering [87, 74, 61]

$$\mathcal{L} = \frac{\mathcal{L}_{\text{DF}}}{(1 + (n/n_0)^2)^2} \tag{6.2}$$

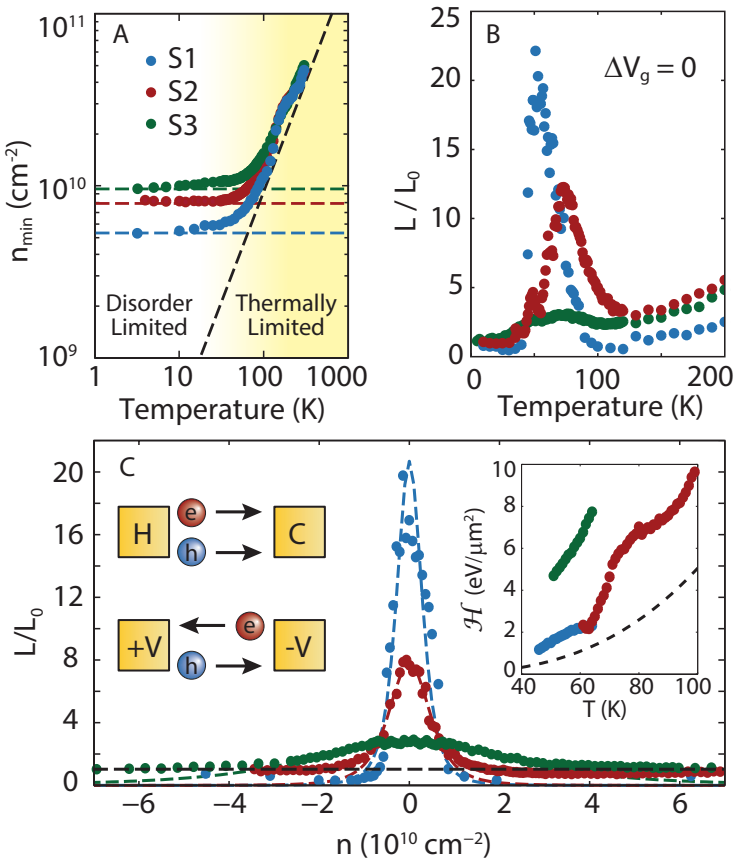

Figure 6.5: Disorder in the Dirac fluid. (A) Minimum carrier density as a function of temperature for all three samples. At low temperature each sample is limited by disorder. At high temperature all samples become limited by thermal excitations. Dashed lines are a guide to the eye. **(B)** The Lorenz ratio of all three samples as a function of bath temperature. The largest WF violation is seen in the cleanest sample. **(C)** The gate dependence of the Lorenz ratio is well fit to hydrodynamic theory of Ref. [74, 61]. Fits of all three samples are shown at $60\ K$. All samples return to the Fermi liquid value (black dashed line) at high density. Inset shows the fitted enthalpy density as a function of temperature and the theoretical value in clean graphene (black dashed line). Schematic inset illustrates the difference between heat and charge current in the neutral Dirac plasma.

where

$$\mathcal{L}_{\mathrm{DF}} = \frac{\mathcal{H} v_{\mathrm{F}} l_{\mathrm{m}}}{T^2 \sigma_{\mathrm{min}}} \quad \text{and} \quad n_0^2 = \frac{\mathcal{H} \sigma_{\mathrm{min}}}{e^2 v_{\mathrm{F}} l_{\mathrm{m}}}. \tag{6.3}$$

Here v_{F} is the Fermi velocity in graphene, σ_{min} is the electrical conductivity at the CNP, $\mathcal{H}$ is the fluid enthalpy density, and l_m is the momentum relaxation length from impurities. Two parameters in Eqn. 6.2 are undetermined for any given sample: l_m and $\mathcal{H}$. For simplicity, we assume we are well within the DF limit where l_m and $\mathcal{H}$ are approximately independent of n. We fit the experimentally measured $\mathcal{L}(n)$ to Eqn. 6.2 for all temperatures and densities in the Dirac fluid regime to obtain l_{m} and $\mathcal{H}$ for each sample. Fig. 6.5C shows three representative fits to Eqn. 6.2 taken at $60\ K$. l_{m} is estimated to be 1.5, 0.6, and $0.034\ \mu m$ for samples S1, S2, and S3, respectively. For the system to be well described by hydrodynamics, l_{m} should be long compared to the electron-electron scattering length of $\sim\ 0.1\ \mu$m expected for the Dirac fluid at $60\ K$ [73]. This is consistent with the pronounced signatures of hydrodynamics in S1 and S2, but not in S3, where only a glimpse of the DF appears in this more disordered sample. Our analysis also allows us to estimate the thermodynamic quantity $\mathcal{H}(T)$ for the DF. The Fig. 6.5c inset shows the fitted enthalpy density as a function of temperature compared to that expected in clean graphene (dashed line) [73], excluding renormalization of the Fermi velocity. In the cleanest sample $\mathcal{H}$ varies from $1.1 - 2.3 eV/\mu m^2$ for $T_{\mathrm{dis}} < T < T_{\mathrm{el-ph}}$. This enthalpy density corresponds to $\sim 20\ meV$ or $\sim 4 k_{\mathrm{B}} T$ per charge carrier — about a factor of 2 larger than the model calculation without disorder [73].

To fully incorporate the effects of disorder, a hydrodynamic theory treating inhomogeneity non-perturbatively is necessary [88, 89]. The enthalpy densities reported here are larger than the the-

oretical estimation obtained for disorder free graphene, consistent with the picture that chemical potential fluctuations prevent the sample from reaching the Dirac point. While we find thermal conductivity well described by Ref. [74, 61], electrical conductivity increases slower than expected away from the CNP, a result consistent with hydrodynamic transport in a viscous fluid with charge puddles [89].

In a hydrodynamic system, the ratio of shear viscosity η to entropy density s is an indicator of the strength of the interactions between constituent particles. It is suggested that the DF can behave as a nearly perfect fluid [73]: η/s approaches a conjecture by Kovtun-Son-Starinets: $(\eta/s)/(\hbar/k_B) \gtrsim 1/4\pi$ for a strongly interacting system [90]. A non-perturbative hydrodynamic framework can be employed to estimate η, as we discuss elsewhere [89]. A direct measurement of η is of great interest.

We have experimentally discovered the breakdown of the WF law and provided evidence for the hydrodynamic behavior of the Dirac fermions in graphene. This provides an experimentally realizable Dirac fluid and opens the way for future studies of strongly interacting relativistic many-body systems. Beyond a diverging thermal conductivity and an ultra-low viscosity, other peculiar phenomena are expected to arise in this plasma. The massless nature of the Dirac fermions is expected to result in a large kinematic viscosity, despite a small shear viscosity η. Observable hydrodynamic effects have also been predicted to extend into the FL regime [91]. The study of magnetotransport in the DF will lead to further tests of hydrodynamics [74, 87].

6.3 Sample Fabrication

Single layer graphene is encapsulated in hexagonal boron nitride on an n-doped silicon wafer with 285 nm SiO_2 [50] and is subsequently annealed in vacuum for 15 minutes at 350 $^\circ C$. It is then etched using reactive-ion-etching (RIE) to define the width of the device. A second etch mask is then lithographically defined to overlap with the sample edge, leaving the rest of the sample rectangular shaped with the desired aspect ratio. After the RIE is performed, the same etch mask is used as the metal deposition mask, upon which Cr/Pd/Au (1.5 nm / 5 nm / 200 nm) is deposited. The resulting Ohmic contacts show low contact resistances and small PN junction effects due to their minimum overlap with device edge.

6.4 Optimizing samples for high frequency thermal conductivity measurements

To measure the electronic thermal conductivity κ_e of graphene using high frequency Johnson noise the sample design should be made with three additional considerations: stray chip capacitance, resistance of the lead wires, and sample dimensions that enhance electron diffusion cooling over phonon coupling.

Johnson noise thermometry (JNT) relies on measuring the total noise power emitted in a speci-

fied frequency band and relating that to the electronic temperature on the device; to maximize the sensitivity, high frequency and wide bandwidth measurements should be made [10]. In the temperature range discussed here, the upper frequency limit for JNT is typically set by the amount of stray capacitance from the graphene, lead wires, and contact pads to the Si back gate. This is minimized by using short, narrow lead wires and small ($50\ \mu m \times 50\ \mu m$) bonding pads resulting in an estimated $4\ pF$ stray capacitance.

The amount of Johnson noise emitted between any two terminals is proportional to the mean electronic temperature between them where each point in space is weighted by its local resistance. Therefore, to maximize the signal coming from the graphene, contact resistance should be kept at a minimum. To compensate for the narrow lead wires, we deposit a thicker layer ($200\ nm$) of gold resulting in an estimated total contact resistance of $< 80\ \Omega$.

Lastly, to effectively extract κ_e from the total electronic thermal conductance G_{th} we want to enhance the electron diffusion cooling pathway with respect to the electron-phonon cooling pathway (see section 4.1 for details). This can be accomplished by keeping the length of the sample short as the total power coupled into the lattice scales as the area of the device while diffusion cooling scales as $1/R$. In addition, the device should be made wide to minimize the effects of disordered edges. We find these high aspect ratio samples ($\sim\ 3\ :\ 1$) are ideal for our measurements and serve the additional purpose of lowering the total sample resistance allowing us to impedance match over a wider bandwidth.

	S1	S2	S3
length (μm)	3	3	4
width (μm)	9	9	10.5
mobility ($10^5\ cm^2/Vs$)	3	2.5	0.8
n_{min} ($10^9\ cm^{-2}$)	5	8	10

Table 6.1: Basic properties of our three samples.

6.5 Device Characterization

In this study we measure three graphene devices encapsulated in hexagonal boron nitride (hBN), whose basic properties are detailed in Table 6.1. All devices are two-terminal with mobility estimated as

$$\mu \approx \frac{L}{neRW}, \tag{6.4}$$

where L and W are the sample length and width respectively, e is the electron charge, and n is the charge carrier density. The gate capacitance per unit area $C_{\text{g}} \approx 0.11$ fF/μm^2 is estimated considering the 285 nm SiO_2 and $\sim 20\ nm$ hBN dielectrics. From this we estimate the charge density

$$n = \frac{C_{\text{g}}(V_{\text{g}} - V_{\text{d}})}{e} \tag{6.5}$$

where V_{d} is the gate voltage corresponding to the charge neutrality point (CNP) estimated by the location of the maximum of the curve $R(V_{\text{g}})$. Fig. 6.6 shows the resistance of all samples as a function of gate voltage.

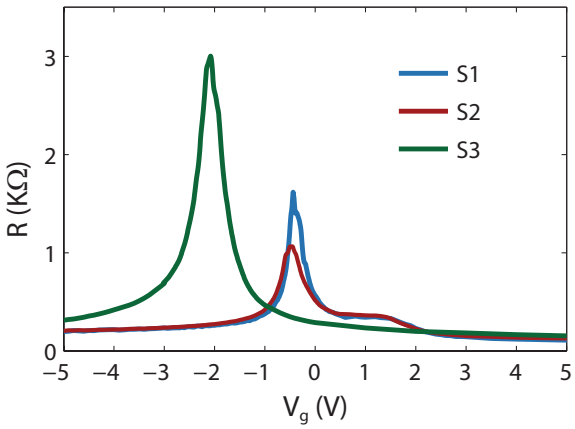

Figure 6.6: 2-terminal resistance R vs. back gate voltage for the 3 samples used in this report.

6.6 Bipolar Diffusion

The bipolar diffusion effect occurs when different charge carriers of opposite sign move in the same direction under an applied temperature gradient. The thermal conductivity κ, in the absence of net electric current flow, is given in Ref. [92]:

$$\kappa \equiv \left(\bar{\kappa}_e - \frac{T\alpha_e^2}{\sigma_e}\right) + \left(\bar{\kappa}_h - \frac{T\alpha_h^2}{\sigma_h}\right) + \frac{T\sigma_e\sigma_h}{\sigma_e + \sigma_h}\left(\frac{\alpha_e}{\sigma_e} - \frac{\alpha_h}{\sigma_h}\right)^2 \tag{6.6}$$

The first two terms in the above equations are the thermal conductivity of electrons and holes respectively. The third term is the bipolar diffusion term, and accounts for the possibility of electrons and holes flowing in the same direction.

Bipolar diffusion has been used to explain the thermal conductivity of narrow gap semiconductors, such as bismuth telluride, when the chemical potential is close to the midgap. Estimates of the

Lorenz ratio in bismuth telluride have been reported as high as 7.2 $\mathcal{L}_0$ in Ref. [93]. In graphene, the two types of charge carriers correspond to above/below the Dirac point. To use the formula (6.6) requires the assumption that interactions between electrons and holes are negligible. If this is the case, it is reasonable to employ kinetic theory to estimate $\sigma_{e,h}$, $\alpha_{e,h}$ and $\bar{\kappa}_{e,h}$. This was shown in Ref. [94] and we state the formalism here for completeness.

Employing the ultrarelativistic band structure of graphene near the CNP, the transport coefficients are given by:

$$\sigma_e = \int \frac{d^2k}{2\pi^2} \tau_e(k) v_F^2 \mathcal{F}\left(\frac{\hbar v_F k \pm \mu}{k_B T}\right), \tag{6.7a}$$

$$\alpha_e = \pm \int \frac{d^2k}{2\pi^2} \tau_e(k) (\hbar v_F k \pm \mu) v_F^2 \mathcal{F}\left(\frac{\hbar v_F k \pm \mu}{k_B T}\right), \tag{6.7b}$$

$$\bar{\kappa}_e = \int \frac{d^2k}{2\pi^2} \tau_e(k) (\hbar v_F k \pm \mu)^2 v_F^2 \mathcal{F}\left(\frac{\hbar v_F k \pm \mu}{k_B T}\right), \tag{6.7c}$$

where $\tau_{e,h}$ are suitably defined energy relaxation times for electrons and holes, we use a $\pm$ sign for electrons/holes, and

$$\mathcal{F}(x) \equiv \frac{1}{k_B T} \frac{e^x}{(1+e^x)^2}. \tag{6.8}$$

Given a choice of τ, it is straightforward to numerically integrate these equations. This was done in Ref. [94] for some choices of τ; we have checked additional choices. We compare the result of this two-band formalism at the CNP, to the same data for S1 used in Fig. 6.5. We can rule out the canonical bipolar diffusion (BD) explanation of our data for the following reasons:

1. The BD theory predicts that $\mathcal{L}/\mathcal{L}_{WF}$ is independent of temperature at the CNP in a clean sample. Adding disorder only adds a very weak temperature dependence [94]. This is in

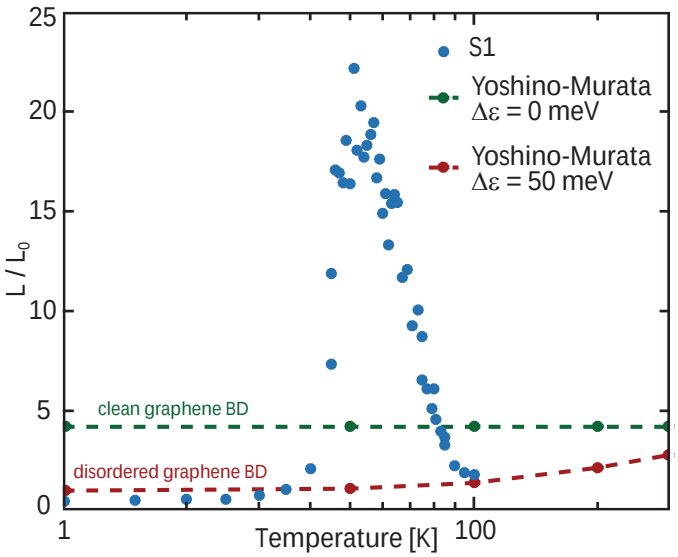

Figure 6.7: Comparison of the Lorenz ratio in graphene between bipolar diffusion theory [94] and our experimental data. The sharp temperature dependence of $\mathcal{L}$ is inconsistent with bipolar diffusion (see green dashed lines). This sharp behavior is predicted in hydrodynamics [89].

stark contrast to our data – see Figure 6.7. Hydrodynamic models do predict a sharp temperature dependence in $\mathcal{L}$ [89].

2. Simple models of BD in the presence of charge puddles with local chemical potential fluctuations of 50 meV or higher predict factor of 2 violations of the WF law [94], and a weak dependence of $\mathcal{L}$ on disorder, compared to hydrodynamics. In contrast we see a sharp dependence on disorder, comparing our three samples (Figure6.5). In samples where chemical potential fluctuations are comparable to $50\ meV$, the WF law is obeyed to within 40% [51].

3. Working under the theory of [95], $\tau(\mathrm{k}) \sim |\mathrm{k}|$, and hence the maximal Lorenz ratio $\mathcal{L}/\mathcal{L}_{\mathrm{WF}} \approx 4$ [94] – well below to our experimental observation of $\mathcal{L}/\mathcal{L}_{\mathrm{WF}} \approx 22$.

4. The BD theory of [94] predicts $\mathcal{L}/\mathcal{L}_{\mathrm{WF}} \gtrsim 0.8$ under all conditions. Hydrodynamics predicts that this ratio can become arbitrarily small in a clean sample, and we have indeed observed $\mathcal{L}/\mathcal{L}_{\mathrm{WF}} \sim 1/3$ at finite density in the DF in sample S1, only consistent with hydrodynamics.

Turn a switch and the light goes on. The layman's perception is that this is like opening a tap so that the water starts running. But this analogy is misleading.

Jan Zaanen

7

Hydrodynamic framework

In exotic materials, as electron-electron interactions begin to dominate over electron-impurity and electron-phonon scattering, new theoretical tools are needed to effectively model heat and charge transport. One such method, described in detail below, is to abandon the idea of quasiparticles altogether and instead rely on tracking macroscopically conserved quantities such as energy,

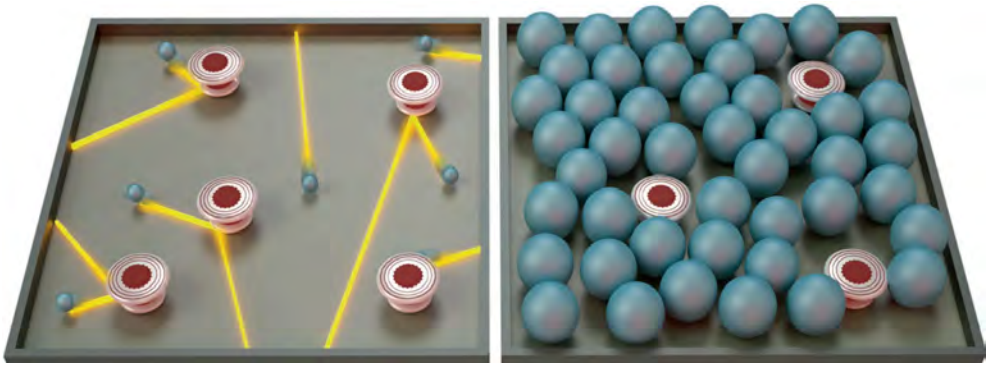

Figure 7.1: Distinguishing different flow regimes. (**Left**) In conventional metals, the flow of electrical current is due to electrons (balls) moving independently as a consequence of quantum physics while scattering against crystal imperfections (bumpers). (**Right**) In normal fluids such as water, the molecules collide with each other, equilibrating in a macroscopic fluid that is described by the theory of hydrodynamics. Electrons in particular solids that form strongly interacting quantum systems are also found to exhibit hydrodynamic transport properties (ref. [55, 96, 97]). Taken from ref. [98], reprinted with permission from AAAS license number 4082140628269

momentum, and charge (hydrodynamics). The difficulty with this technique is the inclusion of momentum relaxing scattering events, such as those due to impurities. It is possible to include these effects to first order by modeling the hydrodynamic equations in the presence of a non-uniform (but slowly varying) potential similar that shown [53] to exist in graphene. While this method has been applied with much success to describe the Dirac fluid, it is worth noting that, for the devices described in chapter 6, the electron-electron scattering rate is of the same order as other relevant scatting rates in the system; as such, a Boltzmann approach with the inclusion of an inter-particle scattering time is feasible [54] (Fig. 7.2 illustrates the regimes applicable to the two frameworks).

Below we present the original text of [89]. Reprinted with permission from A. Lucas, J. Crossno, K. C. Fong, P. Kim and S. Sachdev, "Hydrodynamic transport in quantum critical fluids and in the Dirac fluid in graphene", Physical Review B93 075426 (2016). Copyright (2016) by the American Physical Society

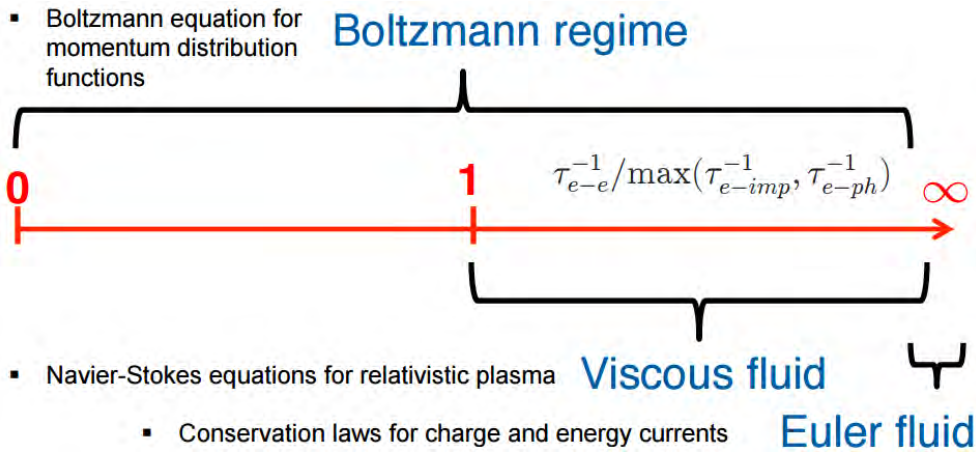

Figure 7.2: Illustration of a few common theoretical frameworks used to model electron flow in solids and their capabilities to models systems with various electron-electron interaction strengths. Taken from ref. [54] adapted from ref. [99] with permission from S. Adam

7.1 Transport in inhomogeneous quantum critical fluids and in the Dirac fluid in graphene

Over a half century ago, the theory of electronic transport in "standard" metals such as iron and copper was developed. The key pillar of this approach is the validity of Fermi liquid theory, which states that the interacting electrons in solids form nearly free-streaming quasiparticles [100]. At finite temperature, these quasiparticles form a weakly interacting quantum gas which is well described by quantum kinetic theory. The transport properties of these quantum gases are by now very well understood. A particularly important property of Fermi liquids is the Wiedemann-Franz

law, which states that[†]

$$\mathcal{L} \equiv \frac{\kappa}{\sigma T} = \frac{\pi^2}{3}\frac{k_B^2}{e^2} \equiv \mathcal{L}_{\text{WF}}. \tag{7.1}$$

Here κ is the electronic contribution to thermal conductivity, σ is the electrical conductivity, T is the temperature, and $\mathcal{L}$ is the Lorenz ratio. Implicit in the above equation is that the dominant interactions are between impurities or phonons and quasiparticles, and in most metals this is true: the interaction time between quasiparticles is typically 10^4 times longer than the interaction times between quasiparticles and impurities or phonons [20].

Also over a half century ago, a study of the consequences of hydrodynamic behavior on correlation functions and transport in interacting quantum systems was initiated [56]. Hydrodynamics is a framework for understanding the collective motion of the quasiparticles in a solid, or any other interacting quantum or classical system, so long as the microscopic degrees of freedom reach thermal equilibrium locally. In a solid, this interaction time must be the fastest time scale in the problem to see hydrodynamic behavior, but since quasiparticles in a Fermi liquid interact with each other only very weakly, observing hydrodynamics in electron fluids is notoriously hard. Even in the purest metals where hydrodynamic behavior can be observed, such as in GaAs [57, 101, 102], the resulting fluid is often a Fermi liquid. The resulting dynamics is the fluid dynamics of (quantum) gases. More recent theoretical work on hydrodynamics in Fermi liquids includes [103, 104, 105, 106, 107, 108], and recent experimental work includes [96, 97].

Fermi liquid theory is known to fail in a variety of experimentally realized metals in two or more

[†]Below we have assumed that the charge of the quasiparticles is $\pm e$, with e the charge of the electron – this is essentially always the case.

spatial dimensions – most famous among these is the strange metal phase of the cuprate superconductors [109, 110, 68] which does not have quasiparticle excitations. A slightly more theoretically controlled and better understood example of a state of quantum matter without quasiparticles is the quasi-relativistic Dirac fluid in the semimetal graphene. The Dirac fluid, which effectively lives in two spatial dimensions, has also been argued to be strongly interacting at experimentally achievable temperatures [67, 60, 79, 111] due to ineffective Coulomb screening [66]. Although it is separated from the Fermi liquid by a crossover, and not a (thermal) phase transition, its proximity to a (simple) zero temperature quantum critical point at charge neutrality means that the phenomenology of the Dirac fluid is expected to differ strongly from Fermi liquid theory. Due to the high spatial dimensionality,[†] the development of a predictive quantitative theory of these systems is notoriously hard. A major theme in recent work has been quantum criticality [112, 113], which opens up the possibility for borrowing powerful techniques from high energy physics, but even in this case very little is known about experimentally relevant regime of finite temperature and density. One of the only remaining techniques for understanding these systems is hydrodynamics, as many features of hydrodynamics are universal and model independent, and the strongly interacting quantum physics is captured entirely by the coefficients in otherwise classical differential equations. Such fluids are quantum analogues of classical liquids such as water, which are strongly interacting (albeit with negligible quantum entanglement) insofar as they do not admit a controllable description via kinetic theory. Furthermore, it has been shown [87] that strongly interacting quantum critical

[†]Quantum dynamics in one dimension, which is often integrable, is described using very different techniques and has qualitatively distinct features.

fluids have a somewhat different hydrodynamic description than the canonical Fermi liquids described above, and this can lead to very different hydrodynamic properties, including in transport [87, 60, 79, 74, 73, 61, 114], as we will review in this paper.

Using novel techniques to measure thermal transport [51, 41, 10], the Dirac fluid has finally been observed in monolayer graphene, and evidence for its hydrodynamic behavior has emerged [55], as we will detail. However, existing theories of hydrodynamic transport are not consistent with the simultaneous density dependence in experimentally measured thermal and electrical conductivities. In this paper, we improve upon the hydrodynamic theory of [87], describe carefully effects of finite density, and develop a non-perturbative relativistic hydrodynamic theory of transport in electron fluids near a quantum critical point. Under certain assumptions about the equations of state of the Dirac fluid, our theory is quantitatively consistent with experimental observations. The techniques we employ are included in the framework of [88], which developed a hydrodynamic description of transport in relativistic fluids with long wavelength disorder in the chemical potential. [88] was itself inspired by recent progress employing the AdS/CFT correspondence to understand quantum critical transport in strange metals [115, 114, 116, 117, 118, 119, 120, 121, 122], but as we will discuss, this theory is also well suited to describe the physics of graphene.

7.1.1 Summary of Results

The recent experiment [55] reported order-of-magnitude violations of the Wiedemann-Franz law. The results were compared with the standard theory of hydrodynamic transport in quantum

critical systems [87], which predicts that

$$\sigma(n) = \sigma_{\text{Q}} + \frac{e^2 v_{\text{F}}^2 n^2 \tau}{\mathcal{H}}, \tag{7.2a}$$

$$\kappa(n) = \frac{v_{\text{F}}^2 \mathcal{H} \tau}{T} \frac{\sigma_{\text{Q}}}{\sigma(n)}, \tag{7.2b}$$

where e is the electron charge, s is the entropy density, n is the charge density (in units of length^{-2}), $\mathcal{H}$ is the enthalpy density, τ is a momentum relaxation time, and σ_{Q} is a quantum critical effect, whose existence is a new effect in the hydrodynamic gradient expansion of a relativistic fluid. Note that up to σ_{Q}, $\sigma(n)$ is simply described by Drude physics. The Lorenz ratio then takes the general form

$$\mathcal{L}(n) = \frac{\mathcal{L}_{\text{DF}}}{(1 + (n/n_0)^2)^2}, \tag{7.3}$$

where

$$\mathcal{L}_{\text{DF}} = \frac{v_{\text{F}}^2 \mathcal{H} \tau}{T^2 \sigma_{\text{Q}}}, \tag{7.4a}$$

$$n_0^2 = \frac{\mathcal{H} \sigma_{\text{Q}}}{e^2 v_{\text{F}}^2 \tau}. \tag{7.4b}$$

$\mathcal{L}(n)$ can be parametrically larger than $\mathcal{L}_{\text{WF}}$ (as $\tau \to \infty$ and $n \ll n_0$), and much smaller ($n \gg n_0$). Both of these predictions were observed in the recent experiment, and fits of the measured $\mathcal{L}$ to (7.3) were quantitatively consistent, until large enough n where Fermi liquid behavior was restored. However, the experiment also found that the conductivity did not grow rapidly away from

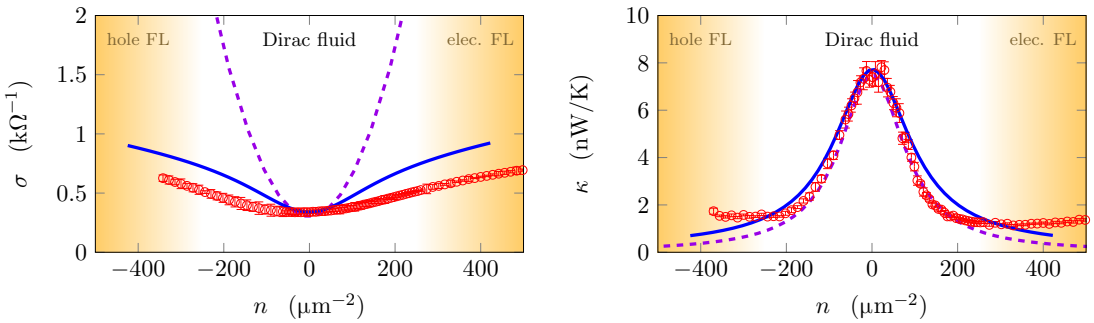

Figure 7.3: A comparison of our hydrodynamic theory of transport with the experimental results of [55] in clean samples of graphene at $T = 75$ K. We study the electrical and thermal conductances at various charge densities n near the charge neutrality point. Experimental data is shown as circular red data markers, and numerical results of our theory, averaged over 30 disorder realizations, are shown as the solid blue line. Our theory assumes the equations of state described in (7.27) with the parameters $C_0 \approx 11, C_2 \approx 9, C_4 \approx 200, \eta_0 \approx 110, \sigma_0 \approx 1.7$, and (7.28) with $u_0 \approx 0.13$. The yellow shaded region shows where Fermi liquid behavior is observed and the Wiedemann-Franz law is restored, and our hydrodynamic theory is not valid in or near this regime. We also show the predictions of (7.2) as dashed purple lines, and have chosen the 3 parameter fit to be optimized for $\kappa(n)$.

$n = 0$ as predicted in (7.2), despite a large peak in $\kappa(n)$ near $n = 0$, as we show in Figure 7.3. Furthermore, the theory of [87] does not make clear predictions for the temperature dependence of τ, which determines $\kappa(T)$.

In this paper, we argue that there are two related reasons for the breakdown of (7.2). One is that the dominant source of disorder in graphene – fluctuations in the local charge density, commonly referred to as charge puddles [81, 123, 82, 53] – are not perturbatively weak, and therefore a non-perturbative treatment of their effects is necessary.† The second is that the parameter τ, even when it is sharply defined, is intimately related to both the viscosity and to n, and this n dependence is neglected when performing the fit to (7.2) in Figure 7.3. We develop a non-perturbative hydrodynamic theory of transport which relies on neither of the above assumptions, and gives us an explicit

†See [80, 124] for a theory of electrical conductivity in charge puddle dominated graphene at low temperatures.

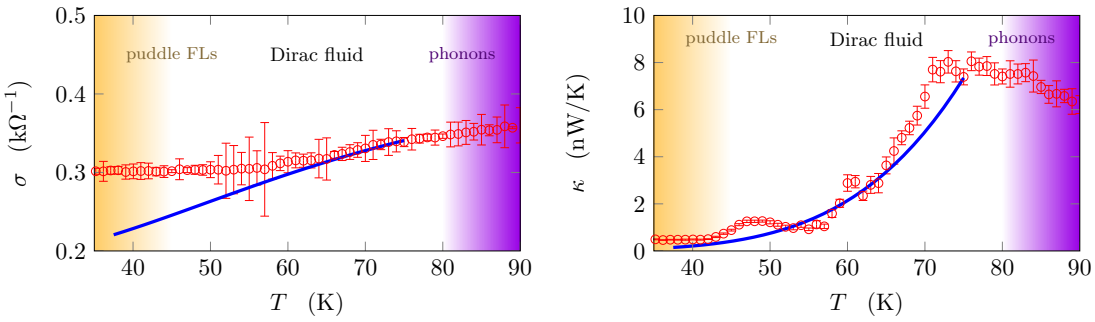

Figure 7.4: A comparison of our hydrodynamic theory of transport with the experimental results of [55] in clean samples of graphene at the charge neutrality point ($n = 0$). We use no new fit parameters compared to Figure 7.3. The yellow shaded region denotes where Fermi liquid behavior is observed; the purple shaded region denotes the likely onset of electron-phonon coupling.

formula for τ in the limit of weak disorder. The key assumption for the validity of our theory is that the size of the charge puddles is comparable to or larger than the electron interaction length scale, which is about 100 nm. Experimental evidence suggests this is marginally true in graphene samples mounted on hexagonal boron nitride [53], as was done in [55]. Although we cannot analytically solve our theory non-perturbatively, we perform numerical computations of the transport coefficients in disordered fluids, and compare the results to the experimental data in Figure 7.3. Our simultaneous fit to $\kappa(n)$ and $\sigma(n)$ shows improved quantitative agreement with both sets of data in the Dirac fluid regime. We further compare in Figure 7.4 the temperature dependence of κ and σ between our numerics and the experiment, using no new fitting parameters, and find satisfactory quantitative agreement in the Dirac fluid regime.

Figure 7.5 shows a cartoon of the regime of validity of our hydrodynamic theory. The fact that the charge puddles may be substantial, while the entropy and energy densities are much more constant, helps to explain why the perturbative description of transport is much better for κ than σ, as

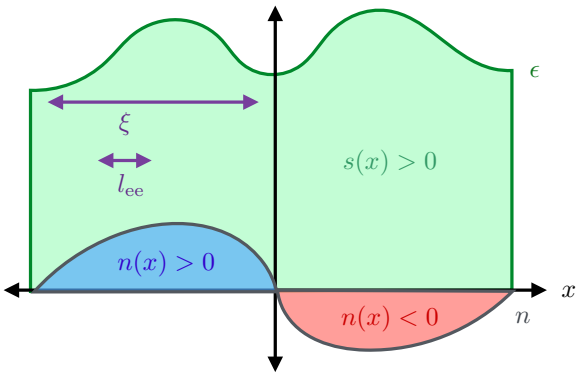

Figure 7.5: A cartoon of a nearly quantum critical fluid where our hydrodynamic description of transport is sensible. The local chemical potential $\mu(\mathrm{x})$ always obeys $|\mu| \ll k_{\rm B}T$, and so the entropy density $s/k_{\rm B}$ is much larger than the charge density $|n|$; both electrons and holes are everywhere excited, and the energy density ϵ does not fluctuate as much relative to the mean. Near charge neutrality the local charge density flips sign repeatedly. The correlation length of disorder ξ is much larger than $l_{\rm ee}$, the electron-electron interaction length.

the perturbative approach works well in a nearly homogeneous fluid. In coming years the quality of graphene samples will improve, and the charge puddle size may grow larger than 100 nm, allowing us to observe the clean hydrodynamic limit described by (7.2). As present day samples are just clean enough to observe hydrodynamics, our determination of the equations of state should be understood as preliminary.

Although the focus of this paper is on the Dirac fluid in graphene, this is because of the experimental motivation for this work. Our theory has broader validity, and we will introduce it in the more general context of transport in a disordered electronic fluid near a quantum critical point with manifest Lorentz invariance, with the microscopic Fermi velocity $v_{\rm F}$ playing the role of the speed of light. The Dirac fluid is not strictly Lorentz invariant, but we will justify the validity of our approach even in this system. While the Dirac fluid in graphene is currently the only experimentally realized strongly interacting condensed matter system with evidence for electronic hydrodynam-

ics [55], in the future surface states in topological insulators in three spatial dimensions may host strongly interacting electron fluids [125]. Strongly interacting three dimensional materials including Weyl semimetals [126, 127, 128] may also give rise to novel phenomena relevant for transport [129, 130].

7.1.2 Outline

The outline of this paper is as follows. We briefly review the definitions of transport coefficients in Section 7.2. In Section 7.3 we develop a theory of hydrodynamic transport in the electron fluid, assuming that it is Lorentz invariant. We discuss the peculiar case of the Dirac fluid in graphene in Section 7.4, and argue that deviations from Lorentz invariance are small. We describe the results of our numerical simulations of this theory in Section 7.5, and directly compare our simulations with recent experimental data from graphene [55]. The experimentally relevant effects of phonons are qualitatively described in Section 7.6. We conclude the paper with a discussion of future experimental directions. AppendixB contains technical details of our theory.

In this paper we use index notation for vectors and tensors. Latin indices $ij\cdots$ run over spatial coordinates x and y; Greek indices $\mu\nu\cdots$ run over time t as well. We will denote the time-like coordinate of A^μ as A^t. Indices are raised and lowered with the Minkowski metric $\eta^{\mu\nu} \equiv \mathrm{diag}(-1,1,1)$. The Einstein summation convention is always employed.

7.2 Transport Coefficients

Let us begin by defining the thermoelectric response coefficients of interest in this paper. Suppose that we drive our fluid by a spatially uniform, externally applied, electric field E_i (formally, an electrochemical potential gradient), and a temperature gradient $-\partial_i T$. We will refer to $-\partial_j T$ as $T\zeta_j$, with $\zeta_j = -T^{-1}\partial_j T$, for technical reasons later. As is standard in linear response theory, we decompose these perturbations into various frequencies, and focus on the response at a single frequency ω. Time translation invariance implies that the (uniformly) spatially averaged charge current $\langle J_i \rangle$ and the spatially averaged heat current $\langle Q_i \rangle$ are also periodic in time of frequency ω, and are related to E_i and ζ_i by the thermoelectric transport coefficients:

$$\begin{pmatrix} \langle J_i \rangle \\ \\ \langle Q_i \rangle \end{pmatrix} e^{-i\omega t} = \begin{pmatrix} \sigma_{ij}(\omega) & T\alpha_{ij}(\omega) \\ \\ T\bar{\alpha}_{ij}(\omega) & T\bar{\kappa}_{ij}(\omega) \end{pmatrix} \begin{pmatrix} E_j \\ \\ \zeta_j \end{pmatrix} e^{-i\omega t}. \tag{7.5}$$

In a typical disordered system, we expect that σ_{ij}, α_{ij}, $\bar{\alpha}_{ij}$ and $\bar{\kappa}_{ij}$ are all proportional to δ_{ij}. In our numerics, finite size effects introduce some anisotropy; our theory is valid in this more general scenario.

In fact, (7.5) is somewhat subtle. Implicit in the definitions of the transport coefficients are a set of boundary conditions. In the definitions in (7.5), we have assumed that we tune E_i and ζ_i, and then measure J_i and Q_i. However, usually in experiments one fixes J_i, as electronic measurements are far easier to control. One then can fix either E_i or ζ_i. So while it is straightforward to measure

σ_{ij} by setting $\zeta_i = 0$, one measures not $\bar{\kappa}_{ij}$ but instead κ_{ij}, defined as

$$\langle Q_i \rangle|_{\langle J_i \rangle = 0} = T\kappa_{ij}\zeta_j. \tag{7.6}$$

Straightforward manipulations give that $\sigma_{ij}E_j = -T\alpha_{ij}\zeta_j$, and therefore that

$$\kappa_{ij} = \bar{\kappa}_{ij} - T\bar{\alpha}_{ik}\sigma^{-1}_{kl}\alpha_{lj}. \tag{7.7}$$

These definitions are general and independent of our hydrodynamic theory.

7.3 Relativistic Hydrodynamics

We now develop a theory of relativistic hydrodynamics of the electronic plasma in a disordered metal, where the disorder is introduced by a spatially dependent chemical potential $\mu_0(\mathrm{x})$. So long as the length scale $\xi \sim |\mu_0|/|\partial_x \mu_0|$ over which this function varies is much larger than the electron-electron scattering length $l_{\mathrm{ee}} \sim \hbar v_{\mathrm{F}}/k_{\mathrm{B}}T$, it is sensible to treat the fluid as locally homogeneous, with parameters such as energy density and viscosity locally being functions of μ_0 alone. This external chemical potential acts as an external source of energy and momentum for the electronic plasma, and can be sourced by lattice defects or impurities, either in the (semi)metal itself, or in the substrate it is placed on, for two-dimensional materials such as graphene [81, 53]. Our theory here is analogous to [88], and similar to the earlier work [103] in non-relativistic fluids. However, [88] focused

mostly on the mathematical consequences of relativistic hydrodynamics, particularly in regards to holographic models. Our focus here is on practical consequences in realistic quantum critical fluids where $\mu \ll k_B T$, and where the equations of state are tightly constrained by scale invariance (see Appendix B.1).

Previous theories of hydrodynamic transport assumed that disorder was parametrically weak, and so momentum is a nearly conserved quantity [87, 60]. Such theories can be shown to be a perturbative limit of the more general approach that we advocate below: see [88] and Appendix B.3. However, near the charge-neutrality point, non-perturbative effects can become important [88]. Since this is the regime where [55] observed evidence for hydrodynamic behavior, it is necessary to treat transport in the charge-neutral fluid carefully and to study non-perturbative physics. We begin with a general discussion of the equations of state of a relativistic plasma, and then outline our non-perturbative hydrodynamic description of transport.

Though our focus in this paper is on the case of two spatial dimensions, it is straightforward to generalize our theory to higher dimensions.

7.3.1 Hydrodynamic Equations

Let us review the structure of relativistic hydrodynamics, which was derived carefully in [87]. Hydrodynamics is a general framework which describes the relaxation of an ergodic and locally thermalizing (classical or quantum) system to global thermal equilibrium, or as close to global equilibrium as boundary conditions or external sourcing allow. The assumption of local thermalization

implies that the only quantities with dynamics on long time scales (compared to the local thermalization time $l_{\text{ee}}/v_{\text{F}}$) are quantities that are globally conserved, up to external sources. In a typical theory, these will be charge, energy and momentum, and we will assume this to be the case for graphene as well. Hydrodynamics is a systematic way to truncate equations of motion for the local charge density $n(x)$, energy density $\epsilon(x)$ and momentum density $\Pi_i(x)$, by treating the perturbative parameter as $l_{\text{ee}}\partial_\mu$. In fact, it is typical to instead study the dynamics of the thermodynamic conjugate variables: chemical potential $\mu(x)$, temperature $T(x)$ and relativistic velocity $u^\mu(x)$, respectively. u^μ is subject to the usual constraint $u_\mu u^\mu = -v_{\text{F}}^2$.

Note that throughout this paper, "charge density" n refers to the number density of electrons, minus the number density of holes: $n = n_{\text{elec}} - n_{\text{hole}}$. Thus, there are no factors of e in the definition of n, or chemical potential μ.[†]

The equations of motion of hydrodynamics are the local conservation laws, up to external sources. We apply an external chemical potential μ_0 via an external electromagnetic field $A^t_{\text{ext}} = -\mu_0(\text{x})/e$, $A^i_{\text{ext}} = 0$. We employ relativistic notation with $v_{\text{F}} = 1$ temporarily. The equations of hydrodynamics are

$$\partial_\mu T^{\mu\nu} = eF^{\mu\nu}_{\text{ext}} J_\nu, \tag{7.8a}$$

$$\partial_\mu J^\mu = 0, \tag{7.8b}$$

where $F^{ti}_{\text{ext}} = -F^{it}_{\text{ext}} = \partial_i \mu_0$ are the only non-vanishing components, $T^{\mu\nu}$ represents the expecta-

[†]Therefore $[n] = [\text{length}]^{-d}$ and $[\mu] = [\text{energy}]$.

tion value of the local stress-energy density, and J^μ the expectation value of the local charge density. $T^{\mu\nu}$ and J^μ must be expressed in terms of μ, T and u^μ in order to obtain a closed set of equations. One can show that there is a static solution to the hydrodynamic equations with $u^\mu = (1,0,0)$, $T = T_0 =$ constant, and $\mu(\mathrm{x}) = \mu_0(\mathrm{x})$ [88]. Recall that $\mu_0(\mathrm{x})$ is slowly varying on the length scale ξ. We will take this solution as the background state of our fluid.

Hydrodynamics is a perturbative expansion of (7.8), where the perturbative expansion parameter is the number of derivatives of space and time. At zeroth order, the equations of state are simply that $T^{\mu\nu}$ and J^μ are given by the thermodynamic relations we derived above:

$$T^{\mu\nu} = (\epsilon + P)u^\mu u^\nu + P\eta^{\mu\nu}, \tag{7.9a}$$

$$J^\mu = nu^\mu, \tag{7.9b}$$

with ϵ the energy density and P the pressure. In the fluid's rest frame, $T^{tt} = \epsilon$, $T^{ij} = P\delta^{ij}$, and $J^t = n$, with all other components vanishing. At first order, [87] showed that the most general first derivative corrections to $T^{\mu\nu}$ and J^μ consistent with symmetries and the local second law of thermodynamics are

$$T^{\mu\nu} = (\epsilon + P)u^\mu u^\nu + P\eta^{\mu\nu} - 2\mathcal{P}^{\mu\rho}\mathcal{P}^{\nu\sigma}\eta\partial_{(\rho}u_{\sigma)} - \mathcal{P}^{\mu\nu}\left(\zeta - \eta\right)\partial_\rho u^\rho, \tag{7.10a}$$

$$J^\mu = nu^\mu - \frac{\sigma_{\mathrm{Q}}}{e^2}(\eta^{\mu\nu} + u^\mu u^\nu)\left(\partial_\nu\mu - \frac{\mu}{T}\partial_\nu T - eF_{\nu\rho,\mathrm{ext}}u^\rho\right), \tag{7.10b}$$

with $\eta, \zeta, \sigma_{\mathrm{Q}} > 0$, and $\mathcal{P}^{\mu\nu} = \eta^{\mu\nu} + u^\mu u^\nu$. Here η and ζ are the shear and bulk viscosity re-

spectively, and σ_Q is a "quantum critical" conductivity [87]. Note that the external electromagnetic fields show up in the hydrodynamic gradient expansion in the charge current; this happens because the charged fluid is sensitive only to the gradient in the total electrochemical potential [100]. We allow for P, n, η, ζ and σ_Q to all be position-dependent, with their position dependence related to μ_{ext}, as we will describe shortly in more detail.

It has long been appreciated [87] that σ_Q plays a fundamental role in hydrodynamic transport near quantum critical points. More recently [114] argued that η could play a role in transport. We will carefully detail how η affects transport in this paper, analytically and numerically.

In our extension of this theory to graphene, we will also allow for Coulomb interactions of the fluid to be substantial enough to enter the hydrodynamic equations. However, this should only alter the equations of state, as well as add a further contribution to $F_{\mu\nu,\text{ext}}$ [60], and we will detail this in the subsequent section. The constraints imposed on hydrodynamics from local positivity of entropy production [87] are unchanged in the presence of Coulomb interactions, which are entirely accounted for via a modified $F^{\mu\nu}_{\text{ext}}$.

It is sufficient in our calculation of σ, α and κ to simplify $T^{\mu\nu}$ and J^μ and retain only the terms linear in velocity. One finds, in $d = 2$:

$$T^{ti} = (\epsilon + P)v^i, \tag{7.11a}$$

$$T^{ij} = P\delta^{ij} - \eta\left(\partial^i v^j + \partial^j v^i\right) - (\zeta - \eta)\delta^{ij}\partial_k v^k, \tag{7.11b}$$

$$J^i = nv^i - \frac{\sigma_Q}{e^2}\left(\partial_i(\mu - \mu_0) - \frac{\mu}{T}\partial_i T\right). \tag{7.11c}$$

We stress the novel role of $\sigma_{\mathcal{Q}}$, a new dissipative transport coefficient in a relativistic fluid, without a direct analogue in the canonical non-relativistic fluid. This term is related to the underlying thermally excited electron-hole plasma, and the fact that electrons and holes can move in opposite directions under an applied electric field, contributing a net electric current.[†] There is no microscopic thermal conductivity – instead, all microscopic dissipation related to electric and thermal gradients is controlled by $\sigma_{\mathcal{Q}}$.

7.3.2 Hydrodynamic Theory of Transport

We are now ready to detail our hydrodynamic calculation of the transport coefficients defined in Section 7.2. We place our fluid in a box of length L in each direction, with periodic boundary conditions on the fluid in every direction. We then apply a constant background E_i and ζ_i.[‡] The static solution above is no longer a solution to the hydrodynamic equations of motion, sourced by these gradients. Now, we generically expect to excite both a spatial electric current J^i, and a spatial heat current

$$Q^i \equiv T^{ti} - \mu J^i. \tag{7.12}$$

[†]It is qualitatively similar to the bipolar diffusion effect [92, 94] – however, in hydrodynamics the quasiparticle lifetimes are limited by $\hbar/k_B T$, whereas in the bipolar diffusion effect these lifetimes are parametrically long, as in a Fermi liquid.

[‡]The application of a constant ζ_j on a periodic space is the reason why we cannot talk about driving the system with a constant temperature gradient, since the temperature is a periodic function in space. One can formally implement ζ_i through deformations of the spacetime metric and external gauge fields [131].

We can expand out J^i and Q^i locally as a Taylor series in E_i and ζ_i. The transport coefficients in Section 7.2 are defined by retaining only the linear terms in E_i and ζ_i, and spatially averaging over the local charge and heat currents. It is sufficient to perform a linear response calculation about our previously identified static solution:

$$\mu \approx \mu_0(\mathrm{x}) + \delta\mu(\mathrm{x})\mathrm{e}^{-\mathrm{i}\omega t}, \tag{7.13a}$$

$$T \approx T_0 + \delta T(\mathrm{x})\mathrm{e}^{-\mathrm{i}\omega t}, \tag{7.13b}$$

$$u^t \approx 1, \tag{7.13c}$$

$$u^i \approx \delta v^i(\mathrm{x})\mathrm{e}^{-\mathrm{i}\omega t}, \tag{7.13d}$$

and then solve the linearized hydrodynamic equations – this is equivalent to only keeping terms linear in E_i and ζ_i in the full solution. For ease of notation, we drop the "δ" in front of the linear response perturbations in the remainder of the paper, but one should keep in mind that $\mu(\mathrm{x})$, $T(\mathrm{x})$, and v^i are henceforth perturbatively small quantities.

Following [88], the linearized hydrodynamic equations (7.8) can be shown to take the following

form:[†]

$$\begin{pmatrix} -e^{-2}\partial_i\sigma_Q\partial_i & e^{-2}T_0^{-1}\partial_i\mu_0\sigma_Q\partial_i & \partial_j n \\ e^{-2}\partial_i\mu_0\sigma_Q\partial_i & -e^{-2}T_0^{-1}\partial_i\mu_0^2\sigma_Q\partial_i & T_0\partial_j s \\ n\partial_i & s\partial_i & -\partial_i(\zeta-\eta)\partial_j - \partial_i\eta\partial_j - \partial_j\eta\partial_i \end{pmatrix} \begin{pmatrix} \mu \\ T \\ v_j \end{pmatrix}$$
$$= \begin{pmatrix} -e^{-1}\partial_i\sigma_Q(E_i - \mu_0\zeta_i/e) \\ e^{-1}\partial_i\sigma_Q\mu_0(E_i - \mu_0\zeta_i/e) \\ enE_i + T_0 s\zeta_i \end{pmatrix} \tag{7.14}$$

Here

$$s = \frac{\epsilon + P - \mu_0 n}{T_0} \tag{7.15}$$

is the entropy density of the background fluid. s and n are not independent, and are related by thermodynamic Maxwell relations: see Appendix B.1. We have also employed

$$\partial_i P = n\partial_i\mu + s\partial_i T. \tag{7.16}$$

In particular, s and n are position dependent functions whose position dependence is entirely determined by the local chemical potential: $s(\mathrm{x}) = s(T_0, \mu_0(\mathrm{x}))$, and similarly for n, η, and all other coefficients in the hydrodynamic equations. The proper boundary conditions to impose on μ, T and v_j are periodicity. This forms a well-posed elliptic partial differential equation and can be numerically solved: see Appendix B.5. Combining (7.11) and (7.12), along with μ, T and v^i as found

[†]In this equation, derivatives act on all fields to the right, so $\partial_x\eta\partial_x v^x$ should be read as $\partial_x(\eta\partial_x v^x)$.

from solving the linear system (7.14), we obtain $J_i(E_j, \zeta_j)$ and $Q_i(E_j, \zeta_j)$. Spatially averaging these quantities and employing (7.5), we obtain σ_{ij},α_{ij} and $\bar{\kappa}_{ij}$.

We cannot exactly compute these transport coefficients in general. However, one can prove [88] that Onsager reciprocity holds. This is a non-trivial consistency check on the validity of our approach. Furthermore, there exist scaling symmetries combining re-scalings of μ, T and v_i, as well as the equations of state; these are listed in Appendix B.2. These are helpful when we fit this theory to the data of [55]. These scaling symmetries are also present in the theory of [87], with the exception of a further scaling symmetry which only affects the viscosity and the length scale of disorder in this theory.

In the limit where

$$\mu_0 = \bar{\mu}_0 + u\hat{\mu}(x), \tag{7.17}$$

with $\hat{\mu}$ an O(1) function but $u \ll \bar{\mu}_0$, the transport coefficients may be perturbatively calculated analytically, and for $\mu \ll k_B T$, we find that

$$\sigma \approx \frac{e^2 v_F^2 n^2 \tau}{\epsilon + P}, \tag{7.18a}$$

$$\alpha \approx \frac{e v_F^2 n s \tau}{\epsilon + P}, \tag{7.18b}$$

$$\bar{\kappa} \approx \frac{v_F^2 T s^2 \tau}{\epsilon + P}, \tag{7.18c}$$

and we find an analytical expression for τ with the following approximate form near the Dirac

point:

$$\frac{1}{\tau} \approx \frac{v_F^2 u^2}{2} \left(\frac{\partial n}{\partial \mu}\right)^2 \left[\frac{e^2}{\sigma_Q(\epsilon + P)} + \frac{\eta + \zeta}{\xi^2} \frac{4\mu^2}{(\epsilon + P)^3}\right]. \tag{7.19}$$

Details of this calculation and a more precise (and complicated) formula are given in Appendix B.3. The requirement that we are "far" from the Dirac point is that $\sigma_Q \ll e^2 v_F^2 n^2 \tau/(\epsilon + P)$. Everything in (7.19) except for u is evaluated in the clean fluid with $u \to 0$. (7.19) makes clear that if η/ξ^2 is large, the n and μ dependence of τ is not negligible even when $\mu \ll k_B T$, and we will verify this in numerical simulations in Section 7.5. The validity of (7.2) for κ is not guaranteed far from the Dirac point in this perturbative limit, but can often be quite good in practice, when the density dependence of all parameters is accounted for. Combining (7.18) and (7.19), we obtain the relativistic analogue of the perturbative results of [103].

Noting that $n \sim \mu$ as $\mu \to 0$, careful study of (7.2) shows that the Lorentzian form of $\kappa(n)$ is not altered by plugging in this hydrodynamic formula for τ, while the form of $\sigma(n)$ can be quite distinct, with $\sigma(n)$ no longer growing quadratically at larger n. This helps explain why in Figure 7.3, (7.2) gave a quantitatively good fit to $\kappa(n)$, but not to $\sigma(n)$.

7.4 The Dirac Fluid in Graphene

The previous section developed a general theory for relativistic fluids. It is often said that the Dirac fluid in graphene is a "quantum critical" system in two spatial dimensions [132, 67, 73], and exhibits behavior analogous to the quantum critical regime at finite temperatures above the superfluid-

insulator transition, although technical differences arise. Let us review elementary features of the quantum critical behavior of graphene, and argue that our formalism remains appropriate for transport computations.

Assuming that the electrons in graphene are non-interacting, standard band theory calculations on a honeycomb lattice in two spatial dimensions with nearest-neighbor hopping give two species of Dirac fermions with low-energy dispersion relation

$$\epsilon(\mathrm{q}) \approx \hbar v_{\mathrm{F}} |\mathrm{q}|, \tag{7.20}$$

Convincing experimental evidence for these massless Dirac fermions was given in [64, 65]. There is a quantum critical point between electron and hole Fermi liquids at zero temperature in graphene, as the chemical potential μ is tuned through the Dirac point, $\mu = 0$. At (any experimentally accessible) finite temperature T, and at $\mu \ll T$, an effectively relativistic plasma of electrons and holes forms, interacting via a $1/r$ Coulomb potential. The strength of these Coulomb interactions is captured by a dimensionless number α_0 analogous to the fine structure constant:

$$\alpha_0 = \frac{e^2}{4\pi\epsilon_0\epsilon_{\mathrm{r}}\hbar v_{\mathrm{F}}} \approx \frac{1}{137}\frac{c}{\epsilon_{\mathrm{r}} v_{\mathrm{F}}}, \tag{7.21}$$

where $\epsilon_{\mathrm{r}} \sim 4$ is a dielectric constant, $c \approx 3 \times 10^8$ m/s is the speed of light, $v_{\mathrm{F}} \approx 1.1 \times 10^6$ m/s is the Fermi velocity in graphene and e is the charge of the electron. In experiments, $\alpha_0 \sim \mathrm{O}(1)$, and so unlike quantum electrodynamics ($\alpha_{\mathrm{QED}} \approx 1/137$), interactions are *strong*. v_{F} plays the role of the

speed of light in an effectively relativistic electron-hole plasma, and in an experimentally accessible regime which we describe below, one can use relativistic hydrodynamics to model thermoelectric transport in graphene.

The exception to the emergent Lorentz invariance is the photon-mediated Coulomb interactions, which are the standard $1/r$ interaction of three spatial dimensions. Further, because $v_F \sim c/300$, the Coulomb interaction is essentially non-local and instantaneous in time. Despite this, graphene shares many features with a truly relativistic plasma with "speed of light" v_F, including a "quantum critical" diffusive conductivity σ_Q [74].

Analogously to in quantum electrodynamics, α is a marginally irrelevant interaction, and so the effective coupling constant runs. At temperature $T \to 0$, we should replace α_0 with [67]

$$\alpha_{\text{eff}} = \alpha_0 \left(1 + \frac{\alpha_0}{4} \log \frac{\Lambda}{T_0}\right)^{-1} \tag{7.22}$$

where $\Lambda \sim 8.4 \times 10^4$ K is a cutoff related to the graphene band structure (the energy scale at which the dispersion is no longer linear). Note that although the running of α_{eff} causes a logarithmically increasing velocity v_F in (7.20), when we write v_F in this paper, we are always referring to the bare velocity, 1.1×10^6 m/s.

At the experimentally accessible temperatures ($T_0 \sim 70$ K) where the plasma described above is most likely not suppressed by local disorder in μ [55], (7.22) gives $\alpha_{\text{eff}} \sim 0.25$. And so the experiments likely probe the dynamics of a strongly interacting quasi-relativistic plasma. It is such a regime where hydrodynamics is a good approximation. More carefully, the electron-electron scattering

length has quantum critical scaling [74]

$$l_{ee} \sim \frac{\hbar v_F}{\alpha_{eff}^2 k_B T_0} \sim 100 \text{ nm}, \tag{7.23}$$

where we have plugged in for experimentally reasonable values of the parameters. Indeed, pump-probe experiments provide evidence that the electron-electron interaction time, $l_{ee}/v_F \sim 10^{-13}$ s, is consistent with (7.23) [70, 72]. Furthermore, it is believed that the dominant source of disorder in graphene are charge puddles, which are fluctuations in the local charge density. It is now possible to find samples of graphene where these fluctuations are correlated on the length scale (7.23) [53]. In these cleanest samples, the experimental evidence thus points to the validity of a hydrodynamic description, such as the one we advocate in this paper.

Most computations of the thermodynamic and hydrodynamic coefficients in graphene are based on kinetic theory, which requires a quasiparticle description to be sensible, and so are valid as $\alpha_{eff} \to 0$ ($T_0 \to 0$), when the plasma becomes weakly interacting. However, the experiments are likely not in this weakly interacting regime, and $\log \alpha_{eff}$ corrections to these properties are not negligible. As such, we will allow *all* coefficients in the equations of motion to be fit parameters. We will also neglect the fact that the running of $\alpha_{eff}(T_0)$ allows for certain thermodynamic relations for a strictly scale invariant, relativistic fluid to be violated. This assumption is justified in Appendix B.4.

We must also take into account the long range Coulomb interactions in our hydrodynamic description. This can be done following [60]. The Coulomb potential introduces a local electric field

and must be included in $F^{\mu\nu}_{\text{ext}}$:

$$A^t_{\text{ext}} = \mu_{\text{ext}} - \varphi = \mu_{\text{ext}} - \varphi_{\text{ext}} - \delta\varphi \tag{7.24}$$

where

$$\varphi(\mathrm{x}) = \int \mathrm{d}^2\mathrm{y}\; K(\mathrm{x}-\mathrm{y})\; n(\mathrm{y}), \tag{7.25}$$

with K a Coulomb kernel whose specific form [95] is not necessary for our purposes, and the n the charge density. At $T_0 = 0$, $K(r) = \alpha_{\text{eff}}/r$; at finite T_0, this is cut-off at long wavelengths due to thermal screening [95]. In (7.24) we have separated the effects of Coulomb screening into two contributions: φ_{ext}, which alters the background disorder profile, so that $\mu_0 \neq \mu_{\text{ext}}$, and $\delta\varphi$, which is the infinitesimal Coulomb potential created by the change in charge density δn, proportional to E_i and ζ_i.

The time-independent equations of motion depend only on T, v_i, the sources E_i and ζ_i, and the electrochemical potential

$$\delta\Phi \equiv \delta\mu + \delta\varphi. \tag{7.26}$$

This is a direct consequence of the tightly constrained way that F_{ext} and μ enter the hydrodynamic gradient expansion. If we solve for $\delta\Phi$ instead of $\delta\mu$, we find that Coulomb screening does not affect dc transport at all: more precisely, the equations of motion are identical to those in Section 7.3, but with $\delta\Phi$ replacing $\delta\mu$. That dc transport is insensitive to Coulomb screening of the hydrodynamic degrees of freedom was also noted in [60] in a homogeneous fluid by appealing to the random phase

approximation.[†] It is therefore appropriate to directly apply the formalism of Section 7.3 to study dc thermal and electric transport in the Dirac fluid in graphene. To maintain notation with Section 7.3, we will continue to refer to Φ as μ in our linear response theory, with the understanding that this includes corrections due to Coulomb screening.

7.5 Numerical Results

Having argued that the theory of Section 7.3 is an acceptable approximation for dc transport in the Dirac fluid in graphene, we now present the results of numerical simulations of (7.14). In our numerics, we assume that the equations of state of the graphene fluid are as follows:

$$n(\mu_0) = \left(\frac{k_B T_0}{\hbar v_F}\right)^2 \left[C_2 \frac{\mu_0}{k_B T_0} + C_4 \left(\frac{\mu_0}{k_B T_0}\right)^3\right], \tag{7.27a}$$

$$s(\mu_0) = \frac{k_B^3 T_0^2}{(\hbar v_F)^2} \left[C_0 + \frac{C_2}{2} \left(\frac{\mu_0}{k_B T_0}\right)^2 - \frac{C_4}{4} \left(\frac{\mu_0}{k_B T_0}\right)^4\right], \tag{7.27b}$$

$$\eta(\mu_0) = \frac{(k_B T_0)^2}{\hbar v_F^2} \eta_0, \tag{7.27c}$$

$$\zeta(\mu_0) = 0, \tag{7.27d}$$

$$\sigma(\mu_0) = \frac{e^2}{\hbar} \sigma_0, \tag{7.27e}$$

with $C_{0,2,4}$, σ_0 and η_0 dimensionless constants. The form of n and s are consistent with thermodynamic Maxwell relations – see Appendix B.1. We take the disorder profile to be random sums of sine

[†] See also the discussion in [100, 133].

waves, and normalize the disorder distribution so that

$$\left\langle (\mu_0 - \bar{\mu}_0)^2 \right\rangle = u_0^2 (k_B T_0)^2. \tag{7.28}$$

The shortest wavelength sine wave in the problem is taken to have wavelength $\xi = l_{ee}$ in all of our numerics. There is an exact symmetry of the problem under which ξ can be made arbitrary, so long as we rescale η and ζ by a factor of $(\xi/l_{ee})^2$ – see Appendix B.2. We have chosen this value of ξ as it is roughly consistent with previous experimental observations [53], and also the smallest value for which a hydrodynamic description is sensible. More details on numerical methods are in Appendix B.5.

An example of our numerical results is shown in Figure 7.6, where the results of varying the dimensionless viscosity η_0 are shown. When the charge puddle sizes are $\sim$ 20 K, as in experiment [53], the value of η_0 dramatically alters the transport coefficients as a function of density. In particular, the $\sigma(n)$ and $\alpha(n)$ curves are substantially flattened, an effect which is predicted using (7.19). Further, the peak in $\kappa(n)$ is substantially smaller than predicted perturbatively, and $\kappa(n)$ does not shrink to 0 as $n \to \infty$, as predicted in [87]. In contrast, in a limit of extremely weak disorder (temperature at which the Dirac fluid emerges $\sim$ 0.2 K), the transport coefficients are relatively insensitive to the viscosity (assuming that $\eta_0/C_0 \sim 1$, as expected for a strongly interacting quantum fluid).

We also show the consequences of a non-zero C_4 in Figure 7.7. The most important effect of C_4 is that n and $\bar{\mu}_0$ are no longer proportional – in particular, when $C_4 > 0$ we see that at larger

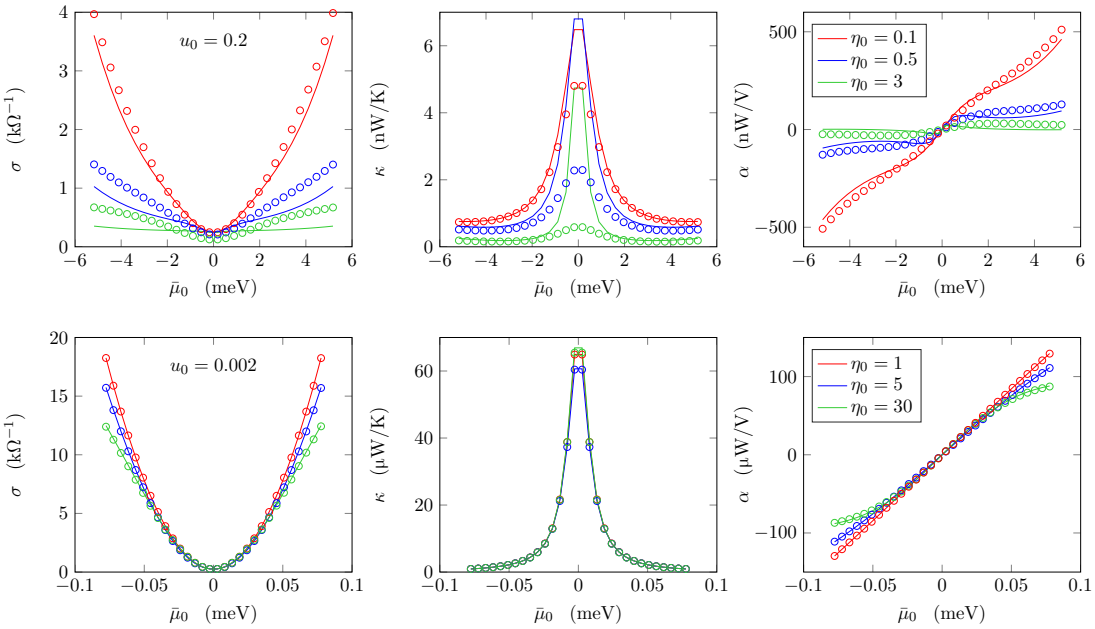

Figure 7.6: Numerical computations of transport coefficients with $C_1 = C_2 = \sigma_0 = 1$ and $C_4 = 0$. The top row has $u_0 = 0.2$, and the bottom row has $u_0 = 0.002$. Solid lines are our theoretical results (using the particular disorder realizations studied) and the circular markers are numerical results. Averages are taken over 20 disorder realizations. $T_0 = 75$ K and we employ the value of v_F in graphene.

n both σ and α decrease much more slowly with n. Whenever $C_4 \neq 0$, the equations of state become badly behaved at large μ, because $s(\mu)$ or $n(\mu)$ becomes a non-monotonically increasing function. At lower temperatures ($T \lesssim 50$ K) in Figure 7.4, this begins to be an issue in the codes for the equations of state we use to compare to experiment. This implies that higher order terms in the equations of state (associated with more fit parameters) are necessary.

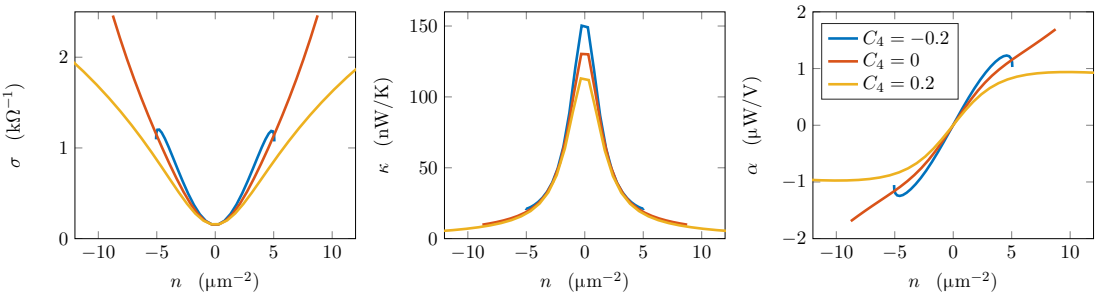

Figure 7.7: Numerical computations of transport coefficients with varying $C_4, C_1 = \sigma_0 = 1, \eta_0 = 3, C_2 = 0.2$ and $u_0 = 0.2$. The sharp change in behavior when $C_4 < 0$ is a consequence of $n(\mu)$ not being monotonically increasing at large μ. Averages are taken over 20 disorder realizations. $T_0 = 75$ K and we employ the value of v_F in graphene.

7.5.1 Comparison to Experiment

We now describe in more details the lessons to be drawn from our fit to experimental data, shown in Figures 7.3 and 7.4. Due to a total of 6 fit parameters (3 which determine the overall scales in the plots, and 3 which alter the shapes of curves), we did not perform an exhaustive analysis and find a statistically optimal fit. We found that most choices of parameters do not agree well with data, and the fit we have presented serves as a proof of principle that hydrodynamics can explain many important features of the experiment [55], as we now discuss.

To obtain data at lower temperatures, we have taken disorder realizations from $T_0 = 75$ K, using our standard assumption $\xi = l_{ee}(T_0 = 75\ \text{K})$, and simply lowered the temperature. We also keep $u_0 T_0$ constant as a function of T_0. Formally, this implies that at lower temperatures $\xi < l_{ee}$, as $l_{ee} \sim T^{-1}$; this may be problematic for the validity of hydrodynamics. A conservative solution, employing the rescaling symmetries of our theory, is to simply double ξ, and quadruple η_0: all data

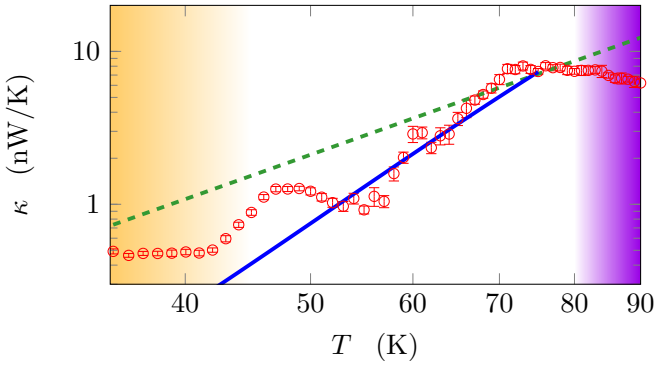

Figure 7.8: A comparison of our numerical computation of $\kappa(T)$ with experimental results of [55] at the charge neutrality point ($n = 0$). The red data points are experimental data from [55], the blue curve is our disorder-averaged simulation (using identical parameters to Figure 7.4), and the green dashed curve is the perturbative prediction $\kappa \sim T^3$ for comparison. Data is shown on a log-log scale. The yellow shaded region denotes where Fermi liquid behavior is observed; the purple shaded region denotes the likely onset of electron-phonon coupling.

is exactly identical, except that for all data points taken in Figure 7.4, $\xi > l_{ee}$ and η_0 increases.

Figure 7.8 revisits the T-dependence in κ. Assuming that disorder is weak, we employ (7.18) and (7.19) to determine the scaling of κ: since $s \sim T^2$, $\epsilon + P \sim T^3$, $\partial n/\partial \mu \sim T$, and the viscosity dependence in τ is negligible, we obtain $\tau \sim T$ and $\kappa \sim T^3$. That numerics and experiment are not consistent with this power law is a sign of the strong non-perturbative effects, and suggests that observing power law signatures of hydrodynamics may only be possible in the cleanest samples: see Figure 7.8. Figure 7.9 suggests that the sharp dependence in T observed in experiment is a consequence of $C_4 > 0$ and is not a robust scaling regime.[†] As noted in [55], this dramatic T-dependence of κ, in contrast with the very weak T-dependence of σ, at the Dirac point, is a tell-tale sign of hydrodynamics that is not captured by competing theories, such as the bipolar diffusion effect.

The fits to $\sigma(n)$ and $\sigma(T)$ are not as good as the fits to κ. Nonetheless, our theory does help to

[†]For this particular simulation, the disorder becomes large enough at $T \lesssim 7.5$ K that disorder realizations with $C_4 = 0.1$ sometimes have unphysical thermodynamic behavior.

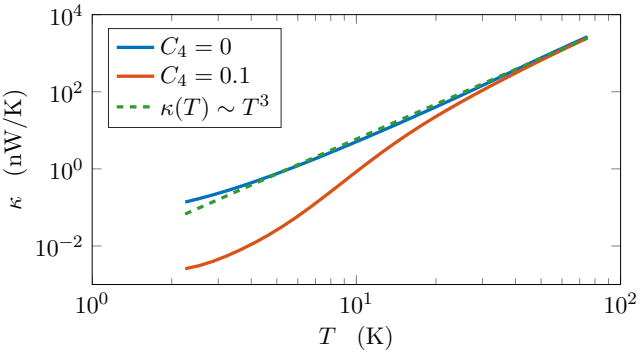

Figure 7.9: A comparison of $\kappa(T)$ in simulations with varying C_4. We take $C_0 = 1, C_2 = \eta_0 = 0.1, \sigma_0 = 1$, $u_0 = 0.1$ (at $T_0 = 75$ K). At large T both scenarios have $\kappa \sim T^3$; at lower T the fluid with $C_4 > 0$ undergoes a dramatic drop in $\kappa(T)$, similar to that observed in experiment.

explain the slow growth in σ away from the Dirac point, as a consequence of a fluid with both non-negligible viscosity and large disorder, as in Figure 7.6. Our simulations also correctly predict that the conductivity is an increasing function of T, an entirely non-perturbative effect, in Figure 7.4. This is at odds with predictions from kinetic theory in the Dirac fluid, which predict that $\sigma(n = 0, T) \sim \alpha_{\text{eff}}^{-2}$ should be decreasing with T due to the T-dependence in α_{eff} [74]. Any residual contact resistance [50] will also increase the growth rate of $\sigma(n)$ away from the Dirac point, and as such will be closer fit by our numerical results in Figure 7.3.

The most surprising thing about the fit is the large values of all coefficients, compared to previous theories. For example, it is predicted [132, 67] that $C_0 \lesssim 3.4$, and we find $C_0 \sim 10$. This is a direct consequence of the large values of the density n over which the Dirac fluid is present (as measured by where strong deviations from the Wiedemann-Franz law occur). The naive theoretical estimate is that the Dirac fluid should not extend past about $n \sim 40\ \mu\text{m}^{-2}$,[†] yet we see the Dirac fluid all the

[†]We have used theoretically predicted values of C_0 and C_2 [67], and assumed that the Dirac fluid ends when the μ-dependent contribution to s is comparable to the T-dependent contribution.

way to about $n \sim 200\ \mu\text{m}^{-2}$; we will comment more on this issue shortly. As in non-relativistic fluid dynamics, our hydrodynamic theory has a large number of rescaling symmetries (Appendix B.2), and these rescaling symmetries turn out to lead to very large values for all hydrodynamic coefficients as a consequence of the large scale on the density axis in Figure 7.3.

Another consequence of this rescaling is a dramatically large shear viscosity: $\eta_0 \sim 100$. It is now canonical to normalize this by the entropy density, and so the "proper units" to measure η in are $\eta_0/C_0 \approx 10$. This scaling is a consequence of a proposition [90] that strongly coupled theories would have $\eta/s \approx \hbar/4\pi k_B$, or $\eta_0/C_0 \approx 1/4\pi$. The viscosity is a helpful measure of the interaction strength in a theory; if the interactions are perturbatively controlled by a small parameter g, then we expect $\eta \sim g^{-2}$; only when the interaction strength is large can $\eta \sim s$, up to a prefactor of order unity. Hence, coming close to saturating the bound of [90] is a signature that the fluid is strongly interacting. Our estimate for η_0/C_0 is about 100 times larger than the bound of [90]. Smaller values of $\eta/s \sim 0.5\hbar/k_B$ have been reported in other experiments in cold atomic gases [58] and quark-gluon plasma [134]. The possibility of adding the Dirac fluid to a list of strongly interacting quantum fluids is tantalizing, and a more direct measure of η in the Dirac fluid is of interest.

One possibility is that our bare coefficients C_0, η_0 etc. are anomalously large because [55] has measured the average charge density in the entire sample. However, some regions of the sample (notably close to the contacts on the edges [135], or regions very close to impurities) may have such large local values of μ_0 that they are always in a Fermi liquid regime. So long as these Fermi liquid regimes do not percolate across the entire sample, our hydrodynamic description of transport may be quite reasonable in the bulk. However, these regions have a much smaller compressibility, and

so can absorb a lot of charge relative to a clean Dirac fluid. It may be that the total averaged charge density is then not equal to the averaged hydrodynamic charge density, leading us to overestimate n. Rescaling $n \to \lambda n$ would rescale $C_0 \to \lambda C_0$ and $\eta_0 \to \lambda^2 \eta_0$. Choosing $\lambda = 0.2$, in accordance with our previous estimates on the regime of the Dirac fluid at $T_0 \sim 75$ K, we obtain $C_0 \sim 2$ and $\eta_0/C_0 \sim 2$, which are both reasonable for a strongly interacting fluid.

As noted previously, we expect that future measurements in cleaner samples may give a wider separation between l_{ee} and ξ. Together with a better understanding of edge effects and the charge puddle profile, we expect this approach to lead to cleaner estimates of $C_{0,2,4}$, η_0 and σ_0.

7.6 Phonons in Graphene

Throughout this work we have neglected the effects of electron-phonon coupling in graphene [51, 41]. In this section, we provide some brief qualitative comments on the role of electron-phonon coupling in the experiment [55], and discuss signatures for future experiments.

Generically, phonons extract both energy and momentum from the electronic fluid, and in doing so hamper a hydrodynamic description.[†] In graphene, the acoustic branch(es) of phonons have dispersion relation [138]

$$\omega_{ac}(q) \approx \hbar v_a |q| \tag{7.29}$$

with $v_a \approx 2 \times 10^4$ m/s and so $v_a \ll v_F$. By considering conservation of energy and momentum

[†]The hydrodynamic description of transport reduces to a diffusion equation for the conserved electrical current. Historically, this was modeled via resistor networks [136, 137].

in electron-phonon scattering events, one finds that the phonon energies are negligible, and thus the scattering event can be treated as elastic from the point of view of the electrons.

If only acoustic phonons couple to the electronic fluid, we may approximate that the momentum conservation equation is modified, following the phenomenology of [87]:

$$\partial_\mu T^{\mu i} \approx F^{\nu i}_{\text{ext}} J_\nu - \frac{T^{ti}}{\tau_{\text{a}}}. \tag{7.30}$$

The latter term implies that the momentum of the electronic fluid degrades at a constant rate τ_{a}^{-1}, which we take to be

$$\frac{1}{\tau_{\text{a}}} = \mathcal{B} T^a, \tag{7.31}$$

where $a > 0$ and $\mathcal{B} > 0$ are constants that are phenomenological. [138] computed their values using kinetic theory and found $a = 4$ far from the Dirac point. This effect has been observed experimentally [40], but a is expected to change near the Dirac point. Following arguments similar to [20, 138], we can estimate a by assuming a quasiparticle description of transport, and that the dominant events are absorption or emission of a single phonon. Since acoustic phonons cannot effectively carry away energy, a Dirac quasiparticle of energy ϵ can scatter into $\sim \epsilon$ states. All phonons with relevant momenta are thermally populated, and we estimate the scattering rate to be proportional to the momentum of the phonon. Thus we estimate, using that the typical quasiparticle energy is $\epsilon \sim T$, $a = 1 + 1 = 2$.[†]

[†]As there is no large Fermi surface with $\mu \gg k_{\text{B}} T$, no further corrections to a are necessary, as in usual metals.

Assuming that the charge puddles are small and can be accounted for perturbatively, κ is approximately given by (7.2) at the Dirac point, with

$$\frac{1}{\tau} \approx \frac{u^2}{2\sigma_Q(\epsilon + P)} \left(\frac{\partial n}{\partial \mu}\right)^2 + \mathcal{B}T^a = \frac{\mathcal{A}u^2}{T^b} + \mathcal{B}T^a. \tag{7.32}$$

Our analytic theory predicts $b = 1$. The contribution κ from electron-phonon coupling is negligible so long as

$$T \ll T^* \equiv \left(\frac{\mathcal{A}}{\mathcal{B}} u^2\right)^{\frac{1}{b+a}}. \tag{7.33}$$

Note that $T^*(u)$ is an increasing function – the weaker the disorder, the lower the temperature at which electron-phonon coupling cannot be neglected in the Dirac fluid. The thermal conductivity scales as

$$\kappa \sim \begin{cases} T^{2+b} & T \ll T^* \\ T^{2-a} & T \gg T^* \end{cases} \tag{7.34}$$

If $a > 2$, we find phenomenology quite similar to that observed in [55], with $\kappa(T)$ growing non-monotonically. We also find that

$$\kappa(T^*) = \mathcal{C}(T^*)^{2-a}, \tag{7.35}$$

a result which can be tested in experiment by measuring T^* via the peak in κ for different samples. The prefactor of this proportionality $\mathcal{C}$ may not be very sensitive to the particular sample, since it is independent of u. Figure 7.10 shows a sketch of $\kappa(T)$, accounting for acoustic phonons, in three samples with different disorder strengths u. This mechanism is also consistent with the fact that

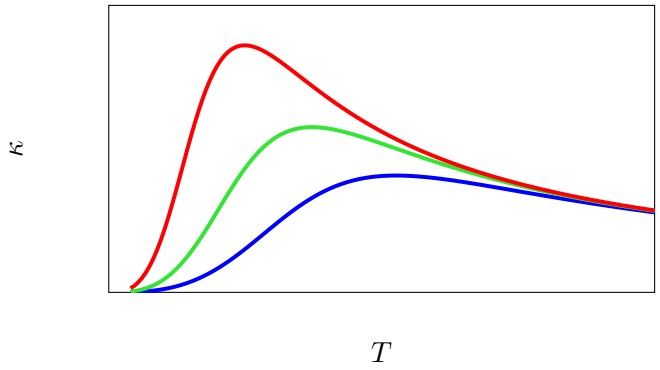

Figure 7.10: A sketch of $\kappa(T)$, accounting for coupling to acoustic phonons, for samples of graphene with three different amounts of disorder (measured by u). We take $a = 3, b = 1$ in this plot.

the cleaner samples in [55] had peaks in $\kappa(T)$ at lower temperatures, which suggests our proposed mechanism for the non-monotonicity in $\kappa(T)$ is sensible. Although our perturbative quasiparticle-based argument found $a = 2$ above, the presence of local charge puddles may increase the effective value of a to somewhere between 2 and 4, and lead to $\kappa(T^*)$ be a decreasing function. A careful analysis of electron-phonon coupling in disordered Dirac fluids is worth more study.

At higher temperatures, we expect optical phonons to couple non-negligibly to the electron fluid. These phonons can exchange both energy and momentum effectively, and at this point we expect the measured thermal conductivity to increase due to electron-phonon coupling. In [55], there is a sharp upturn in $\kappa(T)$ at all densities at temperatures of 100 K, which is likely due to activation of optical phonons in the boron nitride substrate [10].

7.7 Conclusions

We have developed a theory of transport in realistic hydrodynamic electron fluids near a quantum critical point. This theory provides a substantially improved quantitative fit to $\kappa(n)$ and $\sigma(n)$ *simultaneously*. We have further found reasonable quantitative fits to $\sigma(T)$ and $\kappa(T)$ at the Dirac point, giving us valuable information about the mechanism of momentum relaxation beyond the theory of [87].

Although we have managed to find fluids where the growth in $\sigma(n)$ is quite slow, there are still differences between the shape of $\sigma(n)$ found numerically and in experiment. There are numerous possibilities for residual discrepancies. One of the most important possibilities is that the disorder is so strong that the full thermodynamic equation of state is necessary – in this paper, we have only kept the three leading order terms. Alternatively, we may simply not have found the correct equation of state of graphene. A disorder profile more subtle than superimposed sines and cosines may also be responsible for deviations with our theory, although our investigation into this possibility suggests that other disorder profiles cause $\sigma(n)$ to have more substantial density dependence. We have assumed that the disorder profile is unaltered both by changes in T and in $\bar{\mu}_0$. This is a very strong assumption and need not be true. Finally, there may be other sources of momentum relaxation, such as out-of-plane distortions in the graphene lattice, or interactions with phonons. An understanding of the aforementioned issues is an important future task, though may be quite challenging given the possibility that strong interactions in the Dirac fluid at $T \sim 70$ K may lead to the

failure of standard perturbative techniques. The most fruitful direction for resolving at least some of these questions may be directly in experiments: for example, techniques to directly resolve the local charge density on length scales $\lesssim 10$ nm are well known [53], and can shed light into the evolution of μ_0 as a function of T, as well as the spatial correlations in μ_0.

Experimentally, it may be possible to generate samples of graphene with much weaker charge puddles using suspended devices [139, 140]. Thermodynamic measurements can also be used to determine the coefficients $C_{0,2,4}$, though these measurements are complicated by the presence of disorder, as we discuss in Appendix B.1. Nonetheless, measurements of the specific heat and compressibility in the Dirac fluid will serve as valuable guideposts for future hydrodynamic models. Such measurements have been made in the Fermi liquid [81], and their extension to the Dirac fluid form the basis for worthwhile experiments.

Previous experiments which measured the ac conductivity [141] were not in the hydrodynamic limit. Comparing the momentum relaxation time τ between measurements of κ, and a putative Drude peak in ac transport, may provide a quantitative test of our theory. Studying magnetotransport [87] may also be a fruitful direction in experiments. A theoretical discussion of transport at finite frequency and magnetic field beyond the weak disorder limit will appear elsewhere. The thermopower of graphene has recently been measured at $T \sim 200$ K [142], and it would be interesting to measure σ, α and κ in the same sample in the Dirac fluid and compare with our hydrodynamic formalism.

8

Magneto-thermal transport

Extending thermal transport studies of two-dimensional systems into high magnetic fields will facilitate a new wave of condensed matter experiments. Paired with electrical transport, thermal techniques are sensitive to inter-particle scattering [60, 55, 89], quantum criticality [113, 74], charge-less excitation channels [75, 143, 144, 145, 146, 147, 148], and can even be used to extract the entropy

of a system through the Gibbs relations [149]. Furthermore, Johnson noise and Joule heating are particularly suited to magnetic experiments as, in the linear diffusive regime†, the ratio of the Johnson noise temperature (section 2.2) to the heating power P is insensitive to the current profile or form of the conductivity tensor (section 4.3) while remaining quite sensitive to the ballistic, chiral nature of quantum Hall states.

The techniques and methods applied in this chapter are described in detail in chapters 2 and 4.

8.1 Generalized transport coefficients

In the presence of a magnetic field, an electric field in a conductor can induce a current with a component perpendicular to the applied fields. In general, the transport coefficients (σ, α, and $\bar{\kappa}$) take on a tensorial form ($\hat{\sigma}$, $\hat{\alpha}$, and $\hat{\bar{\kappa}}$) such that

$$\begin{pmatrix} \vec{J} \\ \vec{q} \end{pmatrix} = \begin{pmatrix} \hat{\sigma} & \hat{\alpha} \\ T\hat{\alpha} & \hat{\bar{\kappa}} \end{pmatrix} \begin{pmatrix} \vec{E} \\ -\vec{\nabla}T \end{pmatrix} \tag{8.1}$$

For systems with two spatial dimensions (x, y) and a perpendicular magnetic field, the transport coefficient are 2×2 matrices relating the local charge and heat current ($\vec{J}$ and $\vec{q}$, respectively) to the local electric field ($\vec{E}$) and temperature gradient ($\vec{\nabla}T$). The electrical conductivity, defined as the response of the charge current to an electric field with no thermal gradient, is simply given by

†The linear diffusive regime assumes cooling is dominated by Wiedemann-Franz like diffusion, the electrical conduction is sufficiently diffusive (not ballistic), and the temperature rise is small compared to the absolute temperature scale.

$\hat{\sigma}$. However, the thermal conductivity ($\hat{\kappa}$) is not symmetrically defined as the response of heat current to an applied temperature gradient in the absence of an electric field but instead defined in the absence of a charge current. Thus,

$$\hat{\kappa} \equiv \hat{\bar{\kappa}} - T\hat{\alpha}\hat{\sigma}^{-1}\hat{\alpha} \tag{8.2}$$

The form of the transport coefficients are constrained by a number of symmetries: The off diagonal elements of Eqn. 8.1 are related due to Onsager reciprocity[†] [150, 151] and rotational symmetry requires all coefficients be antisymmetric — i.e all coefficients can be written in the form:

$$\hat{\sigma} = \begin{pmatrix} \sigma_{xx} & \sigma_{xy} \\ -\sigma_{xy} & \sigma_{xx} \end{pmatrix} \tag{8.3}$$

For a degenerate Fermi liquid, it has been shown theoretically [151] and experimentally [152] that the thermal-electric coefficient $\hat{\alpha}$ is related to the electrical conductivity $\hat{\sigma}$, component by component, via the generalized Mott formula:

$$\hat{\alpha} = e\mathcal{L}_0 T \frac{\mathrm{d}\hat{\sigma}}{\mathrm{d}\mu} \tag{8.4}$$

where μ is the chemical potential and $\mathcal{L}_0 = \frac{1}{3}(\pi k_B/e)^2$ is the Sommerfeld value of the Lorenz number [26]. However, in clean graphene samples inter-particle scattering breaks the assumptions used to derive Eqn. 8.4 and violations of the Mott relation have been measured [142]. While a simi-

[†]Let $\hat{\alpha}$ and $\hat{\bar{\alpha}}$ be the two offdiagonal terms of eqn. 8.1. Time reversal symmetry and thus Onsager reciprocity demand $\alpha_{ij}(B) = \bar{\alpha}ji(-B)$. But rotational symmetry forces α to be antisymmetric and thus $\alpha_{ij}(B) = -\bar{\alpha}ij(-B) = \bar{\alpha}ij(B)$. Where the last step was done by rotating π along an in plane axis.

lar theoretical treatment [151] has shown the validity of the generalized Wiedemann-Franz law

$$\hat{\kappa} = \mathcal{L}_0 T \hat{\sigma}, \tag{8.5}$$

several detailed calculations have predicted violations in graphene near landau quantization [153, 154, 155] and several more in the hydrodynamic regime [74, 60].

8.2 Classical Hall Effect

In low magnetic field or high carrier density, such that landau quantization does not significantly modify the density of states, the tensorial form of $\hat{\sigma}$ can be calculated under the assumptions of the classical Hall effect yielding:

$$\begin{aligned} \sigma_{xx} &= \sigma_0 \frac{1}{1 + \tan^2(\theta_H)} \\ \sigma_{xy} &= \sigma_0 \frac{\tan(\theta_H)}{1 + \tan^2(\theta_H)} \end{aligned} \tag{8.6}$$

where

$$\tan(\theta_H) = -\frac{\sigma_0}{e} \frac{B}{n}, \tag{8.7}$$

σ_0 is the zero field conductivity, n is the charge density, and B is the perpendicular magnetic field strength.

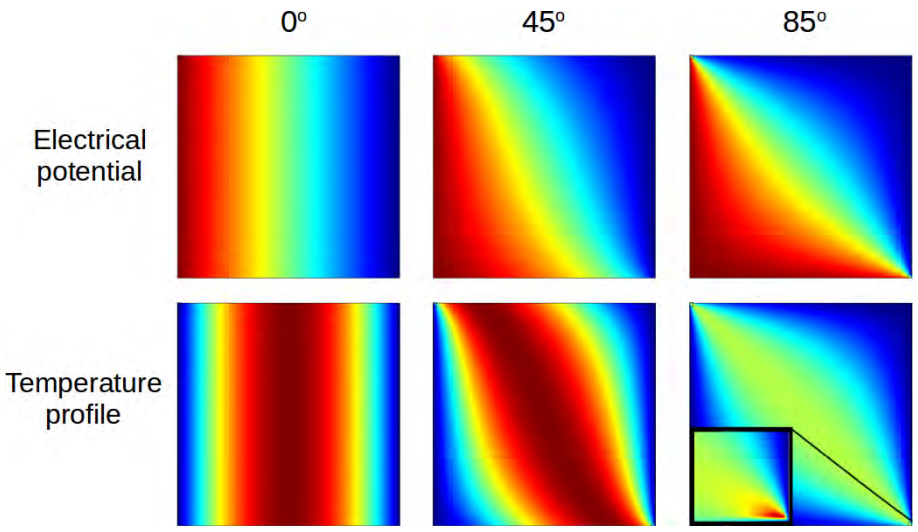

Figure 8.1: Normalized voltage (**upper**) and temperature (**lower**) profiles resulting from Joule heating a uniform, square conductor in the classical Hall regime for Hall angles 0° (**left**), 45° (**center**), and 85° (**right**). The left and right sides of each profile correspond to electrical terminals with the the boundary conditions of constant voltage and temperature. For $\theta_h = 0^\circ$ current flows uniformily from left to right and the temperature profile is parabolic as discussed in section 4.1. As the Hall angle is increased, the current bends and the location of the peak temperature moves closer to the contacts. Near 90°, all of the dissipation occurs at the contacts resulting in the formation of hot spots. All plots are from finite element simulations [156]

As the field strength increases, the changing conductivity tensor results in a changing current distribution, which, in turn, results in a changing Joule heating profile and steady state temperature distribution. Finite element simulations [156] illustrate how a magnetic field can affect the temperature and current profiles of a uniform, two-terminal conductor with the anisotropic $\hat{\sigma}$ and $\hat{\kappa}$ given by Eqn. 8.6 and Eqn. 8.5, as shown in Fig. 8.1. Boundary conditions are chosen to match a typical experiment where macroscopic electrical contacts serve as a thermal bath. In the absence of an external magnetic field, the current is uniform producing a parabolic temperature profile as discussed in section 4.1. However, this simple calculation breaks down at finite field where current begins to bend, resulting in an anisotropic temperature profile. At large magnetic fields, where the Hall angle approaches 90°, nearly all the dissipation occurs at two points near the contacts resulting in the formation of hot spots. For a fixed Joule heating power, the spatial mean temperature of the sample goes to zero as Hall angle is increased and the hot spot size approaches a singularity; the power of Johnson noise measurements is that the measured Johnson noise temperature (section 2.2), T_{JN}, naturally weights regions of higher local dissipation more such that as the dissipation approaches a singularity, so too does the spatial weighting function for T_{JN} — i.e. Johnson noise is sensitive to the temperature of the hot spots.

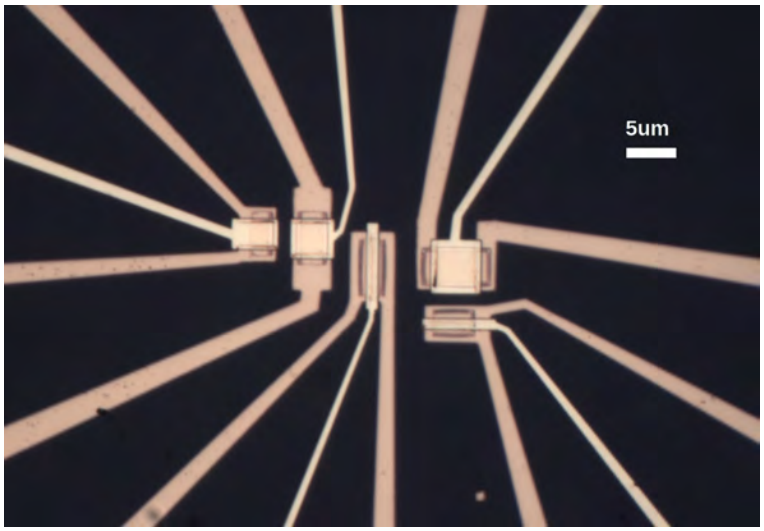

Figure 8.2: Microscope image of the graphene device used in this chapter. Multiple devices of various geometries are made from the same hBN-graphene-hBN stack on an insulating sapphire substrate. The two-terminal device used in this chapter is the second from the left and has a dimension of $4\ \mu m \times 4\ \mu m$. A lithographically defined local top gate is used to control carrier density.

8.3 Graphene characteristics

Monolayer graphene is mechanically exfoliated, encapsulted with hexagonal boron nitride (hBN), and contacted along its one dimensional edge [50] to form a square, two-terminal device ($4\ \mu m \times 4\ \mu m$). These dimensions are chosen as a balance between the requirements that the device be longer than the electronic mean free path yet short enough that Wiedemann-Franz cooling dominates over electron-phonon cooling, as discussed in chapter 4. Samples are fabricated on insulating sapphire substrates with a local top gate to electrostatically control carrier density as shown in Fig. 8.2. The gate capacitance is measured using the integer quantum Hall effect. The low temperature, two-terminal resistance varies between 0.2 and $4.3\ k\Omega$ by varying the top gate $\pm 5\ V$,

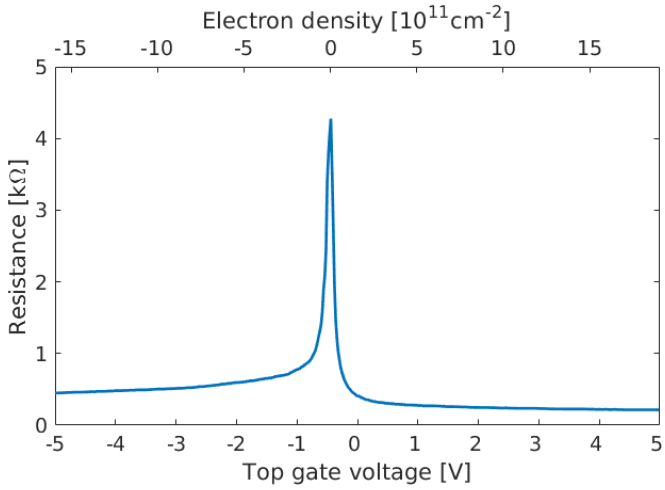

Figure 8.3: DC resistance of the graphene device at zero magnetic field as a function of carrier density controlled via an electrostatic top gate. Gate capacitance is measured using the integer quantum Hal effect.

corresponding to a carrier density of $\sim \pm 1.6 \times 10^{12} cm^{-2}$, as shown in Fig. 8.3. The conductivity minimum is attained for a top gate voltage $V_g = -430\, mV$ corresponding to an intrinsic electron doping of $1.4 \times 10^{11} cm^{-2}$. The FWHM of the resistance is $5 \times 10^{10} cm^{-2}$ with a minimum carrier density of $n_{min} \approx 1.2 \times 10^{10} cm^{-2}$, where n_{min} is defined in accordance with chapter 6.

The sample is cooled to $1.7\ K$ by a variable temperature, ^{4}He vapor cryostat (Appendix A.2 equipped with a $14\ T$ superconducting magnet. The DC two-terminal resistance is measured up to $13\ T$ and shown in Fig. 8.4. Integer quantum Hall states are present at fields as low as $0.5\ T$ and the $\nu = 1$ symmetry broken state appears at high field. By analyzing the resistance values of the quantum Hall plateaus, the contact resistance is estimated to vary between 50 and $170\ \Omega$ as a function of density at $1.7\ K$. Low contact resistance is vital to Johnson noise thermometry as any dissipation that occurs outside of the sample will lead to unwanted Johnson noise which can de-

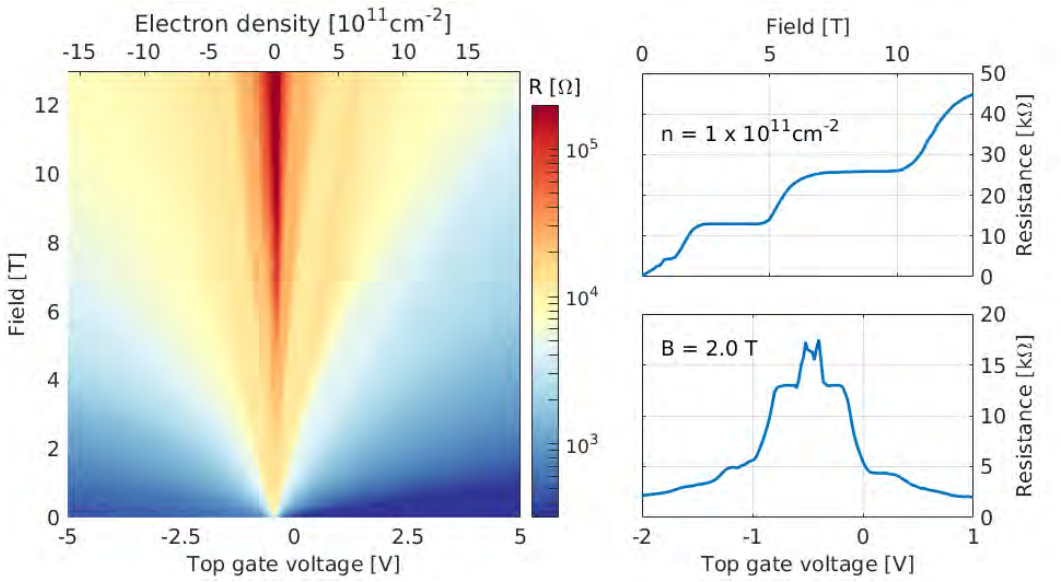

Figure 8.4: Two-terminal DC resistance of a monolayer graphene device at $1.7\ K$. (**left**) Resistance is shown on a log scale as a function of carrier density and perpendicular magnetic field strength. (**top right**) and (**bottom right**) show cuts at constant density and field, respectively.

grade the measurement. Using these estimates for the contact resistance, we can estimate the zero field conductivity and thus the Drude mobility and elastic mean free path which vary between $0.2 - 2 \times 10^5\ cm^2/Vs$ and $200 - 650\ nm$, respectively, as a function of density, as shown in Fig. 8.5.

8.4 Electrical noise in high fields

Varying by over two orders of magnitude, the DC resistance of the graphene device must be impedance matched using a wide dynamic range matching network. As described in detail in section 2.6, an on chip, two-stage LC tank circuit in a low-pass configuration is used to transform the

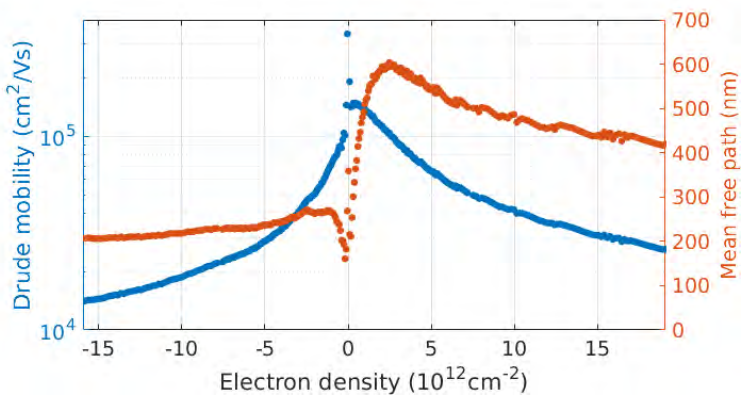

Figure 8.5: Estimated Drude mobility and elastic mean free path of the graphene device used in this chapter as a function of electron density at $1.7\ K$. Estimates are made from the two-terminal conductance at zero magnetic field assuming a contact resistance estimated from the resistance of the integer quantum Hall plateaus. The Drude estimation breaks down near the charge neutrality point where the carrier density is not simply given by the charge density divided by the electron charge

sample impedance to near $50\ \Omega$. To meet the strict requirements of multi-stage matching, the device was built on an insulating sapphire substrate and surface mount inductors and capacitors were directly soldered to a coplanar waveguide. All inductive elements were air-core as to be magnetic field insensitive and used gold leads which facilitated the direct connection of the graphene sample via wirebond, as shown in Fig. 8.6.

A vector network analyzer (VNA) can be used to test the high frequency coupling to the device. As the sample resistance changes, different regions of the noise spectra are efficiently coupled into the measurement circuit, as shown in Fig. 8.7. At a DC resistance of $1\ k\Omega$ the noise bandwidth of the matching network is $\sim 150\ MHz$ and $>3\ dB$ coupling continues for resistances above $100\ k\Omega$. Quantifying the coupling in terms of a noise measurement for a circuit as detailed in section 2.4, we

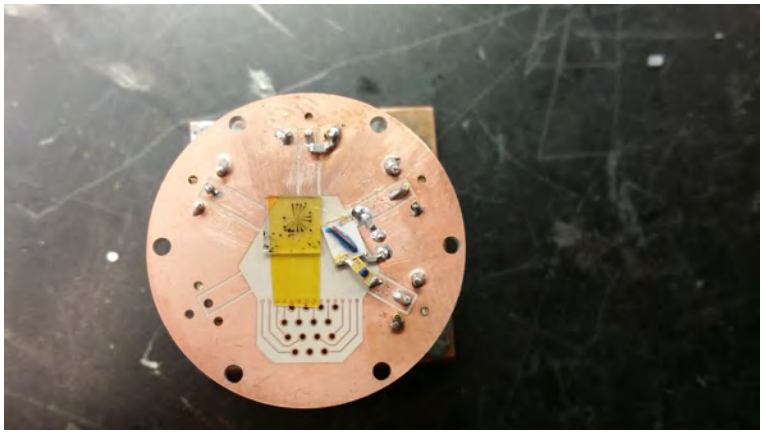

Figure 8.6: Custom sample package used to measure graphene thermal conductance in high magnetic fields. The graphene device is placed on an insulating sapphire substrate which is mounted to the sample package using double-sided Kapton tape. The sample is then wire bonded directly to an air-core surface mount inductor which is part of a two-stage LC tank circuit used to impedance match the high resistance device. The output of the network is soldered directly to a coplanar waveguide which terminates in a high frequency SMP connector. An RF shield then encloses the the device which can be loaded into a cryostat.

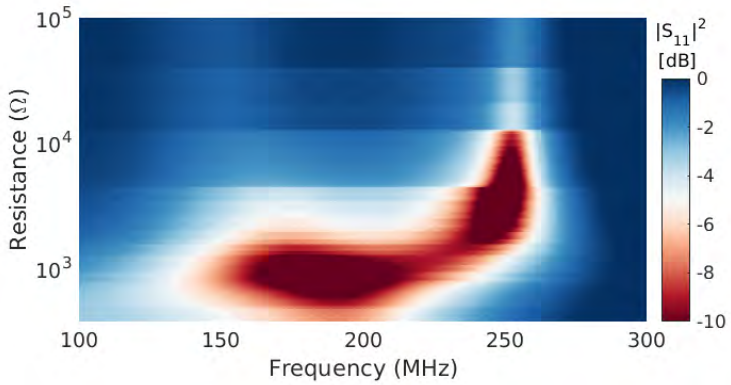

Figure 8.7: Reflection coefficient as a function of frequency and graphene DC resistance. The two-stage LC matching circuit is designed to couple a wide dynamic range of resistances allowing the continual measurement of graphene from zero magnetic field to quantum Hall states. When optimally matched at $R \approx 1k\Omega$, the circuit has a noise bandwidth of $\sim 150\, MHz$. As detailed in section 2.6, the high frequency solution of the two-stage network is intentionally moved to a higher resistance creating a wider dynamic range.

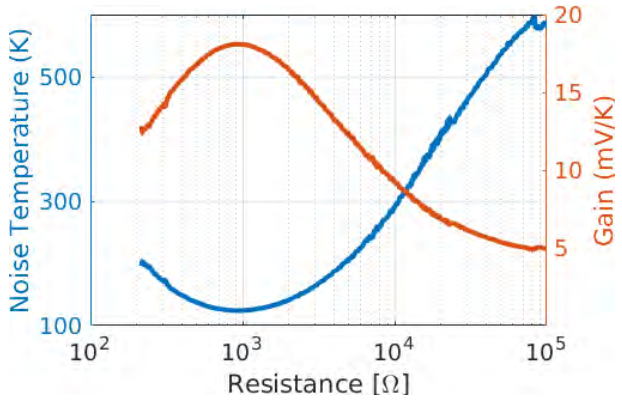

Figure 8.8: Generalize gain and noise temperature, as defined in section 2.7 and Eqn. 8.8, for the graphene device and matching network shown above. Gain is maximize, and noise temperature is minimized when the device is optimally matched at $1\ k\Omega$. This data is collected by varying the carrier density of graphene at three different magnetic field values, $0, 1$, and $13\ T$. All data collapses onto the same line indicating the matching circuit is field insensitive and depends only upon the graphene DC resistance.

can write the measured output voltage as

$$V_{out} = \mathcal{G}(\Gamma)(T + T_n(\Gamma)). \tag{8.8}$$

Calibration as outlined in section 2.8 yields $\mathcal{G}(\Gamma)$ and $T_n(\Gamma)$ which are plotted as a function of the DC resistance in Fig. 8.8. We find the calibration parameters to depend only upon the graphene DC resistance and not upon temperature or magnetic field, indicating the matching network is stable over the parameter range of our measurement. With the device matched and the circuit calibrated, we can measure the total output noise from the sample (Fig. 8.9). During the course of an experiment it is common for the background noise T_n to fluctuate on a long time scale (e.g. hours); thus to reach the desired sensitivity it is necessary to perform differential measurements, as described in chapter 4, by sinusoidally varying the a Joule heating current and measuring the cosinusoidal elec-

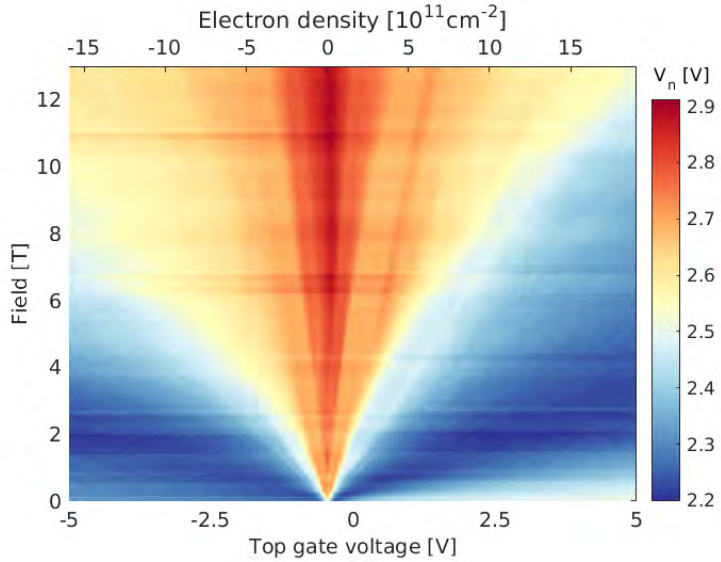

Figure 8.9: DC voltage proportional to the total noise emitted into the measurement bandwidth, as defined by Eqn. 8.8, from a graphene device as a function of carrier density and magnetic field at $1.7\,K$. Horizontal streaks appear in the data as the system noise temperature fluctuates over the course of the experiment illustrating the need for the differential measurements performed in section 8.5.

tronic temperature rise with a lock-in amplifier.

8.5 Magneto-thermal conductance

While injecting heat into the electronic system, the steady state temperature rise provides information on how efficiently the system transports thermal energy to the bath. Applying the methodology of chapter 4, a differential heating current applies a peak power of P_0 to the graphene device and the peak-to-peak differential Johnson noise temperature ΔT_{JN} is measured[†]. When

[†]Calibration of these differential measurements only requires the use of generalized gain, $\mathcal{G}$. Any fluctuations in the background noise are averaged out and T_n is only important in that it determines how long you must average to reach the desired precision.

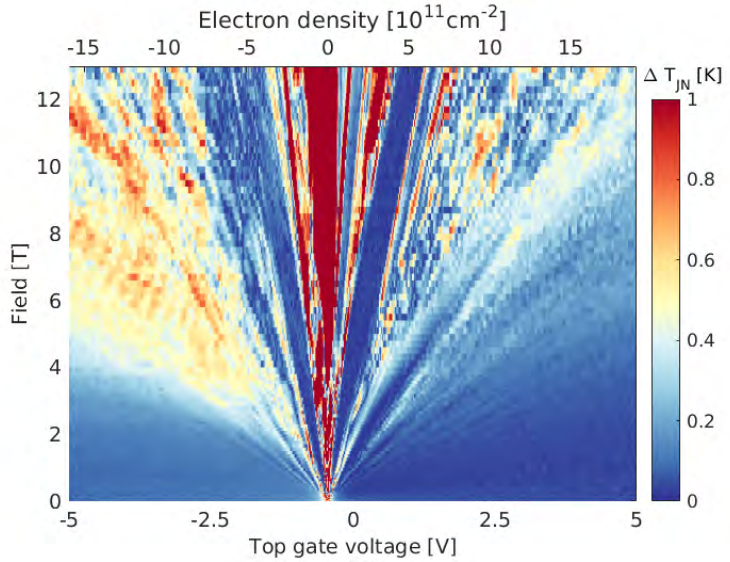

Figure 8.10: Differential Johnson noise temperature rise of a graphene device in response to a differential heating power of $0.4\,nW$ as a function of carrier density and magnetic field at $T_b = 1.7\,K$. At low field and high density, the electronic thermal conductivity is high in accordance with the Wiedemann-Franz law resulting in a small temperature rise. As the field increases, so too does the electrical resistance and thus the thermal resistance and the steady state temperature rise. However, the appearance of quantum effects results in a drastic reduction of ΔT_{JN} due to the ballistic nature of the conduction channel.

the device's thermal conductance is large, ΔT_{JN} is reduced, while an enhancement of ΔT_{JN} signifies a reduction of the thermal conductance. Fig. 8.10 shows the differential (quasi-steady state) electronic temperature rise of a square, two-terminal graphene device (described in section 8.3) for a heating power $P_0 = 0.4\,n$W. Much of the qualitative heating behavior can be understood via the Wiedemann-Franz law; at low field and high density ΔT_{JN} is found to be small, as the electrical conductivity (and therefore the thermal conductivity) is large, while at higher fields, ΔT_{JN} is larger due to magnetoresistance affecting the thermal conductivity. At lower density, we find quantum oscillation in the thermal signal and a drastic reduction of ΔT_{JN} in quantum Hall states.

To analyze this quantitatively, we can define a thermal resistance (R_{th}) as the inverse of the ther-

mal conductance defined in chapter 4,

$$R_{th} \equiv \frac{\Delta T_{JN}}{P_0} \tag{8.9}$$

Its important to note that R_{th} is not the traditional thermal resistance, which describes the total heat current flowing through a material in response to a spatial temperature gradient; it is instead a generalized thermal resistance describing the heat power transferred between the electronic system and the bath under Joule heating. For a diffusive system[†] dominated by Wiedemann-Franz electronic cooling, the thermal resistance in the linear response regime is given by:

$$R_{th} = \frac{R}{12\mathcal{L}\,T_b} \tag{8.10}$$

where $\mathcal{L}$ is the Lorenz ratio and T_b is the bath temperature. Eqn. 8.10 is derived in section 4.3 and holds under the following assumptions:

1. Heat conduction is provided entirely by electron diffusion of the form $\hat{\kappa} \propto \hat{\sigma}$, where the constant of proportionality is defined as $\mathcal{L}T_b$ by convention
2. The transport coefficients are spatially uniform
3. The device has only two electrical terminals which serve as thermal reservoirs and sources of Joule heating current
4. The elastic mean free path of the charge carriers is shorter than all other relevant length scales in the system

[†]Here a diffusive system is defined as one where the elastic mean free path of charge carriers is smaller than all other relevant length scales in the problem

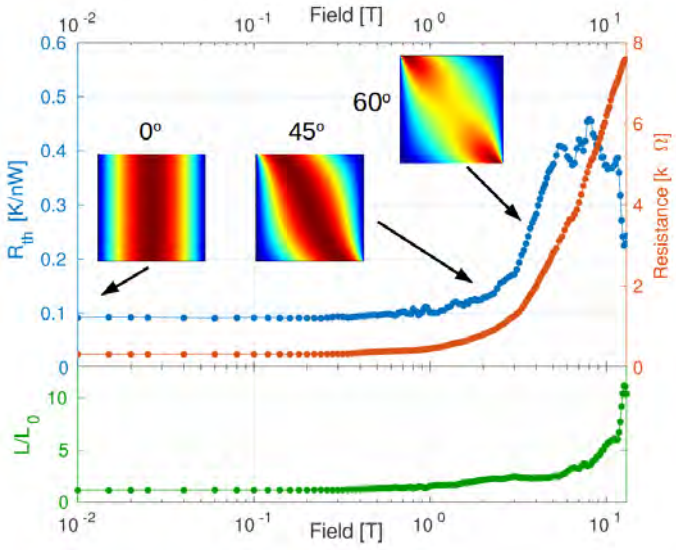

Figure 8.11: (**upper**) Comparison of the thermal resistance $R_{th} \equiv \Delta T_{JN}/P_0$ (blue) and the electrical resistance R (red) for monolayer graphene hole doped away from the charge neutrality point ($n \approx -1.6 \times 10^{12} cm^{-2}$). (**Insets**) show the expected classical Hall temperature profiles for select Hall angles from finite element simulation [156] under the assumption of the WFL. (**lower**) The measured Lorenz ratio $\mathcal{L} \equiv (R/R_{th})(1/12T_b)$ normalized to the Sommerfeld value. For magnetic fields below a few Tesla, R_{th} tracks R, but at high field, the behavior of R_{th} deviates sharply from that of R.

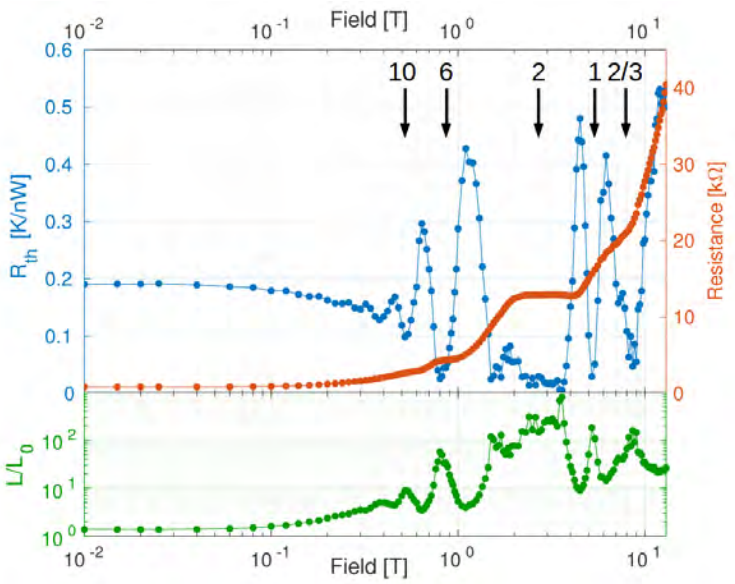

Figure 8.12: (**upper**) Comparison of the thermal resistance $R_{th} \equiv \Delta T_{JN}/P_0$ (blue) and the electrical resistance R (red) for monolayer graphene with a carrier (hole) density of $n \approx -1.2 \times 10^{11} cm^{-2}$. At low field, R increases while R_{th} decreases with quantum oscillations appearing in the thermal data around $0.3\,T$. In the $\nu = 2$ quantum Hall state, the electrical data shown a plateau at the expected $\frac{1}{2}h/e^2$ while the thermal resistance drops close to zero. At the magnetic field strength corresponding to other filling fractions, $\nu = 10, 6, 1$, and $2/3$, the thermal signal shows a similar drop toward zero even though the electrical plateaus are not present. (**lower**) The measured Lorenz ratio $\mathcal{L} \equiv (R/R_{th})(1/12T_b)$ normalized to the Sommerfeld value.

Fig. 8.11 compares R and R_{th} for graphene with a large carrier density ($n \approx -1.6 \times 10^{12} cm^{-2}$) as a function of magnetic field strength at $10\,K$. For fields up to a few Tesla, we find that, while R_{th} qualitatively tracks the field dependence of R, the measured Lorenz ratio, $\mathcal{L} \equiv \frac{1}{12\,T_b}(R/R_{th})$, has a small field dependence, even in the so-called "classical" regime, in stark contrast to the predictions of Eqns. 8.10 and 8.5. In high field, where landau quantization becomes relevant, the behavior of R_{th} begins to significantly deviate from that of R, eventually decreasing with field and tending towards zero. At low density this behavior is even more pronounced as quantum effects enter as low as $0.5\,T$. Fig. 8.12 shows similar measurements to Fig. 8.11 for a lower carrier density of

$n \approx -1.2 \times 10^{11} cm^{-2}$. Unlike the high density data shown in Fig. 8.11, at low density, R_{th} decreases with magnetic field for low fields even though R increases. For all densities $\mathcal{L}$ monotonically increases with field until quantum oscillations are seen. At fields and densities where the electrical data shows well developed plateaus, the thermal signal drops to near zero and the measured $\mathcal{L}$ diverges as a result of the ballistic nature of quantum Hall states. In fact, this combination of Johnson noise thermometry and Joule heating is particularly suited to the detection of quantum modulations of the density of states; this is readily seen in Fig.8.12 where, although not fully developed electrically, the thermal signal shows several more integer states, including the symmetry broken state $\nu = 1$, and the fractional state $\nu = 2/3$. The sensitivity of this technique to quantum effects results from its intimate connection to changes in entropy and carrier thermalization length. Fig. 8.13 shows the entire thermal fan diagram at $T_b = 1.7\ K$.

8.6 Cyclotron radius

Given the apparent violation of Eqn. 8.10 at finite magnetic field, it stands to reason that one of the four assumptions listed above must be violated in graphene. The most obvious of which is the assumption that the elastic mean free path is shorter than all other relevant length scales. In the presence of a magnetic field, electrons in two-dimensional conductors travel along cyclotron orbits of radius

$$r_c = \frac{m^* v_F}{e\,B} \tag{8.11}$$

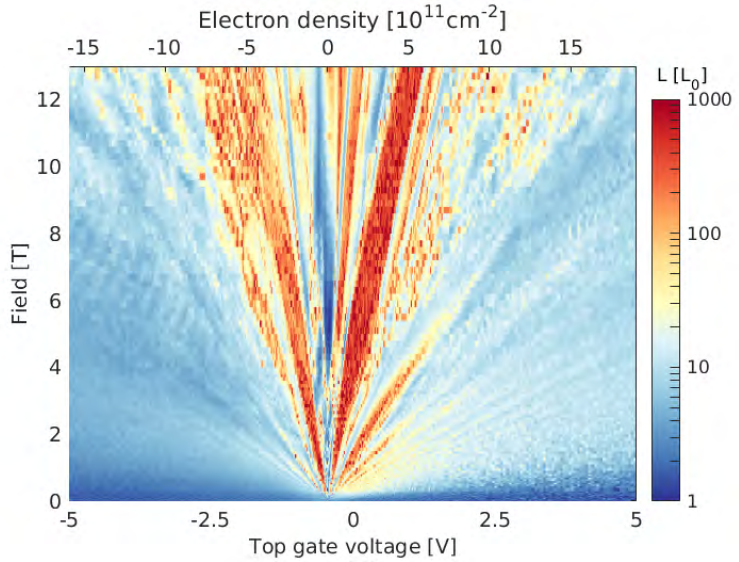

Figure 8.13: The measured Lorenz ratio $\mathcal{L} \equiv (R/R_{th})(1/12T_b)$ of a square graphene device normalized to the Sommerfeld value as a function of carrier density and magnetic field at $T_b = 1.7\,K$. Color axis shown on a log scale. Quantum Hall states appear as lines of large Lorenz number

where v_F is the Fermi velocity and m^* is dynamical mass of the charge carrier. Unlike traditional conductors with parabolic dispersions, the dynamical mass graphene is a function of the Fermi energy (E_F) and given by the relativistic form

$$m^* = E_F/v_F^2 \tag{8.12}$$

$$= \hbar\sqrt{\pi n}/v_F \tag{8.13}$$

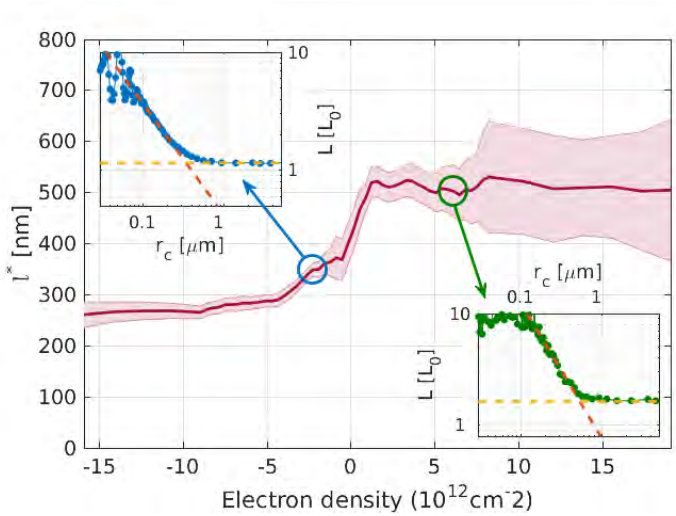

Figure 8.14: Characteristic cyclotron radius $l^*(n)$ at which $\mathcal{L}$ begins to deviate from $\mathcal{L}_0$. Large cyclotron radius corresponds to small magnetic field. (**insets**) plot two representative examples of how l^* is extracted; a linear fit to the log of $\mathcal{L}$ vs cyclotron radius (r_c) is extrapolate to the constant, low field value $\mathcal{L}(B \approx 0)$. Red shaded region represents 50% convince intervals of the fits. These values can be directly compared to the quasiparticle elastic mean free path estimated by the zero field conductance in Fig. 8.5.

thus the cyclotron radius can be written as a function of carrier density and magnetic field, as:

$$r_c = \frac{\hbar\sqrt{\pi n}}{e\,B} \tag{8.14}$$

$$= l_B^2\sqrt{\pi n} \tag{8.15}$$

where $l_B = \sqrt{\hbar/eB}$ is the magnetic length.

As we increase magnetic field for a fixed carrier density, we can quantitatively define a characteristic cyclotron radius (l^*) at which $\mathcal{L}$ begins to deviate from $/sL_0$ by extrapolating a linear fit of the log of $\mathcal{L}(r_c)$ to the constant low field value $\mathcal{L}(B \approx 0)$. The insets of Fig. 8.14 show two representative examples of this procedure. $l^*(n)$ is the relevant magnetic length at which we see violations

of eqn. 8.10 for a given density. The main panel of Fig. 8.14 plots l^* as a function of electron density. The values found should be quantitatively compared to the elastic mean free path of the charge carriers which is estimated from the zero field conductance in Fig. 8.5. Essentially, the mean free path imposes a length cutoff for variations of the local temperature — i.e the temperature cannot equilibrate at scales shorter than the mean-free path, since over these length scales electrons move ballistically. The strong agreement between the data in Figs. 8.14 and 8.5 (rms normalized error of 23%) is evidence that the deviations of $\mathcal{L}$ from $\mathcal{L}_0$ are due to relevant dynamics occurring on a length scale where electrons are ballistic. This is taken to an extreme in the limit of quantum Hall where conduction occurs only on ballistic edge channels and hence the measured Lorenz ratio diverges.

A

RF cryostats

All experiments reported in this thesis were performed in one of three cryostats, each wired for high frequency measurements. A custom sample mounting board was machined from copper laminated PTFE (Rogers Corp, RT/duroid®), as shown in Fig. A.1. Five coplanar waveguides, with characteristic impedance 50 Ω, are milled into the circuit board along with 14 DC lines and a DC

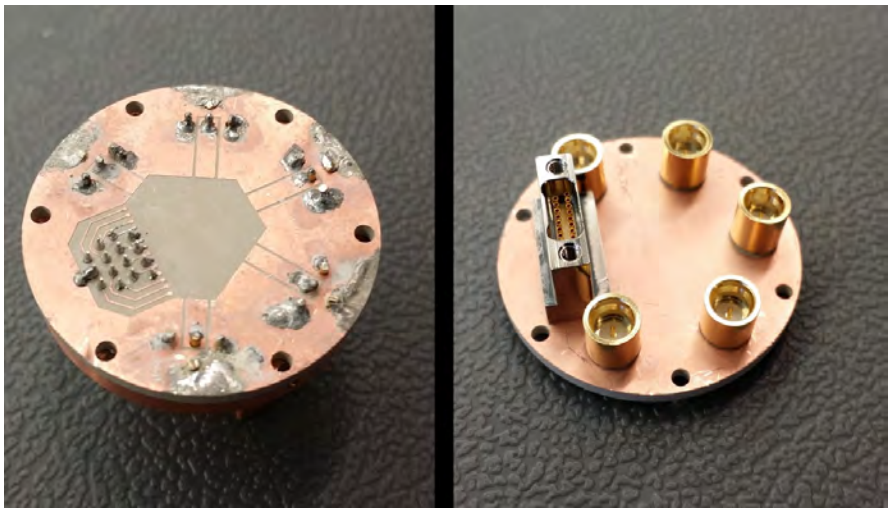

Figure A.1: Images of the circuit board used to mount samples. (**Left**) sample is placed in the copper free area in the center of the board. Five coplanar waveguides are milled along the outer ring. 14 DC lines with bonding pads and a DC ground are machined on one end. (**Right**) the backside of the circuit board where each RF waveguide is soldered to an SMP connector and all DC lines are soldered to the pins on a "NanoD" connector.

ground. Each RF waveguide ends in a through board SMP male connector while all DC lines and the DC ground connect to a through board "NanoD" connector. The entire circular board measures 1 inch in diameter allowing it to lowered into the small bore of a superconducting magnet.

The sample and SMD inductors/capacitors are fixed to the board using double sided Kapton tape and all componets are wired together using either solder or direct wirebonding. Fig. A.2 shows an example of a double-stage match network connected using only wirebonds. In practice, aluminum wire bonds have difficulty bonding to the soft pads of the SMD capacitors and so often solder is used for these parts. Once connected, the sample is sealed in an RF tight copper box which can loading into any of the three cryostats described below.

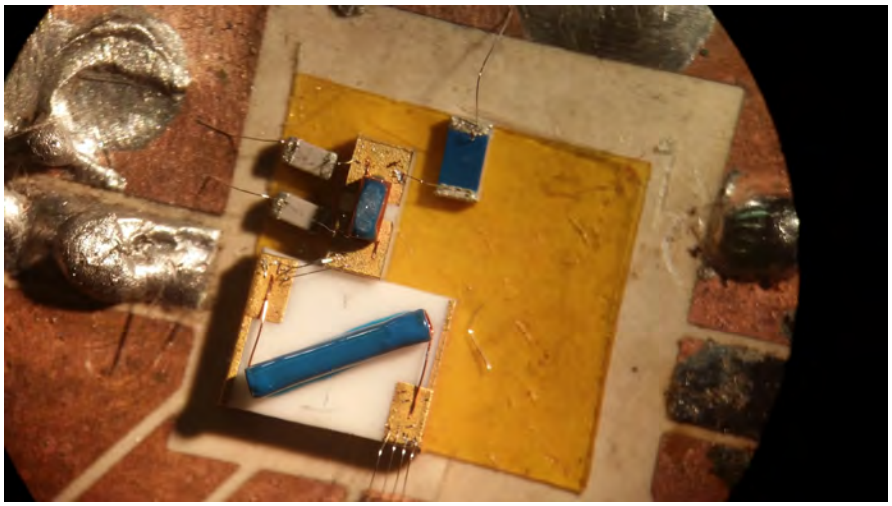

Figure A.2: Example of components mounted on our circuit board. In this case, 2 inductors (blue elements with gold leads), 2 capacitors (grey elements with silver leads), and one resistor (blue element with silver leads) forming a two-stage LC matching network. Components are secured using double-sided Kapton tape and connected using aluminum wirebonds.

A.1 Janis

The experiments discussed in chapters 5 and 6 were performed in one of two ^{4}He closed cycle Janis SHI-4 cryocoolers located at Raytheon BBN Technologies and Harvard University. The Harvard system is shown in Fig A.3 and operates with the sample in vacuum over a continuous temperature range of $2.8 - 320\ K$. Custom copper thermalization plates were machined to thermally anchor SMA bulkheads at $50\ K$ and base temperature. Solid, semi-rigid coaxial cables with copper inner and outer conductors are run through the system. Often low-pass filters are placed at the $50\ K$ stage to help reflect high frequency thermal noise from room temperature. A heater and thermometer are mounted on the sample stage to control and measure the bath temperature using a

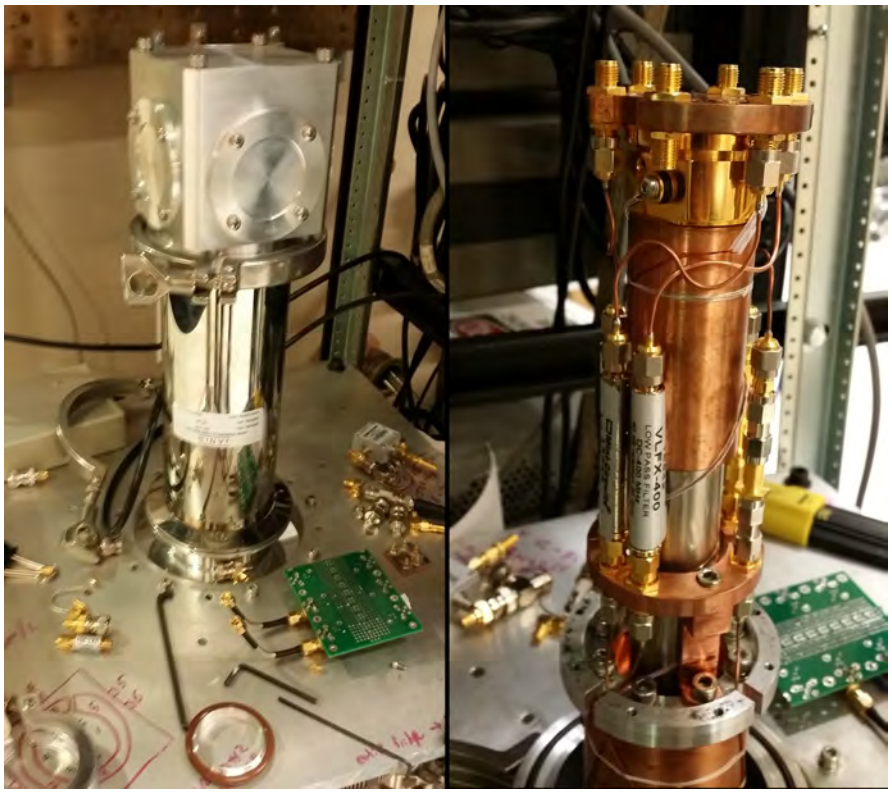

Figure A.3: Janis SHI-4 cryocoolor used in parts of this dissertation. (**Left**) image of the closed system sealed and under vacuum. Optical windows are available but are blocked for these experiments. (**Right**) image of the opened system exposing the RF semi-rigid coax cables. The sample package is mounted onto the top plate which is cooled via a closed cycle ^{4}He system and the temperature is set using a heater, thermometer, and Lakeshore PID controller. Low-pass filters are placed at the mid temperature plate to reflect room temperature noise.

Lakeshore PID controller. The sample package described above is mounted on a pedestal and bolted directly onto the base plate. For experiments that do not require ultra-low temperatures or magnetic fields, this system is my personal favorite as its versatile, reliable, and easy to maintain.

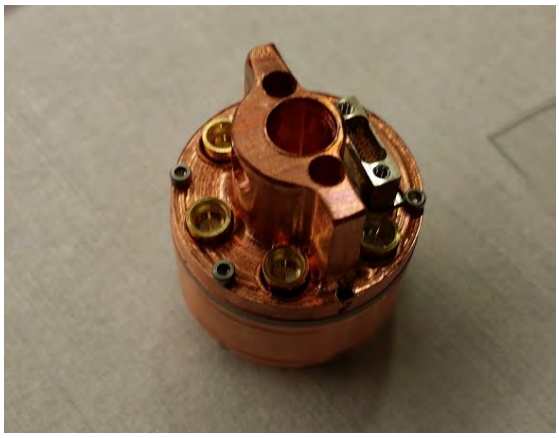

Figure A.4: Sample package mounted to the custom adapter made for the Oxford cryostat. Adapter has two machined holes to house a heater and thermometer. Entire package is then affixed to the end of a long SS thin-walled tube and lowed into the Oxford VTI.

A.2 Oxford

The Oxford brand cryostat, used for the bulk of chapter 8, is a wet ^{4}He system with a variable temperature insert (VTI) capable of operating from $1.7 - 300\ K$. It houses a $14\ T$ superconducting magnet with a relatively small $\sim$1.1 inch bore. The sample is inserted into the VTI and cooled via cold ^{4}He vapor which is held at a fixed temperature by a heater and thermometer located at the vapor inlet and controlled by a Lakeshore PID controller.

The sample package described above is attached via non-magnetic SS screws to a custom copper adapter, as shown in Fig. A.4. This custom adapter was machined to house a Cernox® thermometer (Lakeshore AA package) and resistive cartridge heater. The entire package can then be affixed onto the end of a long SS thin-walled tube and held in place by a set screw, as shown in Fig. A.5. A cop-

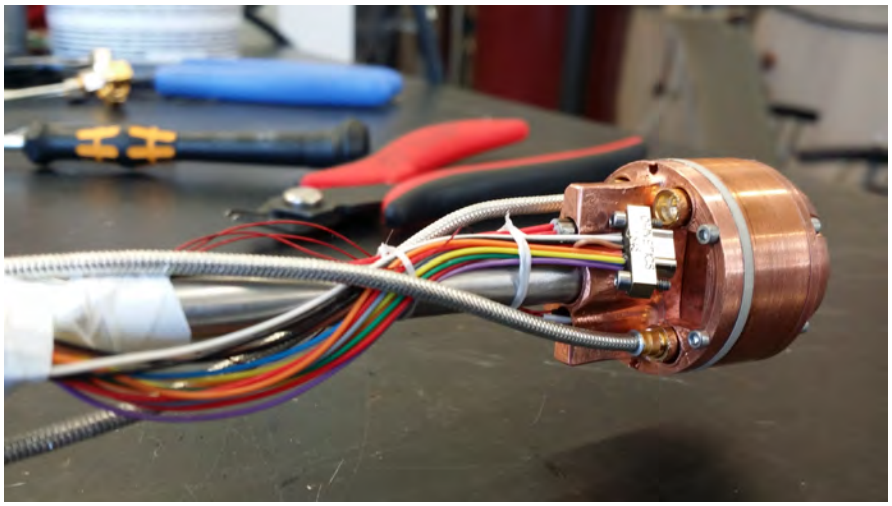

Figure A.5: The business end of the custom made RF measurement probe for the Oxford VTI. The sample package is affixed to a SS tube using a set screw. RF coaxial measurement lines connect the on-board SMP connectors to the room temperature SMA bulkhead feedthroughs. DC connections are made via a nanoD connector (the nanoD plug is removed in this image as DC lines were not needed in this experiment).

per plate in affixed to the tube about 1 foot above the sample package and contains space for up to 6 SMA bulk head connectors. Five semi-rigid coax are run from room temperature SMA bulkhead feedthroughs to this mid-temperature copper plate; two of these coax have copper inner and outer conductors and are used for noise measurements while the rest are an alloy of Copper and Nickel (to reduce the thermal conductance to the sample) and are used as excitation lines and/or gate control lines. Low-pass filters are often placed on the mid-temperature plate to reflect high frequency noise from room temperature. The heater and thermometer lines are connected to a DC military feedthrough and the nanoD is connected to a Fisher feedthrough.

As shown in Fig. A.6, once the sample is installed into sample package and mounted onto the RF probe, the entire unit can be lowered into the Oxford VTI. RF amplifiers can be placed either at low temperature or at room temperature just outside the fridge. For all experiments in this dissertation,

Figure A.6: Image of the Oxford cryostat with VTI and RF probe during a measurement. All electronics are kept at room temperature. The entire fridge is housed inside a shielded metal room.

all electronics were kept outside the fridge at room temperature.

A.3 Leiden

For ultra-low temperature experiments, a dry dilution refrigerator from Leiden cryogenics was used, as shown in Fig. A.7. This entirely closed cycle system has a base temperature of $\sim 10\ mK$ and a large bore ($\sim$6 inches) magnet with a maximum field strength of $5\ T$. To facilitate fast experiment turn around times, it is equipped with a top loading probe which can bring a sample down to base temperature in a few hours. To access the cold plates for maintenance or install a longer term experimental setup, the fridge vacuum shields can be removed with the help of 4 electrically controlled, mechanical legs, as shown in Fig. A.8.

Inside, the system consists of two independent vacuum chambers and five large gold plated copper plates thermally isolated from each other. The first and second plates are cooled by an electrically isolated pulse tube and, during operation, typically run at $50\ K$ and $4 - 5\ K$, respectively. The outer vacuum chamber (OVC) contains the entire $50\ K$ plate and the upper half of the $4\ K$ plate along with two sorption pumps and two heaters. The bottom half of the $4\ K$ plate forms the top of the inner vacuum chamber (IVC) which is sealed with a Kapton o-ring. Four large SS tubes connect into the IVC to allow probes to enter; the central port is used for the main probe (described below), one of the secondary ports is used to bring in 16 RF coaxial cables, and the other two are held in reserve for future expansions. The bottom half of the $4\ K$ plate also contains 2 sorption pumps

Figure A.7: Image of the closed cycle dilution refrigerator made by Leiden cryogenics installed in the Kim lab. The insertable, top-loading probe is seen in the upper half of the image enclosed in flexible bellows. The system sits on four electrically controlled, mechanical legs to lift the system for easy maintenance.

Figure A.8: Image of the Leiden cryostat being disassembled. The four electrically controlled legs are extended, lifting the entire system for easy maintenance.

which pump out the IVC and can be heated (via internal heaters) to release exchange gas into the IVC. The third plate contains the still/impedances and typically operates at a temperature of around $0.8\ K$. The still has an on-board heater allowing the He mixture evaporation rate to be controlled[†]. The $5\ T$ magnet is bolted onto the still plate and thus operates at the still temperature, as shown in Fig. A.9. While running the magnet it is therefore import to watch the still temperature. The fourth plate has no direct cooling mechanism but serves as both a radiation shield and a location to mount the heat exchangers for the dilution circuit; during operation is typically sits around $100\ mK$. The fifth and final plate contains the dilution mixing chamber and includes a long tail that dips into the magnet bore. Fig A.10 shown a close up of the entire IVC (lower 4 plates).

To perform RF measurements, one of two options is available: firstly, if the number of cold microwave elements is small, all circuitry can be installed directly onto the insertable probe[‡], secondly, the microwave components can be installed into the main body of the fridge and connected to the sample via internal lines and an RF "clicking mechanism" that couples to the probe. As shown in Fig. A.11, internal microwaves lines connect each stage; 14 coaxial excitation lines with copper/nickel alloy inner and outer conductors and 2 measurement lines with superconducting niobium-titanium inner and outer conductors run between the stages. All excitation lines are attenuated at each stage to thermalize the electronic temperature (reduce the Johnson noise to the appropriate level).

The insertable, top-loaded probe is shown in Fig. A.12 with the electronically controlled bellows

[†]In principle, raising the evaporation rate results in more cooling power and a high base temperature but in practice the rate must be adjusted to find the proper balance for a given setup.

[‡]The cooling power of the probe is limited by the thermal contact to the cold plates so caution must be taken if active elements such as amplifiers are required.

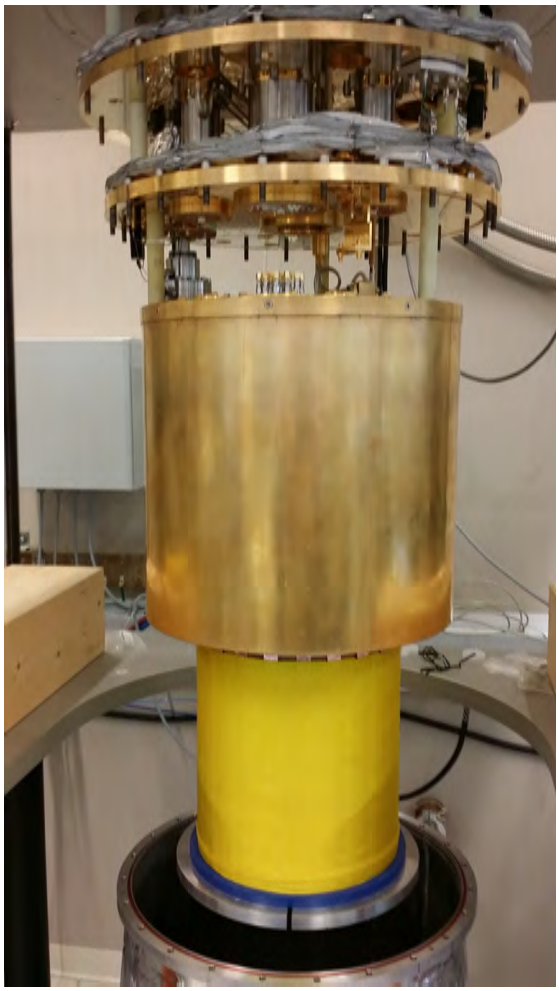

Figure A.9: Image of the $5\,T$ superconducting magnet, made by American Magnet Inc, installed in the Leiden system. The magnet is thermalized to the still plate and thus operates near $1\,K$.

Figure A.10: Close up of the Leiden IVC plates. Starting from the top, the shown plates are the $4\,K$, still, $100\,mK$, and mixing chamber plates. The still is the silver piece seen on the left side of the image mounted on the top side of the still plate. Image taken in Leiden, Netherlands while constructing the fridge. At the bottom of the image, the "tail" that extends down into the magnet bore can be seen

Figure A.11: Image of the microwave lines inside in the body of the Leiden cryostat. Shown here are the 14 excitation lines connecting the still plate to the mixing chamber plate attenuated at every stage. Not shown are the 2 superconducting measurement lines installed alongside these without attenuators.

lowered. The probe holds up to 8 high frequency lines and over 24 DC lines if needed. For each of the five temperature stages in the main fridge body, the probe has a corresponding set of pneumatic expanding thermalization plates; once the probe is fully inserted, these plates expand to thermally sink each stage of the insert to a stage in the main body[†]. A location to place 8 SMA bulkheads is built into every temperature stage. Attached to the final (mixing chamber) stage in a long extension arm which reaches into the magnet bore. The sample is placed at the end of this extender.

For the experiments in this dissertation, the number of cold microwave elements was small and thus all components could be installed onto the probe itself. Fig. A.13 shows an example of one the these circuits. A cold amplifier[‡] is mounted to the $4\ K$ stage and a bias-tee along with two directional couples are attached to allow for DC transport and RF reflection/gain measurements.

At the bottom of the probe (where the sample sits) is a plate with 16 SMP (smooth barrel) connectors pointing downward that fit into matching connectors installed in the main fridge body. When the probe is fully inserted, these connectors make an RF connection between the probe and the main body of the Leiden allowing experiments that require more complicated circuitry to use the ample space and cooling power of the main fridge. Fig. A.14 shows an image of the underside of this "clicking" mechanism where 16 SMA connectors can be used to probe the sample.

[†]While most stages sink well, the $50\ K$ stage is in the OVC and, therefore, has to thermalize through a SS tube.

[‡]Cal-Tech CITLF3

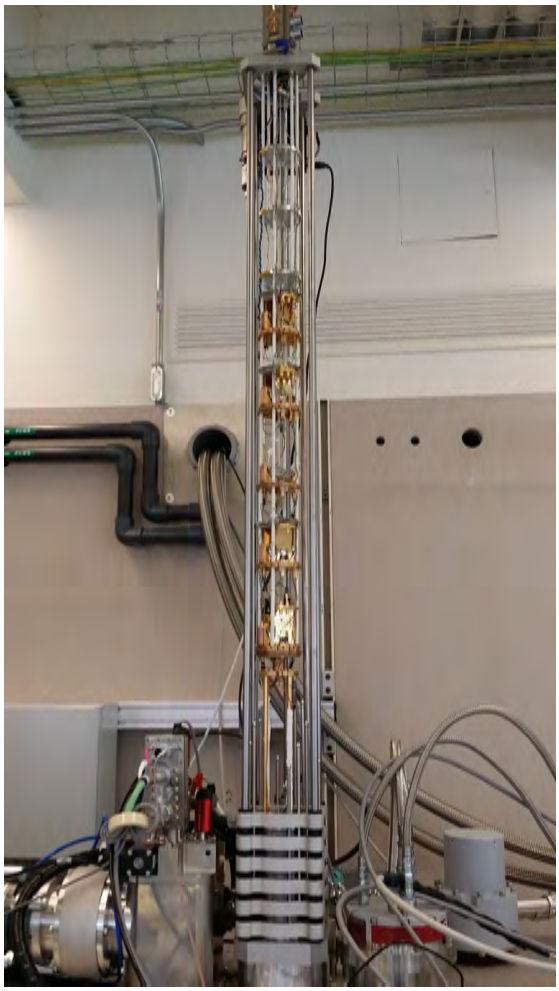

Figure A.12: Image of the insertable, top-loading probe built for the Leiden dilution refrigerator with the retractable bellows lowered. Each gold plated copper section mechanically expands once inserted to thermalize to a stage in the main fridge body. Near the bottom of the probe, and extender is seen which, during operation, contains the sample and is lowered into the magnet bore.

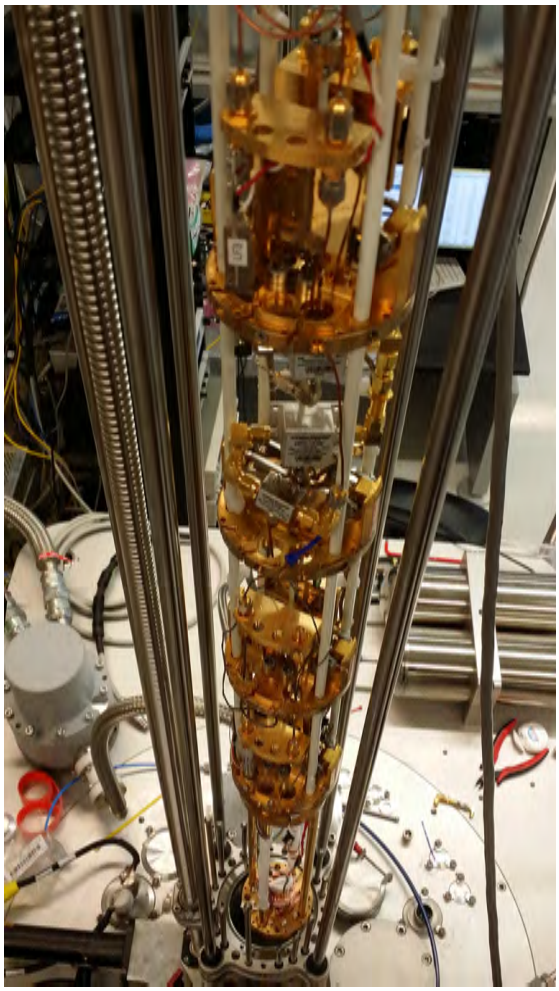

Figure A.13: An image of a microwave noise measurement circuit installed on the Leiden probe. A low noise amplifier is mounted to the $4\,K$ plate and a bias-tee along with two directional couples are attached. This setup allows RF reflection and gain measurements of the sample and amplifier, respectively, as well as DC transport and RF noise measurements.

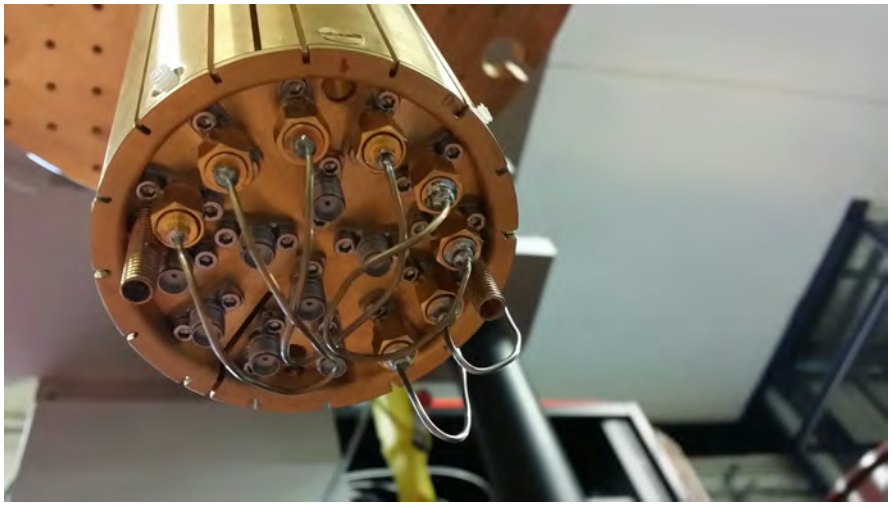

Figure A.14: Image of the underside of the "clicking" mechanism in the Leiden located in the main body of the fridge at the end of the tail that extends into the magnet bore. 16 SMA connectors are available and correspond to the 16 SMP connectors on the end of the probe. When the probe is fully inserted, these connectors form an RF connection between the probe and the main fridge body.

B

Hydrodynamic framework

B.1 Thermodynamics

In this appendix and in every subsequent appendix, we will work in units where $\hbar = k_{\mathrm{B}} = v_{\mathrm{F}} = e = 1$. It is straightforward using dimensional analysis to restore these units.

We consider the equations of state of the relativistic plasma in a relativistic strongly interacting

fluid in $d = 2$. Without specific microscopic details, these are very general facts about relativistic plasmas without an intrinsic mass scale (or gap). The discussion generalizes straightforwardly to other d. The only relevant energy scales are the temperature T and the chemical potential μ. We have the general Gibbs-Duhem relation:

$$\epsilon + P = \mu n + Ts, \tag{B.1}$$

where ϵ is the energy density, P is the pressure, s is the entropy density and n is the charge density ($n = 0$ at the particle-hole symmetric Dirac point). In a relativistic fluid,

$$P = T^3 \mathcal{F}\left(\frac{\mu}{T}\right) \tag{B.2}$$

for some dimensionless function $\mathcal{F}$. Thermodynamic identities imply that

$$n = \frac{\partial P}{\partial \mu} = T^2 \mathcal{F}'\left(\frac{\mu}{T}\right) \tag{B.3a}$$

$$s = \frac{\partial P}{\partial T} = 3T^2 \mathcal{F} - \mu T \mathcal{F}'\left(\frac{\mu}{T}\right) = \frac{3P - \mu n}{T}. \tag{B.3b}$$

Combining (B.1) and (B.3) we obtain

$$\epsilon = 2P. \tag{B.4}$$

The hydrodynamic description is only sensible for $\mu \ll T$ – for $\mu \gg T$ the standard Fermi liquid description applies. Furthermore, the equations of state of the Dirac fluid are charge conjugation

symmetric, implying that $\mathcal{F}$ is an even function of μ. So we Taylor expand:

$$\mathcal{F}\left(\frac{\mu}{T}\right) \approx \frac{C_0}{3} + \frac{C_2}{2}\left(\frac{\mu}{T}\right)^2 + \frac{C_4}{4}\left(\frac{\mu}{T}\right)^4. \tag{B.5}$$

Using (B.3):

$$n = C_2 \mu T + C_4 \frac{\mu^3}{T}, \tag{B.6a}$$

$$s = C_0 T^2 + \frac{C_2 \mu^2}{2} - \frac{C_4 \mu^4}{4T^2}. \tag{B.6b}$$

We also require that $C_0, C_2 \geq 0$, so that $s \geq 0$ and that n/μ is positive as $\mu \to 0$, as it should be.

B.1.1 Thermodynamics of Disordered Fluids

Already at this point we can make interesting predictions about the thermodynamics of the strongly interacting hydrodynamic regime in graphene. For concreteness, let us suppose that the background chemical potential is

$$\mu_0(\mathrm{x}) = \bar{\mu}_0 + \hat{\mu}(\mathrm{x}), \tag{B.7}$$

with $\bar{\mu}_0$ a constant and $\hat{\mu}$ a zero-mean random function; for simplicity, suppose that $\hat{\mu}$ is evenly distributed about zero, and has a disorder correlation length of $\xi \gtrsim l_{\mathrm{ee}}$, so that the hydrodynamic

description applies. In this case, spatially averaging over μ_0, we find

$$\langle \epsilon \rangle = \frac{2C_0}{3} T^3 + C_2 T \left(\bar{\mu}_0^2 + \langle \hat{\mu}^2 \rangle \right) + \frac{C_4}{2} \left(\bar{\mu}_0^4 + 6\bar{\mu}_0^2 \langle \hat{\mu}^2 \rangle + \langle \hat{\mu}^4 \rangle \right) + \cdots . \tag{B.8}$$

The $\cdots$ denotes higher order terms in the equation of state that we have neglected. A similar expression can be found for the charge density:

$$\langle n \rangle = C_2 T \bar{\mu}_0 + \frac{3C_4}{T} \bar{\mu}_0 \langle \hat{\mu}^2 \rangle + \cdots . \tag{B.9}$$

Let us focus on a clean limit where $\hat{\mu}$ is very small relative to T. Let us also assume that we are close to the Dirac point, so that only C_0 and C_2 terms need to be kept. Thermodynamics then gives tight constraints on the behavior of measurable quantities: specific heat and compressibility, in an experimentally testable regime, due to the ability to easily tune both T and $\bar{\mu}_0$ (the average charge density) experimentally. In the limit above, the (spatially averaged) compressibility $\mathcal{K}$ is

$$\frac{1}{\mathcal{K}} = \frac{\partial \langle n \rangle}{\partial \mu} = C_2 T. \tag{B.10}$$

where as before, we use $\langle \cdots \rangle$ to denote a uniform spatial average. Note that the independence of $\mathcal{K}$ to $\bar{\mu}_0$ and $\hat{\mu}$ is simply a consequence of the fact that we did not expand (B.5) to quartic order. The spatially averaged specific heat

$$c = \frac{\partial \langle \epsilon \rangle}{\partial T} = 2C_0 T^2 + C_2 \left(\bar{\mu}_0^2 + \langle \hat{\mu}^2 \rangle \right) . \tag{B.11}$$

The experimental consequence of this result is as follows. Very close to the Dirac point, we expect that $\mathcal{K}$ is approximately constant. Restoring all dimensional prefactors, we can therefore set

$$C_2 \approx \frac{(\hbar v_{\mathrm{F}})^2}{\mathcal{K} k_{\mathrm{B}} T} \tag{B.12}$$

and re-write

$$c \approx 2C_0 \frac{k_{\mathrm{B}}^3 T^2}{(\hbar v_{\mathrm{F}})^2} + 2\frac{\bar{\mu}_0^2 + \langle \hat{\mu}^2 \rangle}{\mathcal{K} T} \approx 2C_0 \frac{k_{\mathrm{B}}^3 T^2}{(\hbar v_{\mathrm{F}})^2} + 2\frac{\langle \hat{\mu}^2 \rangle}{\mathcal{K} T} + \frac{2\mathcal{K} n^2}{T}. \tag{B.13}$$

We thus see that the quadratic dependence in $c(n)$ gives us an independent measurement of $\mathcal{K}$ through a measurement of the heat capacity. In principle, a quadratic polynomial fit to $c(n)$ thus determines both $\mathcal{K}$ and C_0, up to the residual effects of disorder, which will lead to an overestimate of C_0. Repeating measurements of $\mathcal{K}$ directly, as well as $c(n)$ at different T, provide non-trivial checks on the above theory. It is important to note that this argument does *not* rely on the validity of hydrodynamics, only that graphene is gapless, $\bar{\mu}_0 \ll T$, and that $\hat{\mu}$ is very small. Of these three requirements, the last poses the biggest experimental hurdle.

In the above argument, there is no reason a priori why to truncate the Taylor expansion to neglect C_4 and higher order corrections, beyond appealing to the weak disorder limit. In particular, inclusion of C_4 complicates our ability to obtain an accurate measure of $\bar{\mu}_0$ from n. The argument above is simply meant to give a flavor for the constraints on measurable quantities imposed by scale invariant thermodynamics. A more systematic treatment is likely necessary to make quantitative contact

with future experiments.

B.2 Rescaling Symmetries of dc Transport

Solutions to (7.14) are invariant, up to global rescalings, under certain rescalings of the linearized hydrodynamic equations of motion. These symmetries are, assuming $\lambda > 0$ is a constant scaling parameter:

$$\eta \to \lambda^2 \eta, \quad x \to \lambda x; \tag{B.14a}$$

$$\eta \to \lambda\eta, \quad \sigma \to \lambda\sigma, \quad \alpha \to \lambda\alpha, \quad \kappa \to \lambda\kappa, \quad P \to \lambda P; \tag{B.14b}$$

$$\alpha \to \lambda\alpha, \quad \kappa \to \lambda^2\kappa, \quad \eta \to \lambda^{-2}\eta, \quad \mu_0 \to \lambda\mu_0, \quad C_2 \to \lambda^{-2}C_2, \quad C_4 \to \lambda^{-4}C_4, \quad \text{etc.}; \tag{B.14c}$$

$$\alpha \to \lambda\alpha, \quad \kappa \to \lambda\kappa, \quad \sigma \to \lambda\sigma, \quad \eta \to \lambda^{-1}\eta. \tag{B.14d}$$

Everything not listed is invariant. ζ and η have the same scalings, as do σ and σ_Q, and so we have only listed some of these parameters.

These rescalings are useful to help us compare simulations to experimental data from graphene. The latter three rescalings can be used to help fix the overall magnitude of κ and σ, as well as the values of n, as measured in experiment. These are exactly analogous to the symmetries of the Navier-Stokes equation, which allow us to reduce all such hydrodynamic problems to a universal equation,

up to a single dimensionless parameter. [55] neither measured the viscosity directly nor the charge puddle size, and the first scaling above implies that we cannot determine viscosity alone. So, as mentioned in the main text, we assume that $\xi = l_{\text{ee}}$, the shortest possible value of ξ for which hydrodynamics seems sensible.

B.3 Weak Disorder

Many analytic results can be obtained in the limit where the disorder strength is "small". We provide detailed derivations of all such results in this appendix. We introduce disorder as in (7.17). Below we denote $n_0 = n(\bar{\mu}_0)$, etc.

The perturbative solution is found exactly as was done in [88]: we split the velocity field into a constant piece $\bar{v}_i \sim u^{-2}$, and a fluctuating zero-mean piece $\hat{v}_i \sim u^{-1}$; similarly, $\mu \sim T \sim u^{-1}$. It proves convenient to work in Fourier space. At $\mathrm{O}(u^{-1})$, the momentum conservation equation becomes

$$-\mathrm{i}k_i \left(n_0\mu(\mathrm{k}) + s_0 T(\mathrm{k})\right) = \eta_0 k^2 \hat{v}_i(\mathrm{k}) + \zeta_0 k_i k_j \hat{v}_j(\mathrm{k}), \tag{B.15}$$

and the conservation laws become (at the same order)

$$0 = \mathrm{i}k_i \left(\hat{n}(\mathrm{k})\bar{v}_i + n_0 \hat{v}_i(\mathrm{k})\right) + \sigma_{\mathrm{Q}0} k^2 \left(\mu(\mathrm{k}) - \frac{\mu_0}{T_0} T(\mathrm{k})\right), \tag{B.16a}$$

$$0 = \mathrm{i}k_i T_0 \left(\hat{s}(\mathrm{k})\bar{v}_i + s_0 \hat{v}_i(\mathrm{k})\right) - \mu_0 \sigma_{\mathrm{Q}0} k^2 \left(\mu(\mathrm{k}) - \frac{\mu_0}{T_0} T(\mathrm{k})\right). \tag{B.16b}$$

Combining these equations we obtain expressions for T, μ and $k_i\hat{v}_i$:

$$k_i\hat{v}_i(\mathrm{k}) = -\frac{\mu_0\hat{n}(\mathrm{k}) + T_0\hat{s}(\mathrm{k})}{\mu_0 n_0 + T_0 s_0} k_i\bar{v}_i, \tag{B.17a}$$

$$T(\mathrm{k}) = -\frac{\mathrm{i}k_i\bar{v}_i}{\sigma_{\mathrm{Q}0}k^2(\epsilon_0+P_0)^2}\left(\sigma_{\mathrm{Q}0}k^2(\eta_0+\zeta_0)(\mu_0\hat{n}+T_0\hat{s})T_0 - T_0 n_0(T_0 s_0\hat{n} - T_0 n_0\hat{s})\right), \tag{B.17b}$$

$$\mu(\mathrm{k}) = -\frac{\mathrm{i}k_i\bar{v}_i}{\sigma_{\mathrm{Q}0}k^2(\epsilon_0+P_0)^2}\left(\sigma_{\mathrm{Q}0}k^2(\eta_0+\zeta_0)(\mu_0\hat{n}+T_0\hat{s})\mu_0 + T_0 s_0(T_0 s_0\hat{n} - T_0 n_0\hat{s})\right). \tag{B.17c}$$

Spatially averaging over the momentum conservation equation at $\mathrm{O}(u^0)$, and defining:

$$(\epsilon+P)\tau_{ij}^{-1}\bar{v}_j \equiv \sum_{\mathrm{k}} \mathrm{i}k_i\left[\hat{n}(-\mathrm{k})\mu(\mathrm{k}) + \hat{s}(-\mathrm{k})T(\mathrm{k})\right], \tag{B.18}$$

we find that

$$\tau_{ij}^{-1} = \sum_{\mathrm{k}} \frac{k_i k_j}{k^2}\frac{|T_0 s_0\hat{n}(\mathrm{k}) - T_0 n_0\hat{s}(\mathrm{k})|^2 + \sigma_{\mathrm{Q}0}k^2(\eta_0+\zeta_0)\,|\mu_0\hat{n}(\mathrm{k}) + T_0\hat{s}(\mathrm{k})|^2}{\sigma_{\mathrm{Q}0}(\epsilon_0+P_0)^3} \tag{B.19}$$

and that the spatially averaged momentum equation reduces to

$$0 = n_0 E_i + T_0 s_0\zeta_i - (\epsilon_0+P_0)\tau_{ij}^{-1}\bar{v}_j. \tag{B.20}$$

In this equation, we have used the fact that $J_i \approx n\bar{v}_i$ at leading order in perturbation theory. The

resulting transport coefficients are analogous to (7.18):

$$\sigma_{ij} = \frac{n_0^2}{\epsilon_0 + P_0}\tau_{ij}, \tag{B.21a}$$

$$\bar{\alpha}_{ij} = \alpha_{ij} = \frac{n_0 s_0}{\epsilon_0 + P_0}\tau_{ij}, \tag{B.21b}$$

$$\bar{\kappa}_{ij} = \frac{T s_0^2}{\epsilon_0 + P_0}\tau_{ij}. \tag{B.21c}$$

In the expression for σ, we have not included a $\sigma_{\mathcal{Q}0}$ contribution, as was done in [87], as this is a subleading order in perturbation theory.

Using our Taylor expanded equations of state for the fluid and assuming $C_4 = 0$, since

$$\hat{s}(\mathrm{k}) \approx C_2 \mu_0 \hat{\mu}(\mathrm{k}) = \frac{\mu_0}{T_0}\hat{n}(\mathrm{k}), \tag{B.22}$$

we can simplify (B.19) to

$$\tau_{ij}^{-1} = \sum_{\mathrm{k}} \frac{k_i k_j}{k^2} \frac{(T_0 s_0 - \mu_0 n_0)^2 + 4\sigma_{\mathcal{Q}0} k^2 (\eta_0 + \zeta_0)\mu_0^2}{\sigma_{\mathcal{Q}0}(\epsilon_0 + P_0)^3} \left|\hat{n}(\mathrm{k})\right|^2 \tag{B.23}$$

Similar results were presented (in a different format) in [114], though the practical consequences of this formula, as discussed in the main text, have not previously been understood.

We cannot take the naive limit where $\sigma_{\mathcal{Q}0} \sim u^{-2}$ in order to recover (7.2) in full generality. The simplest way to see that something goes wrong is to study $\bar{\kappa}$ near $\bar{\mu}_0 = 0$ (more precisely, $\bar{\mu}_0 \sim u$): if $\sigma_{\mathcal{Q}} \sim u^{-2}$ we find that $\tau \sim u^{-4}$, and this implies that the heat current (and thus $\bar{\kappa}$) would be

parametrically larger than anticipated. Thus our perturbative scaling breaks down. The breakdown of the perturbative theory for $u \sim \bar{\mu}_0$ was also advocated in [88].

Although we have argued there are problems in principle with (7.2) when $\bar{\mu}_0 \sim u$, even when u is perturbatively small, in practice the mean-field model of [87] can be quite good in practice near $\bar{\mu}_0 \sim u$, as shown in Figure 7.6. Note that it is also important that $C_0 T^2 \gg C_2 u^2$ – when this limit is violated, we see substantial deviations from (7.2) at all $\bar{\mu}_0$, as shown in Figure 7.6. This may be a consequence of our assumption that σ_Q is independent of μ_0.

B.4 Equations of State of the Dirac Fluid

The thermodynamics of graphene is similar to that presented in Appendix B.1, with some minor differences. Perturbative computations and renormalization group arguments, valid as $T \to 0$, give [132, 67]

$$C_0 = \frac{9\zeta(3)}{\pi}\left(\frac{\alpha_{\text{eff}}}{\alpha_0}\right)^2 \approx 3.44\left(\frac{\alpha}{\alpha_0}\right)^2, \tag{B.24a}$$

$$C_2 = \frac{4\log 2}{\pi}\left(\frac{\alpha_{\text{eff}}}{\alpha_0}\right)^2 \approx 0.88\left(\frac{\alpha}{\alpha_0}\right)^2. \tag{B.24b}$$

(B.24) can be derived by computing the thermodynamics of 2 species of non-interacting Dirac fermions, with Coulomb interactions leading to a logarithmically increasing Fermi velocity [132, 67]. As $\alpha_{\text{eff}}(T)$ is not a constant, this implies that the entropy has an additional contribution related to

the logarithmic T dependence of $C_{0,2}(\alpha_{\text{eff}})$. Assuming C_0 and C_2 above, and assuming $C_4 = 0$ for simplicity as its value for free fermions is quite small [60], we find:

$$s = C_0 T^2 \left[1 + \frac{\alpha_{\text{eff}}}{6}\right] + \frac{C_2}{2}\mu^2 \left[1 + \frac{\alpha_{\text{eff}}}{2}\right] \tag{B.25}$$

This equation directly implies $\epsilon > 2P$. Using the estimate $\alpha_{\text{eff}} \sim 0.25$ from above, we see that the corrections to s (and ϵ) are rather minor ($< 10\%$); n is unchanged. In fact, (B.25) is not quite right: the computation of (B.24) is only a leading order perturbative computation: there are corrections to (B.24) at higher orders in $\log \alpha_{\text{eff}}$. Nonetheless, our general conclusion that $\epsilon > 2P$ is possible in graphene continues to hold, given any logarithmic running of the Fermi velocity.

As noted above, these theoretical computations of the thermodynamic coefficients in graphene are all perturbative computations in α_{eff}, yet we only expect $\alpha_{\text{eff}}/\alpha_0 \sim 0.5$: there is no reason to expect that higher order corrections, which can be as large as $\sim \log \alpha_{\text{eff}}$, are negligible. More sensitive experiments may find discrepancies with Lorentz invariant hydrodynamics, associated with these peculiar properties of the Dirac fluid. Similar logarithms can appear in σ_Q [74] and η [73], and in both cases, for the reasons above, we neglect these logarithms and use the theory of Section 7.3.

B.5 Numerical Methods

We solved the hydrodynamic equations (7.14) on a periodic domain of size $L \times L$, employing pseudospectral methods [157] using a basis of N Fourier modes in each direction, with

$25 \lesssim N \lesssim 43$. For simplicity, we set $T_0 = 1$, as this can be restored straightforwardly by dimensional analysis. Our numerical methods involves approximating continuous partial differential equations in the form

$$\mathsf{L}\mathrm{u} = \mathrm{s}. \tag{B.26}$$

u contains the linear response fields μ, T, v_x and v_y, evaluated on a uniformly distributed discrete grid, and s contains the source terms, linear in E_i and ζ_i, evaluated at the same points. L is a matrix with two zero eigenvectors, which correspond to constant shifts in μ and T respectively. We thus remove two rows of L and replace them with constraints that $\mu(\mathrm{o}) = T(\mathrm{o}) = 0$. A simple matrix inversion thus gives $\mathrm{u} = \mathsf{L}^{-1}\mathrm{s}$. Inverting this $(4N^2 - 2) \times (4N^2 - 2)$ matrix four times (once for sources $E_{x,y}$ and $\zeta_{x,y}$) limits the size of the domain we can analyze. More complicated algorithms exist [158] to solve such problems but we did not find finite size effects to qualitatively alter our comparison to experimental data, as we discuss below.

As mentioned in the main text, our disorder realizations consisted of random sums of sine waves. More precisely,

$$\mu_0(\mathrm{x}) = \bar{\mu}_0 + \sum_{|n_x|,|n_y|\leq k} \hat{\mu}_0(n_x, n_y) \sin\left(\phi_x + \frac{2n_x\pi x}{k\xi}\right) \sin\left(\phi_y + \frac{2n_y\pi y}{k\xi}\right) \tag{B.27}$$

with $\bar{\mu}_0$ a constant, $\hat{\mu}_0(n_x, n_y)$ uniformly distributed on $[-c, c]$ where $c = \sqrt{(2 - \delta_{n_x,0} - \delta_{n_y,0})/2}$, and $\phi_{x,y}$ uniformly distributed on $[0, 2\pi)$. The lack of heavy tails in $\hat{\mu}_0(n_x, n_y)$, perhaps associated with point-like impurities, is consistent with experiment [81]. The form of c is chosen so that we do

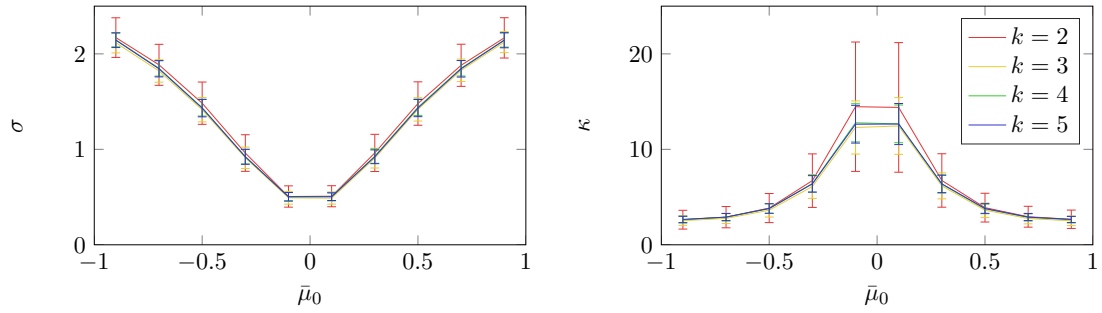

Figure B.1: Finite size effects with $u_0 = 0.3, C_0 = 3, C_2 = 1, \sigma_0 = 1, \eta_0 = 20$. Numerical averages are performed over 100 disorder realizations.

not add random charge density bias to our disorder (as the zero mode has no amplitude), and so that all Fourier modes included at finite wave number have the same average amplitude.

B.5.1 Finite Size Effects

The first source of finite size effects is simply related to the fact that we only have a finite number of disorder modes. Averaging over a large number of ensemble samples allows us to approximately, but not exactly, undo this effect: see Figures B.1 and B.2. In both cases, we used $8k + 3$ grid points in each direction for various k. To the best of our knowledge, in all numerical simulations we have studied, it appears as though the result converges to a finite fixed answer as $k \to \infty$. However, residual error from finite size effects may lead to some error in our estimation of the thermodynamic and hydrodynamic coefficients of the Dirac fluid in graphene.

The other source of finite size effects is related to the finite number of grid points in our pseudospectral methods. However, we expect standard exponential accuracy [157] in the number of grid

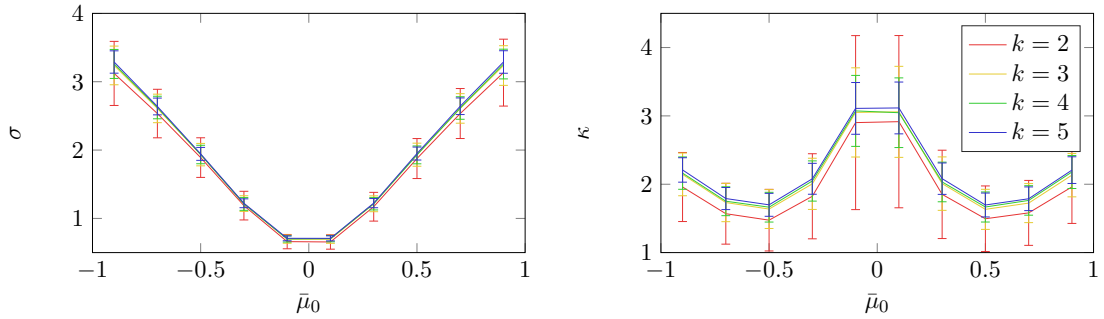

Figure B.2: Finite size effects with $u_0 = 0.3, C_0 = 1, C_2 = 1, \sigma_0 = 1, \eta_0 = 1$. Numerical averages are performed over 100 disorder realizations.

points per ξ, which we have taken to be at least 10 in all figures in the main text. Numerical evidence suggests that our spectral methods have converged to within about 0.1–1% of the correct answer by this relatively small number of grid points per ξ, depending on the precise equations of state used. In the case of the experimentally relevant parameters used in Figure 7.3, we see exponential convergence of our spectral methods with increasing grid points, with numerical error of only 0.1% by the time the number of grid points per ξ is 11, as shown in Figure B.3. This spectral convergence is dramatically faster in the weak disorder limit.

Methods are known to improve our simple algorithms, which can reduce both types of finite size effects discussed above. Given the preliminary nature of the experiments to which we compare our simulations, we have found the numerical errors described above tolerable.

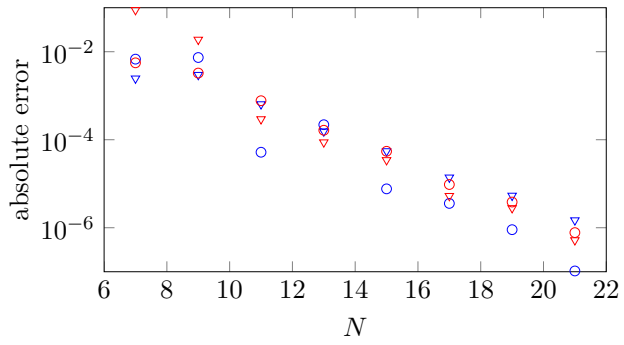

Figure B.3: Exponential convergence of our pseudospectral code with an increasing number of grid points. We computed κ and σ using our code, employing the "experimental" equations of state given in Figure 7.3, and the disorder profile $\mu_0(x) = \bar{\mu}_0 + 2u\cos(2\pi x/L)\cos(2\pi y/L)$. Red data points denote the error in κ, and blue points denote the error in σ. Circles denote data at $\bar{\mu}_0 = 2u$, and triangles at $\bar{\mu}_0 = 0.4u$. Absolute error is determined by (e.g.) $|\sigma(N) - \sigma(29)|/\sigma(29)$, where we use the data points at $N = 29$ as a reference point.

B.5.2 Dimensional Analysis

We have performed numerical computations in dimensionless units, since we can trivially restore the units to our numerical results via dimensional analysis. Setting $\hbar = k_{\mathrm{B}} = e = v_{\mathrm{F}} = T_0 = 1$ completely non-dimensionalizes the problem, while setting no dimensionless parameters to

unity. We can now trivially restore the units as follows:

$$L = \frac{\hbar v_{\mathrm{F}}}{k_{\mathrm{B}} T_0} \times L_{\text{numerics}} \sim (100\ \mathrm{nm}) \times L_{\text{numerics}} \tag{B.28a}$$

$$\mu = k_{\mathrm{B}} T_0 \times \mu_{\text{numerics}} \sim (5\ \mathrm{meV}) \times \mu_{\text{numerics}}, \tag{B.28b}$$

$$\sigma = \frac{e^2}{\hbar} \times \sigma_{\text{numerics}} \sim (0.25\ \mathrm{k}\square^{-1}) \times \sigma_{\text{numerics}}, \tag{B.28c}$$

$$\alpha = \frac{k_{\mathrm{B}} e}{\hbar} \times \alpha_{\text{numerics}} \sim \left(20\ \frac{\mathrm{nW}}{\mathrm{V}}\right) \times \alpha_{\text{numerics}}, \tag{B.28d}$$

$$\kappa = \frac{k_{\mathrm{B}}^2 T_0}{\hbar} \times \kappa_{\text{numerics}} \sim \left(0.1\ \frac{\mathrm{nW}}{\mathrm{K}}\right) \times \kappa_{\text{numerics}}. \tag{B.28e}$$

We have also noted the approximate scale of each important physical quantity in the problem for convenience.

References

[1] Albert Einstein. *Investigations on the Theory of the Brownian Movement*. Courier Corporation, 1956. ISBN 978-0-486-60304-9.

[2] R. Kubo. The fluctuation-dissipation theorem. *Reports on Progress in Physics*, 29(1):255, 1966. ISSN 0034-4885. doi: 10.1088/0034-4885/29/1/306. URL http://stacks.iop.org/0034-4885/29/i=1/a=306.

[3] Herbert B. Callen and Theodore A. Welton. Irreversibility and Generalized Noise. *Physical Review*, 83(1):34–40, July 1951. doi: 10.1103/PhysRev.83.34. URL http://link.aps.org/doi/10.1103/PhysRev.83.34.

[4] H. Nyquist. Thermal Agitation of Electric Charge in Conductors. *Physical Review*, 32(1):110–113, July 1928. doi: 10.1103/PhysRev.32.110. URL http://link.aps.org/doi/10.1103/PhysRev.32.110.

[5] John B Johnson. Thermal agitation of electricity in conductors. *Nature*, 119(2984):50–51, 1927.

[6] J. B. Johnson. Thermal Agitation of Electricity in Conductors. *Physical Review*, 32(1):97–109, July 1928. doi: 10.1103/PhysRev.32.97. URL http://link.aps.org/doi/10.1103/PhysRev.32.97.

[7] R. H. Dicke. The Measurement of Thermal Radiation at Microwave Frequencies. *Review of Scientific Instruments*, 17(7):268–275, July 1946. ISSN 0034-6748. doi: 10.1063/1.1770483. URL http://aip.scitation.org/doi/abs/10.1063/1.1770483.

[8] R. J. Schoelkopf, P. J. Burke, A. A. Kozhevnikov, D. E. Prober, and M. J. Rooks. Frequency Dependence of Shot Noise in a Diffusive Mesoscopic Conductor. *Physical Review Letters*, 78(17):3370–3373, April 1997. doi: 10.1103/PhysRevLett.78.3370. URL http://link.aps.org/doi/10.1103/PhysRevLett.78.3370.

[9] David M. Pozar. *Microwave Engineering*. Wiley, Hoboken, NJ, 4 edition edition, November 2011. ISBN 978-0-470-63155-3.

[10] Jesse Crossno, Xiaomeng Liu, Thomas A. Ohki, Philip Kim, and Kin Chung Fong. Development of high frequency and wide bandwidth Johnson noise thermometry. *Applied Physics Letters*, 106(2):023121, January 2015. ISSN 0003-6951, 1077-3118. doi: 10.1063/1.4905926. URL http://arxiv.org/abs/1411.4596. arXiv: 1411.4596.

[11] S. O. Rice. Mathematical analysis of random noise. *The Bell System Technical Journal*, 23(3): 282–332, July 1944. ISSN 0005-8580. doi: 10.1002/j.1538-7305.1944.tb00874.x.

[12] Paul Horowitz and Winfield Hill. *The Art of Electronics*. Cambridge University Press, Cambridge England ; New York, 2 edition edition, July 1989. ISBN 978-0-521-37095-0.

[13] D. R. White, R. Galleano, A. Actis, H. Brixy, M. De Groot, J. Dubbeldam, A. L. Reesink, F. Edler, H. Sakurai, R. L. Shepard, and J. C. Gallop. The status of Johnson noise thermometry. *Metrologia*, 33(4):325, 1996. ISSN 0026-1394. doi: 10.1088/0026-1394/33/4/6. URL http://stacks.iop.org/0026-1394/33/i=4/a=6.

[14] D. C. Glattli, P. Jacques, A. Kumar, P. Pari, and L. Saminadayar. A noise detection scheme with 10 mK noise temperature resolution for semiconductor single electron tunneling devices. *Journal of Applied Physics*, 81:7350–7356, June 1997. ISSN 0021-8979. doi: 10.1063/1.365332. URL http://adsabs.harvard.edu/abs/1997JAP....81.7350G.

[15] L. DiCarlo, Y. Zhang, D. T. McClure, C. M. Marcus, L. N. Pfeiffer, and K. W. West. System for measuring auto-and cross correlation of current noise at low temperatures. *Rev Sci Instrum*, 77(7):073906–073906–7, 2006.

[16] M. Henny, S. Oberholzer, C. Strunk, and C. Schönenberger. 1/3-shot-noise suppression in diffusive nanowires. *Physical Review B*, 59(4):2871, 1999.

[17] James J. Brophy, Max Epstein, and Samuel L. Webb. Correlator-Amplifier for Very Low Level Signals. *Rev Sci Instrum*, 36(12):1803–1806, 1965. doi: 10.1063/1.1719469.

[18] H.-H. Klein, G. Klempt, and L. Storm. Measurement of the Thermodynamic Temperature of 4 He at Various Vapour Pressures by a Noise Thermometer. *Metrologia*, 15(3):143, 1979. ISSN 0026-1394. doi: 10.1088/0026-1394/15/3/005. URL http://stacks.iop.org/0026-1394/15/i=3/a=005.

[19] N. Sampietro, Gianfranco Accomando, Luca Fasoli, Giorgio Ferrari, and Emilio Gatti. High sensitivity noise measurement with a correlation spectrum analyzer. *Instrumentation and Measurement, IEEE Transactions on*, 49(4):820–822, 2000.

[20] Neil W. Ashcroft and N. David Mermin. *Solid State Physics*. Brooks Cole, New York, 1 edition edition, January 1976. ISBN 978-0-03-083993-1.

[21] Christopher McKitterick, Daniel Prober, and Boris Karasik. Performance of graphene thermal photon detectors. *J Appl Phys*, 113(4):044512–044512–6, 2013.

[22] Christopher B. McKitterick, Daniel E. Prober, and Michael J. Rooks. Electron-phonon cooling in large monolayer graphene devices. *Physical Review B*, 93(7):075410, February 2016. doi: 10.1103/PhysRevB.93.075410. URL https://link.aps.org/doi/10.1103/PhysRevB.93.075410.

[23] R. Franz and G. Wiedemann. Ueber die Wärme-Leitungsfähigkeit der Metalle. *Annalen der Physik*, 165(8):497–531, January 1853. ISSN 1521-3889. doi: 10.1002/andp.18531650802. URL http://onlinelibrary.wiley.com/doi/10.1002/andp.18531650802/abstract.

[24] L. Lorenz. Bestimmung der Wärmegrade in absolutem Maasse. *Annalen der Physik*, 223 (11):429–452, January 1872. ISSN 1521-3889. doi: 10.1002/andp.18722231107. URL http://onlinelibrary.wiley.com/doi/10.1002/andp.18722231107/abstract.

[25] G. S. Kumar, G. Prasad, and R. O. Pohl. Experimental determinations of the Lorenz number. *Journal of Materials Science*, 28(16):4261–4272, August 1993. ISSN 0022-2461, 1573-4803. doi: 10.1007/BF01154931. URL https://link.springer.com/article/10.1007/BF01154931.

[26] A. Sommerfeld. Zur Elektronentheorie der Metalle. *Naturwissenschaften*, 15(41):825–832, October 1927. ISSN 0028-1042, 1432-1904. doi: 10.1007/BF01505083. URL https://link.springer.com/article/10.1007/BF01505083.

[27] Andrew H. Steinbach, John M. Martinis, and Michel H. Devoret. Observation of Hot-Electron Shot Noise in a Metallic Resistor. *Physical Review Letters*, 76(20):3806–3809, May 1996. doi: 10.1103/PhysRevLett.76.3806. URL https://link.aps.org/doi/10.1103/PhysRevLett.76.3806.

[28] Ya M. Blanter and M. Buttiker. Shot Noise in Mesoscopic Conductors. *Physics Reports*, 336 (1-2):1–166, September 2000. ISSN 03701573. doi: 10.1016/S0370-1573(99)00123-4. URL http://arxiv.org/abs/cond-mat/9910158. arXiv: cond-mat/9910158.

[29] M. J. M. de Jong and C. W. J. Beenakker. Semiclassical theory of shot noise in mesoscopic conductors. *Physica A: Statistical Mechanics and its Applications*, 230(1):219–248, August 1996. ISSN 0378-4371. doi: 10.1016/0378-4371(96)00068-4. URL http://www.sciencedirect.com/science/article/pii/0378437196000684.

[30] J. K. Viljas and T. T. Heikkilä. Electron-phonon heat transfer in monolayer and bilayer graphene. *Physical Review B*, 81(24):245404, June 2010. doi: 10.1103/PhysRevB.81.245404. URL http://link.aps.org/doi/10.1103/PhysRevB.81.245404.

[31] R. Bistritzer and A. H. MacDonald. Electronic Cooling in Graphene. *Physical Review Letters*, 102(20):206410, May 2009. doi: 10.1103/PhysRevLett.102.206410. URL http://link.aps.org/doi/10.1103/PhysRevLett.102.206410.

[32] Justin C. W. Song, Michael Y. Reizer, and Leonid S. Levitov. Disorder-Assisted Electron-Phonon Scattering and Cooling Pathways in Graphene. *Physical Review Letters*, 109(10):106602, September 2012. doi: 10.1103/PhysRevLett.109.106602. URL http://link.aps.org/doi/10.1103/PhysRevLett.109.106602.

[33] Wei Chen and Aashish A. Clerk. Electron-phonon mediated heat flow in disordered graphene. *Physical Review B*, 86(12):125443, September 2012. doi: 10.1103/PhysRevB.86.125443. URL http://link.aps.org/doi/10.1103/PhysRevB.86.125443.

[34] Thibault Sohier, Matteo Calandra, Cheol-Hwan Park, Nicola Bonini, Nicola Marzari, and Francesco Mauri. Phonon-limited resistivity of graphene by first-principles calculations: Electron-phonon interactions, strain-induced gauge field, and Boltzmann equation. *Physical Review B*, 90(12):125414, September 2014. doi: 10.1103/PhysRevB.90.125414. URL https://link.aps.org/doi/10.1103/PhysRevB.90.125414.

[35] K. J. Tielrooij, N. C. H. Hesp, A. Principi, M. Lundeberg, E. A. A. Pogna, L. Banszerus, Z. Mics, M. Massicotte, P. Schmidt, D. Davydovskaya, K. Watanabe, T. Taniguchi, M. Bonn, D. Turchinovich, C. Stampfer, G. Cerullo, M. Polini, and F. H. L. Koppens. Out-of-plane heat transfer in van der Waals stacks: electron-hyperbolic phonon coupling. *arXiv:1702.03766 [cond-mat]*, February 2017. URL http://arxiv.org/abs/1702.03766. arXiv: 1702.03766.

[36] Jürgen Schiefele, Fernando Sols, and Francisco Guinea. Temperature dependence of the conductivity of graphene on boron nitride. *Physical Review B*, 85(19):195420, May 2012. doi:

10.1103/PhysRevB.85.195420. URL https://link.aps.org/doi/10.1103/PhysRevB.85.195420.

[37] F. Bloch. Zum elektrischen Widerstandsgesetz bei tiefen Temperaturen. *Zeitschrift für Physik*, 59(3-4):208–214, March 1930. ISSN 0044-3328. doi: 10.1007/BF01341426. URL https://link.springer.com/article/10.1007/BF01341426.

[38] E. Grüneisen. Die Abhängigkeit des elektrischen Widerstandes reiner Metalle von der Temperatur. *Annalen der Physik*, 408(5):530–540, January 1933. ISSN 1521-3889. doi: 10.1002/andp.19334080504. URL http://onlinelibrary.wiley.com/doi/10.1002/andp.19334080504/abstract.

[39] H. L. Stormer, L. N. Pfeiffer, K. W. Baldwin, and K. W. West. Observation of a Bloch-Gr\"uneisen regime in two-dimensional electron transport. *Physical Review B*, 41(2):1278–1281, January 1990. doi: 10.1103/PhysRevB.41.1278. URL https://link.aps.org/doi/10.1103/PhysRevB.41.1278.

[40] Dmitri K. Efetov and Philip Kim. Controlling Electron-Phonon Interactions in Graphene at Ultrahigh Carrier Densities. *Physical Review Letters*, 105(25):256805, December 2010. doi: 10.1103/PhysRevLett.105.256805. URL https://link.aps.org/doi/10.1103/PhysRevLett.105.256805.

[41] Kin Chung Fong, Emma E. Wollman, Harish Ravi, Wei Chen, Aashish A. Clerk, M. D. Shaw, H. G. Leduc, and K. C. Schwab. Measurement of the Electronic Thermal Conductance Channels and Heat Capacity of Graphene at Low Temperature. *Physical Review X*, 3(4):041008, October 2013. doi: 10.1103/PhysRevX.3.041008. URL http://link.aps.org/doi/10.1103/PhysRevX.3.041008.

[42] A. C. Betz, S. H. Jhang, E. Pallecchi, R. Ferreira, G. Fève, J.-M. Berroir, and B. Plaçais. Supercollision cooling in undoped graphene. *Nature Physics*, 9(2):109–112, February 2013. ISSN 1745-2473. doi: 10.1038/nphys2494. URL http://www.nature.com/nphys/journal/v9/n2/abs/nphys2494.html.

[43] Matt W. Graham, Su-Fei Shi, Daniel C. Ralph, Jiwoong Park, and Paul L. McEuen. Photocurrent measurements of supercollision cooling in graphene. *Nature Physics*, 9(2):103–108, February 2013. ISSN 1745-2473. doi: 10.1038/nphys2493. URL http://www.nature.com/nphys/journal/v9/n2/abs/nphys2493.html.

[44] S. S. Kubakaddi. Interaction of massless Dirac electrons with acoustic phonons in graphene at low temperatures. *Physical Review B*, 79(7):075417, February 2009. doi: 10.1103/PhysRevB.79.075417. URL http://link.aps.org/doi/10.1103/PhysRevB.79.075417.

[45] Tony Low, Vasili Perebeinos, Raseong Kim, Marcus Freitag, and Phaedon Avouris. Cooling of photoexcited carriers in graphene by internal and substrate phonons. *Physical Review B*, 86(4):045413, July 2012. doi: 10.1103/PhysRevB.86.045413. URL https://link.aps.org/doi/10.1103/PhysRevB.86.045413.

[46] D. R. Schmidt, R. J. Schoelkopf, and A. N. Cleland. Photon-Mediated Thermal Relaxation of Electrons in Nanostructures. *Physical Review Letters*, 93(4):045901, July 2004. doi: 10.1103/PhysRevLett.93.045901. URL https://link.aps.org/doi/10.1103/PhysRevLett.93.045901.

[47] Christopher Burt McKitterick. *Prospects for Ultra-sensitive Terahertz Photon Detection with Graphene*. PhD thesis, Yale University, 2015. URL http://proberlab.yale.edu/sites/default/files/files/McKitterick_Thesis.pdf.

[48] Jae Hun Seol, Insun Jo, Arden L. Moore, Lucas Lindsay, Zachary H. Aitken, Michael T. Pettes, Xuesong Li, Zhen Yao, Rui Huang, David Broido, Natalio Mingo, Rodney S. Ruoff, and Li Shi. Two-Dimensional Phonon Transport in Supported Graphene. *Science*, 328 (5975):213–216, April 2010. ISSN 0036-8075, 1095-9203. doi: 10.1126/science.1184014. URL http://science.sciencemag.org/content/328/5975/213.

[49] S. Yiğen and A. R. Champagne. Wiedemann–Franz Relation and Thermal-Transistor Effect in Suspended Graphene. *Nano Letters*, 14(1):289–293, January 2014. ISSN 1530-6984. doi: 10.1021/nl403967z. URL http://dx.doi.org/10.1021/nl403967z.

[50] L. Wang, I. Meric, P. Y. Huang, Q. Gao, Y. Gao, H. Tran, T. Taniguchi, K. Watanabe, L. M. Campos, D. A. Muller, J. Guo, P. Kim, J. Hone, K. L. Shepard, and C. R. Dean. One-Dimensional Electrical Contact to a Two-Dimensional Material - Supplementary Materials. *Science*, 342(6158):614–617, November 2013. doi: 10.1126/science.1244358.

[51] Kin Chung Fong and K. C. Schwab. Ultrasensitive and Wide-Bandwidth Thermal Measurements of Graphene at Low Temperatures. *Physical Review X*, 2(3):031006, July 2012. doi: 10.1103/PhysRevX.2.031006. URL http://link.aps.org/doi/10.1103/PhysRevX.2.031006.

[52] R. J. Schoelkopf, P. Wahlgren, A. A. Kozhevnikov, P. Delsing, and D. E. Prober. The radio-frequency single-electron transistor (RF-SET): A fast and ultrasensitive electrometer. *Science*, 280(5367):1238–1242, January 1998.

[53] Jiamin Xue, Javier Sanchez-Yamagishi, Danny Bulmash, Philippe Jacquod, Aparna Deshpande, K. Watanabe, T. Taniguchi, Pablo Jarillo-Herrero, and Brian J. LeRoy. Scanning tunnelling microscopy and spectroscopy of ultra-flat graphene on hexagonal boron nitride. *Nature Materials*, 10(4):282–285, April 2011. ISSN 1476-1122. doi: 10.1038/nmat2968. URL http://www.nature.com/nmat/journal/v10/n4/full/nmat2968.html.

[54] Shaffique Adam, Derek Ho, Indra Yudhistira, and Nilotpal Chakraborty. Theoretical study of the criteria and consequences of hydrodynamic electron flow in graphene. In *Bulletin of the American Physical Society*, New Orleans, 2017. American Physical Society. URL http://meetings.aps.org/Meeting/MAR17/Session/X30.8.

[55] Jesse Crossno, Jing K. Shi, Ke Wang, Xiaomeng Liu, Achim Harzheim, Andrew Lucas, Subir Sachdev, Philip Kim, Takashi Taniguchi, Kenji Watanabe, Thomas A. Ohki, and Kin Chung Fong. Observation of the Dirac fluid and the breakdown of the Wiedemann-Franz law in graphene. *Science*, 351(6277):1058–1061, March 2016. ISSN 0036-8075, 1095-9203. doi: 10.1126/science.aad0343. URL http://science.sciencemag.org/content/351/6277/1058.

[56] L. P. Kadanoff and P. C. Martin. Hydrodynamic equations and correlation functions. *Annals of Physics*, 24:419–469, 1963.

[57] M. J. M. De Jong and L. W. Molenkamp. Hydrodynamic electron flow in high-mobility wires. *Physical Review B*, 51(19):13389–13402, 1995.

[58] C. Cao, E. Elliott, J. Joseph, H. Wu, J. Petricka, T. Schäfer, and J. E. Thomas. Universal Quantum Viscosity in a Unitary Fermi Gas. *Science*, 331(6013):58–61, January 2011. ISSN 0036-8075, 1095-9203. doi: 10.1126/science.1195219. URL http://science.sciencemag.org/content/331/6013/58.

[59] E. Shuryak. Why does the quark-gluon plasma at RHIC behave as a nearly ideal fluid? *Progress in Particle and Nuclear Physics*, 53:273–303, 2004.

[60] Markus Müller and Subir Sachdev. Collective cyclotron motion of the relativistic plasma in graphene. *Physical Review B*, 78(11), 2008.

[61] M. Foster and I. Aleiner. Slow imbalance relaxation and thermoelectric transport in graphene. *Physical Review B*, 79(8):085415, 2009.

[62] S. S. Apostolov, A. Levchenko, and A. V. Andreev. Hydrodynamic Coulomb drag of strongly correlated electron liquids. *Physical Review B*, 89(12):121104, 2014.

[63] B. Narozhny, I. Gornyi, M. Titov, M. Schütt, and A. Mirlin. Hydrodynamics in graphene: Linear-response transport. *Physical Review B*, 91:035414, 2015.

[64] K. S. Novoselov, A. K. Geim, S. V. Morozov, D. Jiang, M. I. Katsnelson, I. V. Grigorieva, S. V. Dubonos, and A. A. Firsov. Two-dimensional gas of massless Dirac fermions in graphene. *Nature*, 438(7065):197–200, November 2005. ISSN 0028-0836. doi: 10.1038/nature04233. URL http://www.nature.com/nature/journal/v438/n7065/full/nature04233.html.

[65] Yuanbo Zhang, Yan-Wen Tan, Horst L. Stormer, and Philip Kim. Experimental observation of the quantum Hall effect and Berry's phase in graphene. *Nature*, 438(7065): 201–204, November 2005. ISSN 0028-0836. doi: 10.1038/nature04235. URL http://www.nature.com/nature/journal/v438/n7065/full/nature04235.html.

[66] D. Siegel, W. Regan, A. Fedorov, A. Zettl, and A. Lanzara. Charge-Carrier Screening in Single-Layer Graphene. *Physical Review Letters*, 110(14):146802, 2013.

[67] D. Sheehy and J. Schmalian. Quantum Critical Scaling in Graphene. *Physical Review Letters*, 99(22):226803, 2007.

[68] B. Keimer and S. Sachdev. Quantum Criticality. *Physics Today*, 64:29, 2011.

[69] C. H. Lui, K. F. Mak, J. Shan, and T. F. Heinz. Ultrafast Photoluminescence from Graphene. *Physical Review Letters*, 105(12):127404, 2010.

[70] Markus Breusing, Claus Ropers, and Thomas Elsaesser. Ultrafast Carrier Dynamics in Graphite. *Physical Review Letters*, 102(8):086809, February 2009. doi: 10.1103/PhysRevLett.102.086809. URL https://link.aps.org/doi/10.1103/PhysRevLett.102.086809.

[71] K. J. Tielrooij, J. C. W. Song, S. A. Jensen, A. Centeno, A. Pesquera, A. Zurutuza Elorza, M. Bonn, L. S. Levitov, and F. H. L. Koppens. Photoexcitation cascade and multiple hot-carrier generation in graphene. *Nature Physics*, 9:248, 2013.

[72] Jens Christian Johannsen, Søren Ulstrup, Federico Cilento, Alberto Crepaldi, Michele Zacchigna, Cephise Cacho, I. C. Edmond Turcu, Emma Springate, Felix Fromm, Christian Raidel, Thomas Seyller, Fulvio Parmigiani, Marco Grioni, and Philip Hofmann. Direct View of Hot Carrier Dynamics in Graphene. *Physical Review Letters*, 111(2):027403, July 2013. doi: 10.1103/PhysRevLett.111.027403. URL https://link.aps.org/doi/10.1103/PhysRevLett.111.027403.

[73] M. Müller, J. Schmalian, and L. Fritz. Graphene: A Nearly Perfect Fluid. *Physical Review Letters*, 103(2):025301, July 2009.

[74] Markus Müller, Lars Fritz, and Subir Sachdev. Quantum-critical relativistic magnetotransport in graphene. *Physical Review B*, 78(11):115406, September 2008. doi: 10.1103/PhysRevB.78.115406. URL https://link.aps.org/doi/10.1103/PhysRevB.78.115406.

[75] Nicholas Wakeham, Alimamy F. Bangura, Xiaofeng Xu, Jean-Francois Mercure, Martha Greenblatt, and Nigel E. Hussey. Gross violation of the Wiedemann–Franz law in a quasi-one-dimensional conductor. *Nature Communications*, 2:396, July 2011. ISSN 2041-1723. doi: 10.1038/ncomms1406. URL http://www.nature.com/ncomms/journal/v2/n7/full/ncomms1406.html.

[76] R. P. Smith, M. Sutherland, G. G. Lonzarich, S. S. Saxena, N. Kimura, S. Takashima, M. Nohara, and H. Takagi. Marginal breakdown of the Fermi-liquid state on the border of metallic ferromagnetism. *Nature*, 455(7217):1220–1223, 2008.

[77] H. Pfau and et al. Thermal and electrical transport across a magnetic quantum critical point. *Nature*, 484(7395):493–497, 2012.

[78] R. W. Hill, C. Proust, L. Taillefer, P. Fournier, and R. L. Greene. Breakdown of Fermi-liquid theory in a copper-oxide superconductor. *Nature*, 414(6865):711–715, 2001.

[79] Lars Fritz, Jörg Schmalian, Markus Müller, and Subir Sachdev. Quantum critical transport in clean graphene. *Physical Review B*, 78(8):085416, 2008.

[80] Shaffique Adam, E. H. Hwang, V. M. Galitski, and S. Das Sarma. A self-consistent theory for graphene transport. *Proceedings of the National Academy of Sciences*, 104(47):18392–18397, November 2007. ISSN 0027-8424, 1091-6490. doi: 10.1073/pnas.0704772104. URL http://www.pnas.org/content/104/47/18392.

[81] J. Martin, N. Akerman, G. Ulbricht, T. Lohmann, J. H. Smet, K. von Klitzing, and A. Yacoby. Observation of electron–hole puddles in graphene using a scanning single-electron transistor. *Nature Physics*, 4(2):144–148, February 2008. ISSN 1745-2473. doi: 10.1038/nphys781. URL http://www.nature.com/nphys/journal/v4/n2/abs/nphys781.html.

[82] Yuanbo Zhang, Victor W. Brar, Caglar Girit, Alex Zettl, and Michael F. Crommie. Origin of spatial charge inhomogeneity in graphene. *Nature Physics*, 5(10):722–726, October 2009. ISSN 1745-2473. doi: 10.1038/nphys1365. URL http://www.nature.com/nphys/journal/v5/n10/abs/nphys1365.html.

[83] C. R. Dean and et al. Boron nitride substrates for high-quality graphene electronics. *Nature Nanotechnology*, 5(10):722–726, 2010.

[84] N. J. G. Couto, D. Costanzo, S. Engels, D.-K. Ki, K. Watanabe, T. Taniguchi, C. Stampfer, F. Guinea, and A. F. Morpurgo. Random Strain Fluctuations as Dominant Disorder Source for High-Quality On-Substrate Graphene Devices. *Physical Review X*, 4(4):041019, 2014.

[85] AC Betz, F Vialla, D Brunel, C Voisin, M Picher, A Cavanna, A Madouri, G Fève, J-M Berroir, and B Plaçais. Hot electron cooling by acoustic phonons in graphene. *Physical Review Letters*, 109(5):56805, 2012.

[86] A. Laitinen, M. Oksanen, A. Fay, D. Cox, M. Tomi, P. Virtanen, and P. J. Hakonen. Electron-phonon coupling in suspended graphene: supercollisions by ripples. *Nano Letters*, 14:3009–3013, 2014.

[87] Sean A. Hartnoll, Pavel K. Kovtun, Markus Müller, and Subir Sachdev. Theory of the Nernst effect near quantum phase transitions in condensed matter and in dyonic black holes. *Physical Review B*, 76(14):144502, October 2007. doi: 10.1103/PhysRevB.76.144502. URL https://link.aps.org/doi/10.1103/PhysRevB.76.144502.

[88] Andrew Lucas. Hydrodynamic transport in strongly coupled disordered quantum field theories. *New Journal of Physics*, 17(11):113007, October 2015. ISSN 1367-2630. doi: 10.1088/1367-2630/17/11/113007. URL http://arxiv.org/abs/1506.02662. arXiv: 1506.02662.

[89] Andrew Lucas, Jesse Crossno, Kin Chung Fong, Philip Kim, and Subir Sachdev. Transport in inhomogeneous quantum critical fluids and in the Dirac fluid in graphene. *Physical Review B*, 93(7):075426, February 2016. doi: 10.1103/PhysRevB.93.075426. URL https://link.aps.org/doi/10.1103/PhysRevB.93.075426.

[90] P. K. Kovtun, D. T. Son, and A. O. Starinets. Viscosity in Strongly Interacting Quantum Field Theories from Black Hole Physics. *Physical Review Letters*, 94(11):111601, March 2005. doi: 10.1103/PhysRevLett.94.111601. URL https://link.aps.org/doi/10.1103/PhysRevLett.94.111601.

[91] Alessandro Principi, Giovanni Vignale, Matteo Carrega, and Marco Polini. Bulk and shear viscosities of the 2d electron liquid in a doped graphene sheet. *arXiv.org*, 2015. arXiv: 1506.06030v1.

[92] G. S. Nolas and H. J. Goldsmid. Thermal Conductivity of Semiconductors. In Terry M. Tritt, editor, *Thermal Conductivity*, Physics of Solids and Liquids, pages 105–121. Springer US, 2004. ISBN 978-0-306-48327-1 978-0-387-26017-4. URL http://link.springer.com/chapter/10.1007/0-387-26017-X_4. DOI: 10.1007/0-387-26017-X_4.

[93] H. J. Goldsmid. The Thermal Conductivity of Bismuth Telluride. *Proceedings of the Physical Society. Section B*, 69(2):203, 1956. ISSN 0370-1301. doi: 10.1088/0370-1301/69/2/310. URL http://stacks.iop.org/0370-1301/69/i=2/a=310.

[94] H. Yoshino and K. Murata. Significant enhancement of electronic thermal conductivity of two-dimensional zero-gap systems by bipolar-diffusion effect. *Journal of the Physical Society of Japan*, 84(2):024601, January 2015. ISSN 0031-9015. doi: 10.7566/JPSJ.84.024601. URL http://journals.jps.jp/doi/abs/10.7566/JPSJ.84.024601.

[95] E. H. Hwang and S. Das Sarma. Screening-induced temperature-dependent transport in two-dimensional graphene. *Physical Review B*, 79(16):165404, April 2009. doi: 10.1103/PhysRevB.79.165404. URL https://link.aps.org/doi/10.1103/PhysRevB.79.165404.

[96] D. A. Bandurin, I. Torre, R. Krishna Kumar, M. Ben Shalom, A. Tomadin, A. Principi, G. H. Auton, E. Khestanova, K. S. Novoselov, I. V. Grigorieva, L. A. Ponomarenko, A. K. Geim, and M. Polini. Negative local resistance caused by viscous electron backflow in graphene. *Science*, 351(6277):1055–1058, March 2016. ISSN 0036-8075, 1095-9203. doi: 10.1126/science.aad0201. URL http://science.sciencemag.org/content/351/6277/1055.

[97] Philip J. W. Moll, Pallavi Kushwaha, Nabhanila Nandi, Burkhard Schmidt, and Andrew P. Mackenzie. Evidence for hydrodynamic electron flow in PdCoO2. *Science*, 351(6277):1061–1064, March 2016. ISSN 0036-8075, 1095-9203. doi: 10.1126/science.aac8385. URL http://science.sciencemag.org/content/351/6277/1061.

[98] Jan Zaanen. Electrons go with the flow in exotic material systems. *Science*, 351(6277):1026–1027, March 2016. ISSN 0036-8075, 1095-9203. doi: 10.1126/science.aaf2487. URL http://science.sciencemag.org/content/351/6277/1026.

[99] U. Briskot, M. Schütt, I. V. Gornyi, M. Titov, B. N. Narozhny, and A. D. Mirlin. Collision-dominated nonlinear hydrodynamics in graphene. *Physical Review B*, 92(11):115426, September 2015. doi: 10.1103/PhysRevB.92.115426. URL https://link.aps.org/doi/10.1103/PhysRevB.92.115426.

[100] David Pines. *Theory Of Quantum Liquids: Normal Fermi Liquids*. Westview Press, Reading, Mass, March 1994. ISBN 978-0-201-40774-7.

[101] C. P. Weber, N. Gedik, J. E. Moore, J. Orenstein, J. Stephens, and D. D. Awschalom. Observation of spin Coulomb drag in a two-dimensional electron gas. *Nature*, 437(7063):1330–1333, October 2005. ISSN 0028-0836. doi: 10.1038/nature04206. URL http://www.nature.com/nature/journal/v437/n7063/full/nature04206.html.

[102] Luyi Yang, J. D. Koralek, J. Orenstein, D. R. Tibbetts, J. L. Reno, and M. P. Lilly. Doppler velocimetry of spin propagation in a two-dimensional electron gas. *Nature Physics*, 8(2):153–157, February 2012. ISSN 1745-2473. doi: 10.1038/nphys2157. URL http://www.nature.com/nphys/journal/v8/n2/abs/nphys2157.html.

[103] A. V. Andreev, Steven A. Kivelson, and B. Spivak. Hydrodynamic Description of Transport in Strongly Correlated Electron Systems. *Physical Review Letters*, 106(25):256804, June 2011. doi: 10.1103/PhysRevLett.106.256804. URL https://link.aps.org/doi/10.1103/PhysRevLett.106.256804.

[104] M. Mendoza, H. J. Herrmann, and S. Succi. Preturbulent Regimes in Graphene Flow. *Physical Review Letters*, 106(15):156601, April 2011. doi: 10.1103/PhysRevLett.106.156601. URL https://link.aps.org/doi/10.1103/PhysRevLett.106.156601.

[105] Andrea Tomadin, Giovanni Vignale, and Marco Polini. Corbino Disk Viscometer for 2d Quantum Electron Liquids. *Physical Review Letters*, 113(23):235901, December 2014. doi: 10.1103/PhysRevLett.113.235901. URL https://link.aps.org/doi/10.1103/PhysRevLett.113.235901.

[106] Alessandro Principi and Giovanni Vignale. Violation of the Wiedemann-Franz Law in Hydrodynamic Electron Liquids. *Physical Review Letters*, 115(5):056603, July 2015. doi:

10.1103/PhysRevLett.115.056603. URL https://link.aps.org/doi/10.1103/PhysRevLett.115.056603.

[107] Iacopo Torre, Andrea Tomadin, Andre K. Geim, and Marco Polini. Nonlocal transport and the hydrodynamic shear viscosity in graphene. *Physical Review B*, 92(16):165433, October 2015. doi: 10.1103/PhysRevB.92.165433. URL https://link.aps.org/doi/10.1103/PhysRevB.92.165433.

[108] Leonid Levitov and Gregory Falkovich. Electron viscosity, current vortices and negative nonlocal resistance in graphene. *Nature Physics*, 12(7):672–676, July 2016. ISSN 1745-2473. doi: 10.1038/nphys3667. URL http://www.nature.com/nphys/journal/v12/n7/full/nphys3667.html.

[109] D. van der Marel, H. J. A. Molegraaf, J. Zaanen, Z. Nussinov, F. Carbone, A. Damascelli, H. Eisaki, M. Greven, P. H. Kes, and M. Li. Quantum critical behaviour in a high-Tc superconductor. *Nature*, 425(6955):271–274, September 2003. ISSN 0028-0836. doi: 10.1038/nature01978. URL http://www.nature.com/nature/journal/v425/n6955/full/nature01978.html.

[110] R. A. Cooper, Y. Wang, B. Vignolle, O. J. Lipscombe, S. M. Hayden, Y. Tanabe, T. Adachi, Y. Koike, M. Nohara, H. Takagi, Cyril Proust, and N. E. Hussey. Anomalous Criticality in the Electrical Resistivity of La2–xSrxCuO4. *Science*, 323(5914):603–607, January 2009. ISSN 0036-8075, 1095-9203. doi: 10.1126/science.1165015. URL http://science.sciencemag.org/content/323/5914/603.

[111] Guohong Li, Adina Luican, and Eva Y. Andrei. Scanning Tunneling Spectroscopy of Graphene on Graphite. *Physical Review Letters*, 102(17):176804, April 2009. doi: 10.1103/PhysRevLett.102.176804. URL https://link.aps.org/doi/10.1103/PhysRevLett.102.176804.

[112] Kedar Damle and Subir Sachdev. Nonzero-temperature transport near quantum critical points. *Physical Review B*, 56(14):8714–8733, October 1997. doi: 10.1103/PhysRevB.56.8714. URL https://link.aps.org/doi/10.1103/PhysRevB.56.8714.

[113] Subir Sachdev. *Quantum Phase Transitions*. Cambridge University Press, Cambridge ; New York, 2 edition edition, May 2011. ISBN 978-0-521-51468-2.

[114] Richard A. Davison, Koenraad Schalm, and Jan Zaanen. Holographic duality and the resistivity of strange metals. *Physical Review B*, 89(24):245116, June 2014. doi: 10.1103/PhysRevB.89.245116. URL https://link.aps.org/doi/10.1103/PhysRevB.89.245116.

[115] Mike Blake, David Tong, and David Vegh. Holographic Lattices Give the Graviton an Effective Mass. *Physical Review Letters*, 112(7):071602, February 2014. doi: 10.1103/PhysRevLett.112.071602. URL https://link.aps.org/doi/10.1103/PhysRevLett.112.071602.

[116] Koushik Balasubramanian and Christopher P. Herzog. Losing forward momentum holographically. *Classical and Quantum Gravity*, 31(12):125010, 2014. ISSN 0264-9381. doi: 10.1088/0264-9381/31/12/125010. URL http://stacks.iop.org/0264-9381/31/i=12/a=125010.

[117] Andrew Lucas, Subir Sachdev, and Koenraad Schalm. Scale-invariant hyperscaling-violating holographic theories and the resistivity of strange metals with random-field disorder. *Physical Review D*, 89(6):066018, March 2014. doi: 10.1103/PhysRevD.89.066018. URL https://link.aps.org/doi/10.1103/PhysRevD.89.066018.

[118] Andrew Lucas. Conductivity of a strange metal: from holography to memory functions. *Journal of High Energy Physics*, 2015(3):71, March 2015. ISSN 1029-8479. doi: 10.1007/JHEP03(2015)071. URL https://link.springer.com/article/10.1007/JHEP03(2015)071.

[119] Richard A. Davison and Blaise Goutéraux. Dissecting holographic conductivities. *Journal of High Energy Physics*, 2015(9):90, September 2015. ISSN 1029-8479. doi: 10.1007/JHEP09(2015)090. URL https://link.springer.com/article/10.1007/JHEP09(2015)090.

[120] Mike Blake. Momentum relaxation from the fluid/gravity correspondence. *Journal of High Energy Physics*, 2015(9):10, September 2015. ISSN 1029-8479. doi: 10.1007/JHEP09(2015)010. URL https://link.springer.com/article/10.1007/JHEP09(2015)010.

[121] Aristomenis Donos and Jerome P. Gauntlett. Navier-Stokes equations on black hole horizons and DC thermoelectric conductivity. *Physical Review D*, 92(12):121901, December 2015. doi: 10.1103/PhysRevD.92.121901. URL https://link.aps.org/doi/10.1103/PhysRevD.92.121901.

[122] Sašo Grozdanov, Andrew Lucas, Subir Sachdev, and Koenraad Schalm. Absence of Disorder-Driven Metal-Insulator Transitions in Simple Holographic Models. *Physical Review Letters*, 115(22):221601, November 2015. doi: 10.1103/PhysRevLett.115.221601. URL https://link.aps.org/doi/10.1103/PhysRevLett.115.221601.

[123] Enrico Rossi and S. Das Sarma. Ground State of Graphene in the Presence of Random Charged Impurities. *Physical Review Letters*, 101(16):166803, October 2008. doi: 10.1103/PhysRevLett.101.166803. URL https://link.aps.org/doi/10.1103/PhysRevLett.101.166803.

[124] Enrico Rossi, S. Adam, and S. Das Sarma. Effective medium theory for disordered two-dimensional graphene. *Physical Review B*, 79(24):245423, June 2009. doi: 10.1103/PhysRevB.79.245423. URL https://link.aps.org/doi/10.1103/PhysRevB.79.245423.

[125] Dmitry K. Efimkin and Victor Galitski. Strongly interacting Dirac liquid on the surface of a topological Kondo insulator. *Physical Review B*, 90(8):081113, August 2014. doi: 10.1103/PhysRevB.90.081113. URL https://link.aps.org/doi/10.1103/PhysRevB.90.081113.

[126] Ling Lu, Zhiyu Wang, Dexin Ye, Lixin Ran, Liang Fu, John D. Joannopoulos, and Marin Soljačić. Experimental observation of Weyl points. *Science*, 349(6248):622–624, August 2015. ISSN 0036-8075, 1095-9203. doi: 10.1126/science.aaa9273. URL http://science.sciencemag.org/content/349/6248/622.

[127] Su-Yang Xu, Ilya Belopolski, Nasser Alidoust, Madhab Neupane, Guang Bian, Chenglong Zhang, Raman Sankar, Guoqing Chang, Zhujun Yuan, Chi-Cheng Lee, Shin-Ming Huang, Hao Zheng, Jie Ma, Daniel S. Sanchez, BaoKai Wang, Arun Bansil, Fangcheng Chou, Pavel P. Shibayev, Hsin Lin, Shuang Jia, and M. Zahid Hasan. Discovery of a Weyl fermion semimetal and topological Fermi arcs. *Science*, 349(6248):613–617, August 2015. ISSN 0036-8075, 1095-9203. doi: 10.1126/science.aaa9297. URL http://science.sciencemag.org/content/349/6248/613.

[128] B. Q. Lv, H. M. Weng, B. B. Fu, X. P. Wang, H. Miao, J. Ma, P. Richard, X. C. Huang, L. X. Zhao, G. F. Chen, Z. Fang, X. Dai, T. Qian, and H. Ding. Experimental Discovery of Weyl Semimetal TaAs. *Physical Review X*, 5(3):031013, July 2015. doi: 10.1103/PhysRevX.5.031013. URL https://link.aps.org/doi/10.1103/PhysRevX.5.031013.

[129] H. B. Nielsen and Masao Ninomiya. The Adler-Bell-Jackiw anomaly and Weyl fermions in a crystal. *Physics Letters B*, 130(6):389–396, November 1983. ISSN 0370-2693. doi: 10.1016/0370-2693(83)91529-0. URL http://www.sciencedirect.com/science/article/pii/0370269383915290.

[130] D. T. Son and B. Z. Spivak. Chiral anomaly and classical negative magnetoresistance of Weyl metals. *Physical Review B*, 88(10):104412, September 2013. doi: 10.1103/PhysRevB.88.104412. URL https://link.aps.org/doi/10.1103/PhysRevB.88.104412.

[131] Sean A. Hartnoll. Lectures on holographic methods for condensed matter physics. *Classical and Quantum Gravity*, 26(22):224002, 2009. ISSN 0264-9381. doi: 10.1088/0264-9381/26/22/224002. URL http://stacks.iop.org/0264-9381/26/i=22/a=224002.

[132] Oskar Vafek. Anomalous Thermodynamics of Coulomb-Interacting Massless Dirac Fermions in Two Spatial Dimensions. *Physical Review Letters*, 98(21):216401, May 2007. doi: 10.1103/PhysRevLett.98.216401. URL https://link.aps.org/doi/10.1103/PhysRevLett.98.216401.

[133] Andrew Lucas and Subir Sachdev. Memory matrix theory of magnetotransport in strange metals. *Physical Review B*, 91(19):195122, May 2015. doi: 10.1103/PhysRevB.91.195122. URL https://link.aps.org/doi/10.1103/PhysRevB.91.195122.

[134] Matthew Luzum and Paul Romatschke. Conformal relativistic viscous hydrodynamics: Applications to RHIC results at $\sqrt{{s}_{\mathit{nn}}}=200$ GeV. *Physical Review C*, 78(3):034915, September 2008. doi: 10.1103/PhysRevC.78.034915. URL https://link.aps.org/doi/10.1103/PhysRevC.78.034915.

[135] B. Huard, N. Stander, J. A. Sulpizio, and D. Goldhaber-Gordon. Evidence of the role of contacts on the observed electron-hole asymmetry in graphene. *Physical Review B*, 78(12):121402, September 2008. doi: 10.1103/PhysRevB.78.121402. URL https://link.aps.org/doi/10.1103/PhysRevB.78.121402.

[136] Scott Kirkpatrick. Classical Transport in Disordered Media: Scaling and Effective-Medium Theories. *Physical Review Letters*, 27(25):1722–1725, December 1971. doi: 10.1103/PhysRevLett.27.1722. URL https://link.aps.org/doi/10.1103/PhysRevLett.27.1722.

[137] B. Derrida and J. Vannimenus. A transfer-matrix approach to random resistor networks. *Journal of Physics A: Mathematical and General*, 15(10):L557, 1982. ISSN 0305-4470. doi: 10.1088/0305-4470/15/10/007. URL http://stacks.iop.org/0305-4470/15/i=10/a=007.

[138] E. H. Hwang and S. Das Sarma. Acoustic phonon scattering limited carrier mobility in two-dimensional extrinsic graphene. *Physical Review B*, 77(11):115449, March 2008. doi: 10.1103/PhysRevB.77.115449. URL https://link.aps.org/doi/10.1103/PhysRevB.77.115449.

[139] K. I. Bolotin, K. J. Sikes, Z. Jiang, M. Klima, G. Fudenberg, J. Hone, P. Kim, and H. L. Stormer. Ultrahigh electron mobility in suspended graphene. *Solid State Communications*, 146(9–10):351–355, June 2008. ISSN 0038-1098. doi: 10.1016/j.ssc.2008.02.024. URL http://www.sciencedirect.com/science/article/pii/S0038109808001178.

[140] Alexander S. Mayorov, Daniel C. Elias, Ivan S. Mukhin, Sergey V. Morozov, Leonid A. Ponomarenko, Kostya S. Novoselov, A. K. Geim, and Roman V. Gorbachev. How Close Can One Approach the Dirac Point in Graphene Experimentally? *Nano Letters*, 12(9):4629–4634, September 2012. ISSN 1530-6984. doi: 10.1021/nl301922d. URL http://dx.doi.org/10.1021/nl301922d.

[141] Jason Horng, Chi-Fan Chen, Baisong Geng, Caglar Girit, Yuanbo Zhang, Zhao Hao, Hans A. Bechtel, Michael Martin, Alex Zettl, Michael F. Crommie, Y. Ron Shen, and Feng Wang. Drude conductivity of Dirac fermions in graphene. *Physical Review B*, 83(16):165113, April 2011. doi: 10.1103/PhysRevB.83.165113. URL https://link.aps.org/doi/10.1103/PhysRevB.83.165113.

[142] Fereshte Ghahari, Hong-Yi Xie, Takashi Taniguchi, Kenji Watanabe, Matthew S. Foster, and Philip Kim. Enhanced Thermoelectric Power in Graphene: Violation of the Mott Relation by Inelastic Scattering. *Physical Review Letters*, 116(13):136802, March 2016. doi: 10.1103/PhysRevLett.116.136802. URL https://link.aps.org/doi/10.1103/PhysRevLett.116.136802.

[143] C. L. Kane and Matthew P. A. Fisher. Thermal Transport in a Luttinger Liquid. *Physical Review Letters*, 76(17):3192–3195, April 1996. doi: 10.1103/PhysRevLett.76.3192. URL https://link.aps.org/doi/10.1103/PhysRevLett.76.3192.

[144] S. Y. Li, Louis Taillefer, C. H. Wang, and X. H. Chen. Ballistic Magnon Transport and Phonon Scattering in the Antiferromagnet ${\mathrm{Nd}}_{2}{\mathrm{CuO}}_{4}$. *Physical Review Letters*, 95(15):156603, October 2005. doi: 10.1103/PhysRevLett.95.156603. URL https://link.aps.org/doi/10.1103/PhysRevLett.95.156603.

[145] D. C. McCollum, R. L. Wild, and J. Callaway. Spin-Wave Thermal Conductivity of Ferromagnetic EuS. *Physical Review*, 136(2A):A426–A428, October 1964. doi: 10.1103/PhysRev.136.A426. URL https://link.aps.org/doi/10.1103/PhysRev.136.A426.

[146] Aveek Bid, N. Ofek, H. Inoue, M. Heiblum, C. L. Kane, V. Umansky, and D. Mahalu. Observation of neutral modes in the fractional quantum Hall regime. *Nature*, 466 (7306):585–590, July 2010. ISSN 0028-0836. doi: 10.1038/nature09277. URL http://www.nature.com/nature/journal/v466/n7306/full/nature09277.html.

[147] Hiroyuki Inoue, Anna Grivnin, Yuval Ronen, Moty Heiblum, Vladimir Umansky, and Diana Mahalu. Proliferation of neutral modes in fractional quantum Hall states. *Nature Communications*, 5:4067, June 2014. ISSN 2041-1723. doi: 10.1038/ncomms5067. URL http://www.nature.com/ncomms/2014/140606/ncomms5067/full/ncomms5067.html.

[148] Vivek Venkatachalam, Sean Hart, Loren Pfeiffer, Ken West, and Amir Yacoby. Local thermometry of neutral modes on the quantum Hall edge. *Nature Physics*, 8(9):676–681, September 2012. ISSN 1745-2473. doi: 10.1038/nphys2384. URL http://www.nature.com/nphys/journal/v8/n9/full/nphys2384.html.

[149] A. Y. Kuntsevich, Y. V. Tupikov, V. M. Pudalov, and I. S. Burmistrov. Strongly correlated two-dimensional plasma explored from entropy measurements. *Nature Communications*, 6: 7298, June 2015. ISSN 2041-1723. doi: 10.1038/ncomms8298. URL http://www.nature.com/ncomms/2015/150623/ncomms8298/full/ncomms8298.html.

[150] P. Mazur and S. R. de Groot. On onsager's relations in a magnetic field. *Physica*, 19(1):961–970, January 1953. ISSN 0031-8914. doi: 10.1016/S0031-8914(53)80108-4. URL http://www.sciencedirect.com/science/article/pii/S0031891453801084.

[151] L. Smrcka and P. Streda. Transport coefficients in strong magnetic fields. *Journal of Physics C: Solid State Physics*, 10(12):2153, 1977. ISSN 0022-3719. doi: 10.1088/0022-3719/10/12/021. URL http://stacks.iop.org/0022-3719/10/i=12/a=021.

[152] Yuri M. Zuev, Willy Chang, and Philip Kim. Thermoelectric and Magnetothermoelectric Transport Measurements of Graphene. *Physical Review Letters*, 102(9):096807, March 2009. doi: 10.1103/PhysRevLett.102.096807. URL https://link.aps.org/doi/10.1103/PhysRevLett.102.096807.

[153] Balázs Dóra and Peter Thalmeier. Magnetotransport and thermoelectricity in Landau-quantized disordered graphene. *Physical Review B*, 76(3):035402, July 2007. doi: 10.1103/PhysRevB.76.035402. URL https://link.aps.org/doi/10.1103/PhysRevB.76.035402.

[154] Wen Long, Hui Zhang, and Qing-feng Sun. Quantum thermal Hall effect in graphene. *Physical Review B*, 84(7):075416, August 2011. doi: 10.1103/PhysRevB.84.075416. URL https://link.aps.org/doi/10.1103/PhysRevB.84.075416.

[155] V. P. Gusynin and S. G. Sharapov. Magnetic oscillations in planar systems with the Dirac-like spectrum of quasiparticle excitations. II. Transport properties. *Physical Review B*, 71(12):125124, March 2005. doi: 10.1103/PhysRevB.71.125124. URL https://link.aps.org/doi/10.1103/PhysRevB.71.125124.

[156] COMSOL Multiphysics®, 2017. URL www.comsol.com.

[157] Lloyd N. Trefethen. *Spectral Methods in MATLAB*. SIAM: Society for Industrial and Applied Mathematics, Philadelphia, PA, 62026th edition edition, February 2001. ISBN 978-0-89871-465-4.

[158] Barry Smith, Petter Bjorstad, and William Gropp. *Domain Decomposition: Parallel Multilevel Methods for Elliptic Partial Differential Equations*. Cambridge University Press, Cambridge, March 2004. ISBN 978-0-521-60286-0.

Kim group photo taken while hiking in the White Mountains (2015).